A High-Throughput Analytic Strategy for Discovery of Molecular Targeting Ligands for Pancreatic Diseases

---

A

Dissertation

Presented to

the faculty of the School of Engineering and Applied Science

University of Virginia

---

in partial fulfillment

of the requirements for the degree

Doctor of Philosophy

by

Jessica Hung

August 2021

APPROVAL SHEET

This

Dissertation

is submitted in partial fulfillment of the requirements
for the degree of

Doctor of Philosophy

Author: Jessica Hung

This Dissertation has been read and approved by the examing committee:

Advisor: Kimberly A. Kelly, PhD

Advisor:

Committee Member: Thomas H. Barker, PhD

Committee Member: Alexander L. Klibanov, PhD

Committee Member: Todd W. Bauer, MD

Committee Member: Andrew C. Dudley, PhD

Committee Member:

Committee Member:

Accepted for the School of Engineering and Applied Science:

Craig H. Benson, School of Engineering and Applied Science

August 2021

Abstract

Pancreatic diseases are worldwide public health issues and account for substantial health care utilization and spending. Thus far, effective therapeutic options remain limited. The emergence of proteomic technologies has improved our understanding of differential protein expression in chronic pancreatitis (CP) and pancreatic cancer. Yet, developing target-specific interventions based on proteomic profiles will require significant improvement in the methodologies to generating targeting moieties. In this dissertation, we explore phage display as a method for selecting molecular ligands in pancreatic diseases. Phage display is a versatile screening technique that has been used in drug discovery, epitope mapping, and ligand identification. Next-generation sequencing has dramatically increased the throughput of phage display, and a large database of potential moieties can be easily generated. However, methods to guide ligand selection has yet to be matured, especially for in vivo phage display because there are more diverse targets present in the system. Thus, the overarching goal of this dissertation is to establish an in vivo phage display-based pipeline and utilize quantitative methods to advance the identification of targeting moieties and their molecular targets for pancreatic diseases.

The first aim of this dissertation is to evaluate four analytical methods in selecting high specific targeting ligands for deep-sequenced in vivo phage display. Using the mouse model of CP as a disease model, we identify seven 7-mer peptides that demonstrate preferential binding to the CP over the healthy pancreas. In the second aim of this dissertation, we further evaluate the cellular selectivity of CP-targeted peptides and utilize these findings to design a targeted liposomal formulation to deliver a small molecular drug, apigenin, to achieve targeted antifibrotic therapy for CP. Finally, we leverage phage display beyond ligand identification by using functional proteomics to identify the binding partner of a peptide specific to pancreatic cancer-associated fibroblasts. The finding of a novel molecular target motivates the development of a stromal targeted drug delivery platform to reprogram the crosstalk between cancer cells and cancer-associated fibroblasts in pancreatic cancer. Collectively, these aims establish a streamline from ligand identification to the development of target-specific nanomedicine for pancreatic diseases.

Acknowledgements

First and foremost, I would like to express my deepest gratitude to my advisor, Dr. Kimberly Kelly, without whom the work of this dissertation would not have been possible. Thank you for your mentorship, guidance, and support throughout my professional development. You are an extraordinary role model that I look upon in so many aspects. Thank you for challenging me to look at the bigger picture and to become a better writer in science. Thank you for letting me grow at a comfortable pace and offering sound advice when most needed. Thank you for helping me fortify my skills in scientific communication. The last six years of working with you have shaped me into an independent researcher and a better scientist. Thank you for all that you have done for me.

A sincere appreciation to my committee members, Dr. Thomas Barker, Dr. Sasha Klibanov, Dr. Todd Bauer, and Dr. Andrew Dudley, for their invaluable scientific perspective and support throughout graduate school. Tom, thank you for being my chair and for sharing your trick to "hunt down" PIs using the cat metaphor. Todd, thank you for providing clinical perspective and challenging me to think about the greater impact of the project. Drew, thank you for providing valuable insight into endothelial cells and sharing the cell lines with us. Sasha, thank you for the time you dedicated to meeting with me, in-person or on zoom, and sharing everything you know about liposomes. Your willingness and patience in answering all my questions made our every meeting a valuable lesson to me.

Thank you to my incredible labmates, who are the major contributors to make the lab a joyful working space and whom I have learned so much from and grown alongside – Siva Sai Krishna Dasa, Julien Dimastromatteo, Michael Gutknecht, Lindsey Brinton, Dustin Baucknight, Samantha Perez, and Roxanne Ruiz. I cannot decide which one is better, doing science or building a gingerbread house with you all! To Siva, Julien, and Michael, thank you for being the most reliable resource when I ran into questions – no matter big or small – since day one I joined the lab. To Lindsey and Dustin, thank you for guiding me into the world of phage and sharing all the need-to-knows about graduate schools. To Samantha, thank you for being my coffee buddy, early morning/late night carpool partner, and co-guardian of the lab's tidiness. I am glad to have

overlapped with you for most of my time here at UVA, and my appreciation to you is totally reflected in the insanely high numbers of matching outfits we happen to own. A special thanks to Venessa Trevino-Stevens, our lab would not operate as smoothly without you.

Next, I wish to express my thanks to the undergraduate students whom I had the privilege of mentoring over the years – Rohni Awasthi, Zainab Aziz, Aishu Hombal, Saquib Rizvi, and Bess Woods. Thank you for sharing your time, passion, creativity, and talent with me. Working with you has been a pleasant experience, and you have taught me how to communicate better in science and become a better mentor.

To all my friends in the department, BIMS, TGSA, and UVA community, you have made Charlottesville a home to me. I am grateful for meeting each and every one of you. I enjoy every science conversation on the hallway, jokes over cookie hours, attending athletic events together, fun gatherings on holidays, and warm messages and encouragements that we exchanged all the time.

Finally, this journey would not have even begun without the support of my family. Dad and mom, thank you for inspiring me into the field of science and engineering, for encouraging and supporting a 17-years-old's decision to pursue a bachelor's and doctorate overseas, and for continuously asking for my graduation timeline since year 3 (which did help…a little bit!). To my siblings, thank you for being the best sister and brother I could ever ask for – life would have missed so much fun without you. To my sister, I feel blessed to have spent the last five years with you together in Charlottesville. Your humor and company are always there to walk me through all the good and bad times. To my grandparents, although you never understand what I am working on and why *biology*, *medicine*, and *engineering* make a single phrase, your 100% love and confidence in me are what carried me through this journey. I will always and forever miss you.

Table of Contents

List of Figures

Chapter 1. Background and Significance

Portions of the text from this chapter have been published here:

Hung J, Reynolds F, Kelly KA (2021). "Phage Display for Imaging Agent Development" of *Molecular Imaging: Principles and Practice, 2nd Edition*. PMPH-USA, 2021. (*In press)*

1.1 Introduction

Since the announcement of the Precision Medicine Initiative in 2015 [1], emerging experimental and computational technologies have been developed to advance personalized interventions. The goal of precision medicine is to reveal the mechanistic profile of disease on a patient-to-patient basis and utilize the gathered information, such as genetic profile, proteomics, metabolomics, and environmental factors, to direct a specific intervention that matches an individual's needs. The patient-oriented strategy aims to improve treatment and diagnostic specificity using the right combinations at the optimized dosage. This, in particular, benefits chronic diseases where complex and dynamic molecular events occur in response to genetic and environmental stimuli at various levels throughout disease progression. For example, cancers undergo genetic and epigenetic alterations that lead to differential responses to the same treatment and potential development of drug resistance; the etiology of chronic inflammatory diseases remains enigmatic as integrated pathophysiological factors in genome [2], exposome [3], microbiome [4], and immunome [5] could contribute to the dysregulation of inflammatory pathways. The emergence of omics technologies has improved our understanding of genetic mutations and differential protein expressions. However, the clinical translatability of these findings remains disappointed. Novel approaches that reveal underlying mechanisms and/or allow differentiation of disease from the healthy condition are needed to improve clinical outcomes. Indeed, molecular ligands specific to patient subsets or disease stages hold significant promise to close this gap by serving as a tool to stratify target populations, reveal druggable targets, and functionalize nanoparticles to deliver therapeutics to the target cells. Through ligand-mediated interventions, precision medicine can be used to tailor treatments for complex diseases.

In this chapter, we discuss ligand-mediated therapies, outline the challenges in the existing omics technologies pertaining to ligand identification, provide literature reviews on phage display and their applications in selecting high-affinity ligands, and introduce a new approach that utilizes computational guidance to enhance ligand selection from experimental data collected using phage display. Finally, we summarize targeting ligands and molecular targets

that have been identified for pancreatic diseases and their potential in developing targeted therapies.

1.2 Ligand-mediated therapeutic strategies

Ligand-mediated targeting of therapeutics has been widely explored in various disease treatments to selectively improve drug delivery to the target cells and minimize off-target effects. By taking advantage of molecularly targeted ligands that bind specifically to receptors or antigens, which are either uniquely expressed or overexpressed on the diseased cells compared to the normal tissues, small molecular drugs or drug carriers can be engineered to facilitate targeting and allow administration of higher dose while maintaining acceptable safety at non-diseased sites. In addition to therapeutic benefits, targeting ligands can be radionuclide-labeled to generate a companion theranostic agent to first detect abnormal cells expressing the corresponding receptors and then achieve therapeutic actions through drug activity. The incorporation of targeting ligands can be tailored for individual needs, overcome biological barriers that limit drug delivery, and potentially improve the potency of therapies (Figure 1.1).

Several targeting moieties, including antibodies, peptides, proteins, and small molecules, have been explored for targeted therapy [6, 7]. Antibody-based ligands, either monoclonal antibody or antibody fragments (e.g., Fab, scFv, and minibody), are the most commonly used high-affinity ligands because of their favorable pharmacokinetics (long circulation half-life) and the broad diversity of antigens that they target. However, antibodies are expensive to produce and difficult to synthesize on a large scale. Antibodies also face concerns for stability, short shelf-life, and immunogenicity [6]. Non-antibody ligands, especially peptides, are typically non-immunogenic, can adopt conformations that compliment extended surfaces, and combine high affinity and selectivity with a greater tolerance for modification.

Ligands conjugated to nanoparticles have been used in facilitating target-specific treatments in preclinical and clinical studies. Lipid-based nanoparticles, in particular, have been approved and shown clinical efficacy in delivering small molecular drugs in cancer therapies [8–10]. Liposomes are the most commonly used form with the capacity to encapsulate hydrophilic, hydrophobic, and lipophilic drugs. Moreover, liposomes have high versatility that their particle

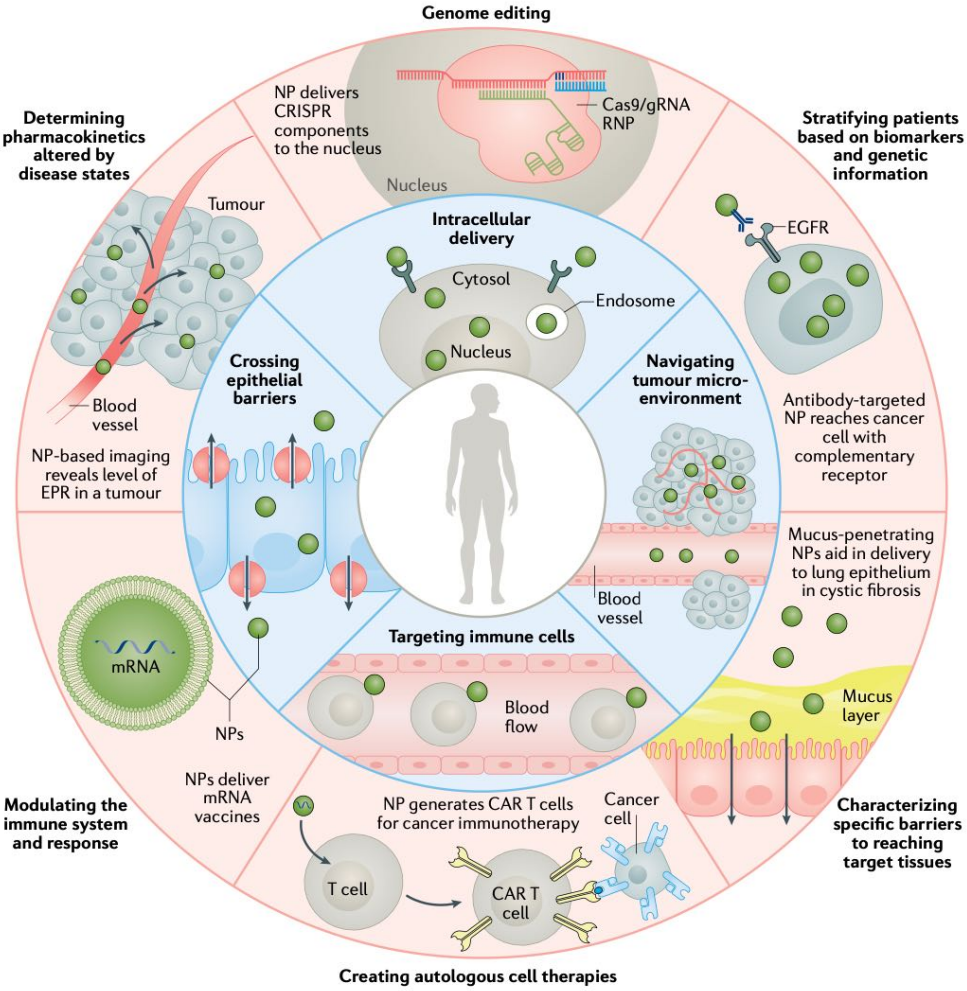

Figure 1.1. Biological barriers to precision medicine applications. Overview highlighting some of the biological barriers that nanoparticles (NPs) can overcome (inner ring) and precision medicine applications that may benefit from NPs (outer ring). As explored in this Review, intelligent NP designs that improve delivery have the potential to enhance the performance of precision medicines and, thus, accelerate their clinical translation. CAR, chimeric antigen receptor; EGFR, epidermal growth factor receptor; EPR, enhanced permeation and retention; gRNA, guide RNA; RNP, ribonucleoprotein.

Reprinted from [7], "Engineering precision nanoparticles for drug delivery", Mitchell, M.J., Billingsley, M.M., Haley, R.M. *et al. Nat Rev Drug Discov* **20,** 101–124 (2021). https://doi.org/10.1038/s41573-020-0090-8*, with permission from Wolters Kluwer.*

size, surface charge, lipid composition, drug payloads, and ligand modifications can be engineered to meet the need for a wide variety of systems [7]. For instance, the size of the nanoparticles affects the clearance rate that particles with diameters less than 10 nm undergo rapid clearance by kidneys; particles greater than 200 nm will activate the complement system and accumulate in the liver or spleen [11]. Surface coating with polyethylene glycol (PEG) can prevent liposome opsonization and extend blood circulation half-life by ten times compared to the non-stealth formulations [12]. Liposomes functionalized with targeting ligands have been shown to promote tumor accumulation, reduce toxicity, and improve antitumoral effects in breast [13], ovarian [14], prostate [15], lung [16], and colorectal cancer [17]. Incorporation of targeting ligands leverages nanoparticles from passive delivery to selectively bind to targets of interest and demonstrate an effective platform for targeted therapy.

1.3 Current challenges in ligand identification

Traditional ligand identification methods usually start with a known target, and then the antibody or peptide ligands will be designed to meet the predicted structure of the target. This process requires years of iterations and validation to mature high-affinity ligands. The emerging development in next-generation sequencing has dramatically increased the throughput and allowed rapid generation of genome database in a wide variety of systems. However, there are only few relevant targets identified with the sequencing of the human genome. This is because proteins, as the main functional molecules, usually undergo posttranslational modifications, such as alternative splicing, methylation, glycosylation, acetylation, and ubiquitination. These events, however, are not captured by comparative gene expression analysis and, thus, diminish the clinical relevance of making predictions on functional interactions purely based on genetic compositions. Additionally, comparative gene expression analysis is an indirect method to identify targeting ligands as only the identity of the target is revealed. Similar to the traditional method, ligands will need to be identified or engineered for each target.

Proteomic approaches have been widely used in facilitating our understanding of the molecular responses to perturbations within cells and tissues. It also provides a direct mapping of proteomic profile to disease status. However, effective ligand selection methods have yet to

be perfected to meet the clinical need for developing targeting moieties that discriminate between healthy and diseased cells. One of the challenges in using the proteomic approach for ligand identification is the systematic bias induced during sample preparations. Mass spectrometry (MS)-based proteomics is the most commonly used platform to profile proteomes and study protein-protein interactions. In order to prepare protein samples from cells or tissues for liquid chromatography-tandem MS (LC-MS/MS) analysis, proteins are denatured, digested (e.g., disulfide bond reduction and cysteine alkylation), then proceed through gel- or centrifuge-based precipitation [18]. These methods induce different biases in sample preparation. For example, the in-solution digestion method could result in a 27-40% loss of peptide and protein throughout the process; methionine oxidation and deamidation of asparagine and glutamine are often found using the in-gel digestion method [19]. The sample preparation procedure also introduces biases as the molecular weight distribution favors larger peptides and proteins and those with higher solubility at pH values of the digestion buffers [19]. In addition, biospecimen acquisition procedures and intraoperative ischemia could induce loss of phosphorylation status and affect biomarker readouts of P13K/mTOR signaling in breast cancer [20]. Workflows that better preserve proteins' native structures during screening can minimize systematic bias and decrease the selection of false-positive biomarkers.

Next, the lack of comparative analysis to allow multi-database cross-referencing limits the application of proteomics in identifying tissue-selective markers [6, 11]. Targeting ligands with high tissue selectivity can significantly reduce off-target effects in vivo [23]. Proteomic labeling techniques in MS-based approaches, such as enzyme biotinylation [15–19] and biorthogonal amino acids labeling [20–27], offer a way to pre-label specific cell types in a multicellular organism prior to proteomic analysis. These methods, however, are limited by low labeling selectivity and efficiency that they fail to provide a systematic evaluation on tissue-wide proteomes purely based on wet-lab methodologies [37]. Moreover, crude comparison of omics data from independent assays poses challenges in data harmonization and increases the difficulty of interpretation [38]. For these reasons, it is crucial to develop in silico approach that allows cross-database comparison based on quantitative algorithms. In this way, current findings of cell-centered proteomics can be leveraged to form a tissue-wide protein database and provide a

more comprehensive evaluation that allows selection of candidate ligands matching the design criteria of targeted drug delivery platforms for the system of interest.

In sum, promising trends toward more rigorous data collection, less biased sample handling, easier database integration, and development of in silico comparative algorithms will continue to drive the realization of precision diagnostics and treatments.

1.4 Phage display: a versatile ligand screening technique and beyond

1.4.1 Phage display in ligand identification

Phage display is a versatile screening technique that has so far been published in over 9000 publications in PubMed since first described by George Smith in 1985 [39]. In addition to its major impact on immunology [40], cell biology [41], drug discovery [42], and pharmacology [43], phage display also contributes to the selection of antibodies specific to known antigens [44], epitope mapping [45], and discovery of disease-specific peptides [37–40]. Phage display employs a population of bacteriophage genetically modified to display a library on various phage coat proteins. These libraries, made of either peptide [39], cDNA [50], or antibody and its fragments [42–44], possess molecular diversities as high as 10^{10} clones and can perform a rapid screening on biomolecules, cells, tissues, or in vivo. During biopanning, targets are maintained in their natural conformations to allow phage binding, followed by washing and amplification of phage that bound to the targets (Figure 1.2). This “direct” approach minimizes bias induced from sample preparation as seen in MS-based approaches, which in return increases clinical relevance of the selected ligands.

Another exciting feature of phage display is that no prior knowledge of the target is needed when designing the screening. This advantage is exemplified in ligand identification via in vivo screening in diseases whose molecular mechanism remains enigmatic and yield disease or organ-specific phage clones [54]. The process begins with intravenous administration of phage display libraries in the desired animal models or patient settings, followed by target organ extraction and bound phage isolation (Figure 1.2). Compared to in vitro or in situ screening, in vivo phage display exposes naive libraries to heterogenous repertoires while being subject to the body's clearance system; thus, preselecting homing probes that are less likely to be removed by

the reticuloendothelial system. This technique has been used to develop a number of targeting ligands for atherosclerosis [55], inflamed cardiomyocyte [48], and endothelial bed in both mice and humans [45, 47]. Likewise, in vivo screening for tumor vascular targets have also produced peptides specific for tumor-associated endothelial cells [57]. In addition to vascular targets, researchers have extended the technology to include in vivo screening for tumor epithelial cells and have found specific peptides for cancers such as prostate [49, 50], oral [60], and neuroblastoma [61]. Ligands homing to ischemic tissues and plaques have also been identified in stroke [62] and Alzheimer's [63] models, demonstrating the potential of developing targeted therapy and imaging agents for neurological disorders.

1.4.2 Pitfalls of conventional phage display

Just like all the other proteomic technologies, phage display also induces biases that could skew screening readouts. Conventionally, the enriched pools are titered, colonies picked, amplified, and DNA sequenced to produce homogenous, characterized individual phage samples that are ready for analysis. This procedure is considered labor-intensive and low throughput, required multiple rounds of biopanning and appropriate inclusion of positive and negative controls are required to obtain phage clones with high binding affinity. Since only 10-100 out of millions of presented clones were usually sequenced, the plaque picking approach suffers from sampling effects, and the readouts fail to cover most of the library complexity. In addition, each screen is an independent process that direct comparison is impossible between screens performed on different targets or using different libraries. In fact, lacking a robust and quantitative algorithm to guide lead compound selection significantly increases false-positive rates and prolongs the validation procedures [64]. Recent developments in next-generation sequencing (NGS) have opened a new avenue in providing a high-throughput approach that increases genome sequencing capacity to cover 75-8500 base pairs at low cost [65]. Pipelines that adopt NGS platforms into phage display workflow can address pitfalls of conventional phage display and provide a more robust process for ligand selection.

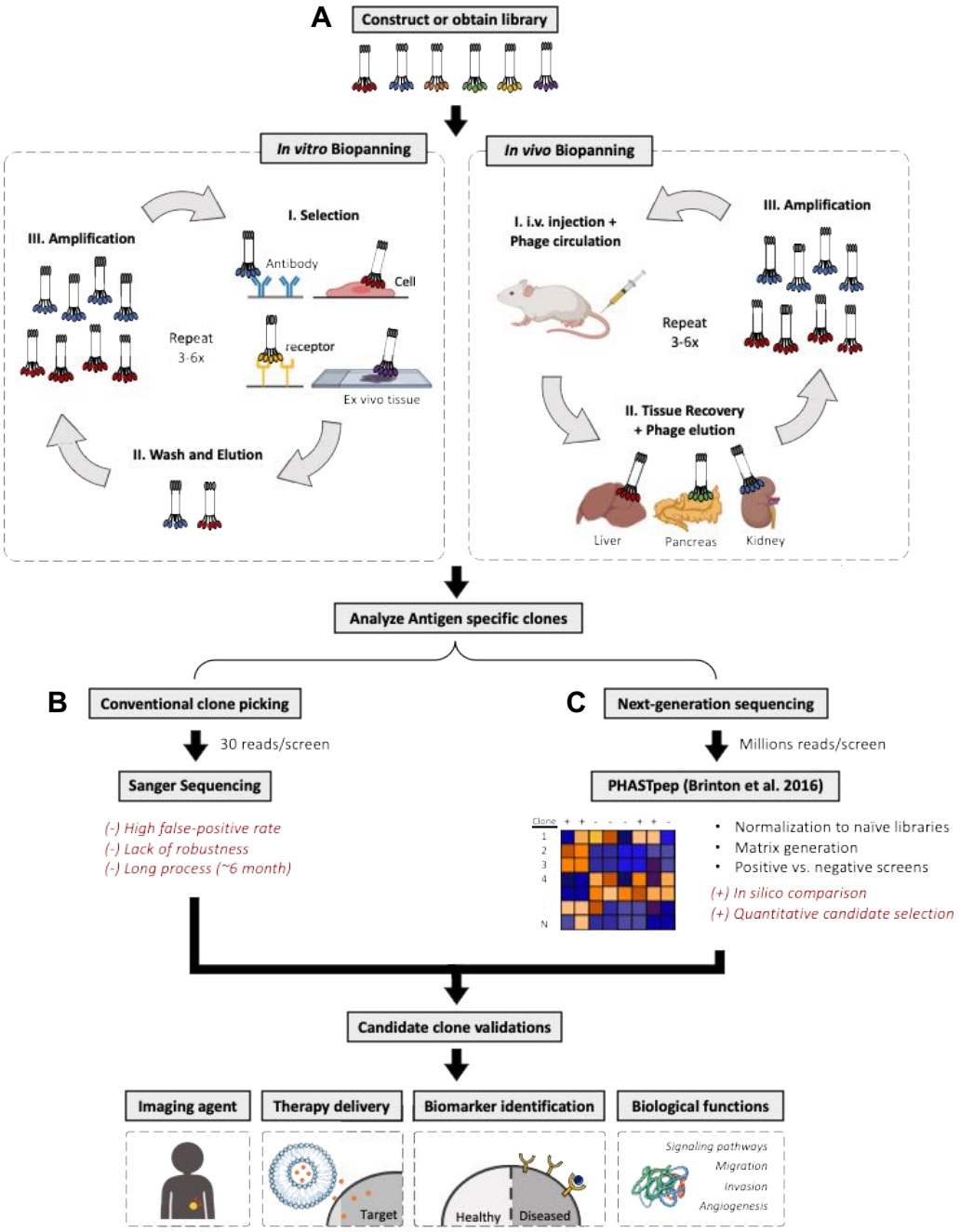

Figure 1.2. Schematics of phage display process. (A) Phage libraries were applied to in vitro targets, including protein, cells, tissues, or live animals for tissue-specific clone in the biopanning process. (B) The conventional clone picking approach manually isolates a limited amount of phage clones for Sanger sequencing, which usually results in a high false-positive rate and long experimental duration. (C) QSAT deep sequences all phage clones present in the final round of biopanning and utilizes PHASTpep to guide ligand section. The identified and validated ligands can be applied to develop for targeting modality in diagnosis and therapy or reveal disease-specific biomarkers and their functional roles.

1.4.3 Computational-guided ligand selection from NGS-phage display

Taking advantage of the Illumina MiSeq platform, which generates approximately 25 million of 150-basepair reads per run and supports sample multiplexing [66], high-throughput deep sequencing can be performed to effectively determine the sequences of various types of phage libraries [40, 58–61]. The PCR primer pairs designed to flank the variable region of the phage genome allow reads aligned against the sequence of interest and amplified over PCR reactions. As the diversity of reads increases by 4-to-5-order of magnitude compared to the conventional plaque picking, it becomes crucial to narrow down datasets from the large NGS readouts in a way that investigators can rank and select manageable candidate phage clones for validation considering limited resource capacity is available to evaluate ligand specificity and selectivity in vitro and in vivo. A wide range of analytic algorithms and software have been developed to process and translate deep sequenced phage libraries. For example, multiple specificity identifier [71] and target-binding motif analysis [72] map peptide recognizing domains; FASTAptamer [73] and SORTCERY [74] perform sequence counting, normalization, and affinity ranking. While these algorithms provide valuable insight into affinity and specificity, ligand selectivity, an important factor in designing targeted therapeutics and imaging agents, was left out of the discussion.

To address this shortage, we have established a standardized process called Quantitative Selection of Available Targets (QSAT) that uses our previously developed computational algorithm, Phage Analysis for Selective Targeted PEPtides (PHASTpep) [49], to unbiasedly sift through phage libraries and identify targeting ligands. Compared to other computational deep sequencing software, QSAT is innovative by incorporating 1) a normalization algorithm that corrects library and amplification bias to allow cross-referencing between screens, libraries, targets, and animals and 2) motif clustering that uses a text searching program to find the significant motif families based on their physiochemical properties. These features allow the identification of highly selective and specific clones and comparison between multiple screens to form a peptide database for specific cell types or disease models (Figure 1.3). Indeed, the application of PHASTpep has been demonstrated in selecting peptides specific and selective for cancer-associated fibroblasts in pancreatic ductal adenocarcinoma in vitro [49]. In chapter 2, we

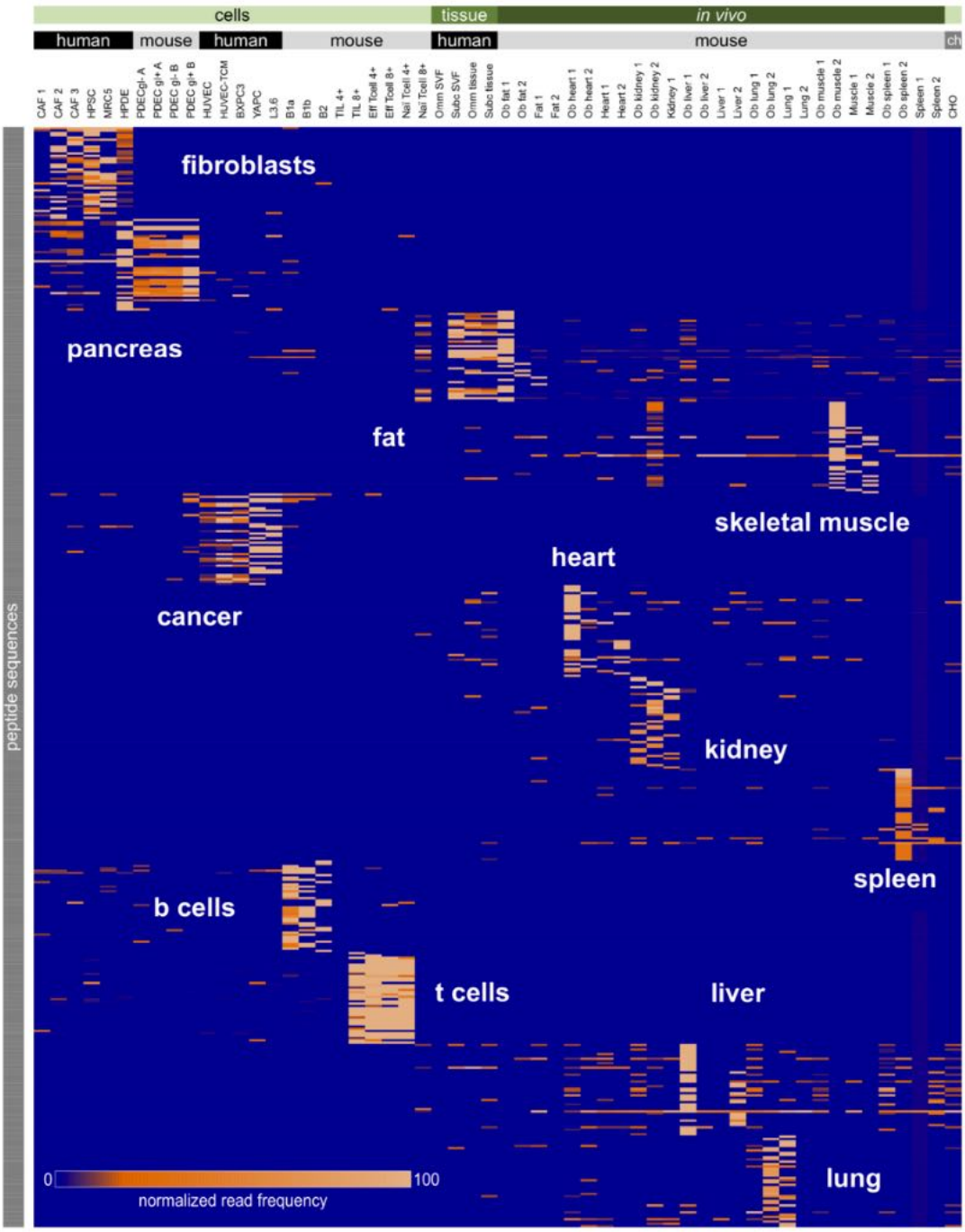

Figure 1.3. Peptide signatures of various cells and tissues. Peptides identified from screens performed on cell lines, ex vivo tissue specimens and in vivo screens were processed and analyzed using PHASTpep. They are presented as a heatmap generated via conditional formatting in Excel. PDEC, pancreatic ductal epithelial cell; gl, glucose; B, b cells; TIL, tumor infiltrating lymphocyte; Eff, effector; Omm, ommental; SVF, stromal vascular fraction; Ob, obese; CHO, chinese hamster ovary. Reprinted from [49].

will demonstrate the application of QSAT in analyzing in vivo NGS-phage display, which is a more diverse and complex system that involves more than a single cell type and a much higher background noise.

1.4.4 Leveraging phage display beyond ligand screening

Beyond ligand screening, target identification of the phage display-isolated molecules generates a mechanism whereby potential novel biomarkers of diseases can be ascertained. Target identification can be pursued using in silico database searching on Receptor Ligand Contacts (RELIC) [75], Artificially Selected Proteins/Peptides Database (ASPD) [76], and PepBank [77]. If the in silico methods of target identification produce too many or too few possible outcomes, experimental methods utilizing affinity chromatography may be employed. In affinity chromatography, biotin-peptides are used as “bait” and either incubated with the cell or tissues positive for binding or immobilized on a solid support, then incubated with the cell or tissues of interest [78]. In the first case, the peptide/target mixture is then incubated with streptavidin-coated beads, washed then eluted with excess biotin. In the second example, the beads/lysate mixture is washed then eluted with either free peptide or low pH buffers. The resulting eluate is then run on SDS/PAGE, and unique bands cut, digested with trypsin, then analyzed via mass spectroscopy to identify the target protein.

Target identification from disease-specific ligands not only reveals potential biomarkers, but the identified molecule may as well serve functional roles in disease biology, through which the molecular mechanism of a disease may be studied. For example, cell surface plectin was initially identified as a biomarker for pancreatic cancer epithelial cells using phage display. The follow-up research demonstrated the functional roles of plectin in proliferation, migration, and invasion in pancreatic ductal adenocarcinoma (PDAC) [79], prostate cancer [80], and hepatocellular carcinoma [81]. Hornerin is another protein that was discovered as the binding partner of an endothelial cell targeting peptide and later showed therapeutic potential in regulating vessel normalization in a PDAC mouse model [82]. All the above support that phage display can be leveraged beyond ligand identification to reveal novel mechanistic insights in disease.

1.5 Lack of effective molecular ligands for pancreatic diseases

Pancreatic diseases are worldwide public health issues and account for substantial health care utilization and spending. In the United States, annual health care expenditures for pancreatic combined with other gastrointestinal diseases total $135.9 billion, exceeding the amount spent on heart disease ($113.4 billion) [83]. Pancreatitis and PDAC made up the majority of exocrine pancreatic diseases. Acute pancreatitis (AP) is associated with high morbidity and a wide range of mortality rates (<10% to 85%) [84]. About 20% of AP patients develop recurrent events, and among which approximately 35% develop chronic pancreatitis (CP), resulting in exocrine and endocrine pancreatic insufficiency [76, 77]. While the survival rate of CP is high (70% at 10 years; 45% at 20 years [87]), patients with CP have a diminished quality of life and an increased risk of developing pancreatic cancer [78, 79]. Pancreatic cancer is the 12th most common cancer worldwide, with a global incidence rate of 4.8 per 100,000 persons [90]. In the United States, PDAC accounts for 3.2% of all new cancer cases (57,600 cases) in 2020 and is projected to become the 2nd leading cause of cancer-related death by 2030 [81, 82]. Up to date, pathogenesis for pancreatic diseases remains not fully understood, and options for effective therapy are limited [93].

Currently, there is no molecular targeting ligand available for acute or chronic pancreatitis. In order to reveal potential molecular targets, large-scale investigations in proteomics of pancreatitis have been performed by several groups. Chen et al. used ICAT labeling and tandem mass spectrometry-based proteomics to analyze tissues obtained from patients with CP and found differential expression of 116 proteins in CP, with the majority of them related to wound healing and inflammation [94]. Intriguingly, 40% of identified proteins are also associated with pancreatic cancer, suggesting commonality in protein expression between two diseases. Paulo et al. found four proteins (collagen α 1, filamin A, collagen α 3, and SNC73) exclusively expressed in CP by comparing tissue proteomes of CP to the normal pancreas and pancreatic cancer [95]. However, the study was performed on three specimens per group, and whether these proteins have diagnostic or therapeutic values remains to be validated. A more comprehensive and systematic proteomic evaluation is in need to allow the identification of highly selective and specific targeting ligands for pancreatitis. Therefore, we undertook to identify novel targeting

ligands for CP (chapter 2) and utilized these findings to design targeted liposomes for delivering antifibrotic small molecular drugs in CP (chapter 3).

Thus far, the discovery of targeting moieties has been focusing on targeting cancer epithelial cells in PDAC. Nanoparticles decorated with tumor cell targeted ligands to IGF1R [96], EGFR [97], or cell surface plectin-1 [98] for delivery of standard-of-care drugs showed promises in reducing tumor growth and toxicity profile in animal models. However, these approaches share a commonality with all standard PDAC therapies that they ignore the role of tumor microenvironment. PDAC is composed of extensive stroma that cancer-associated fibroblasts (CAFs), endothelial cells, and immune cells form complex networks with cancer cells and play an integral role in regulating tumor progression, immunosuppression, metastasis, and drug resistance [99–102]. A Recent study in proteomics of PDAC microenvironment revealed differential expression proteins secreted by stromal cells correlated with poor patient survival [104]. Using phage display, Gutknecht et al. identified a PDAC endothelial targeting peptide and showed the functional role of its receptor, hornerin, in regulating tumor vascularity [82]. These findings highlight the importance of understanding stromal proteome and the potential of revealing new targets with new molecular mechanism, which may pave the way for the development of novel therapeutic strategies that overcome low efficacy seen in current cancer cell-orientated treatments. Thus, in chapter 4 of this dissertation, we will use functional phage display-based proteomics to identify the binding partner of a CAF-targeted ligand and will evaluate the potential of a CAF-targeted liposomal formulation as a non-depletion, stromal-targeted strategy in pancreatic cancer.

In closing, targeting moieties and molecular targets provide means to developing target-specific interventions for pancreatic diseases. However, a challenging aspect to this realization is the lack of a high-throughput, analytical method to effectively select molecular ligands from disease models and allow in silico comparison between various diseased conditions. Thus, the overarching goal of this dissertation is to establish an in vivo phage display-based pipeline and utilize quantitative methods to advance the identification of targeting moieties and their molecular targets for pancreatic diseases.

1.6 Reference

[1] F. S. Collins and H. Varmus, “A New Initiative on Precision Medicine,” *N. Engl. J. Med.*, vol. 372, no. 9, pp. 793–795, Feb. 2015, doi: 10.1056/NEJMp1500523.

[2] B. Verstockt, K. G. Smith, and J. C. Lee, “Genome-wide association studies in Crohn’s disease: Past, present and future,” *Clin. Transl. Immunol.*, vol. 7, no. 1, Jan. 2018, doi: 10.1002/cti2.1001.

[3] A. N. Ananthakrishnan *et al.*, “Environmental triggers in IBD: a review of progress and evidence,” *Nat. Rev. Gastroenterol. Hepatol.*, vol. 15, no. 1, Art. no. 1, Jan. 2018, doi: 10.1038/nrgastro.2017.136.

[4] J. McIlroy, G. Ianiro, I. Mukhopadhya, R. Hansen, and G. L. Hold, “Review article: the gut microbiome in inflammatory bowel disease-avenues for microbial management,” *Aliment. Pharmacol. Ther.*, vol. 47, no. 1, pp. 26–42, Jan. 2018, doi: 10.1111/apt.14384.

[5] H. S. P. de Souza and C. Fiocchi, “Immunopathogenesis of IBD: current state of the art,” *Nat. Rev. Gastroenterol. Hepatol.*, vol. 13, no. 1, pp. 13–27, Jan. 2016, doi: 10.1038/nrgastro.2015.186.

[6] T. M. Allen, “Ligand-targeted therapeutics in anticancer therapy,” *Nat. Rev. Cancer*, vol. 2, no. 10, pp. 750–763, Oct. 2002, doi: 10.1038/nrc903.

[7] M. J. Mitchell, M. M. Billingsley, R. M. Haley, M. E. Wechsler, N. A. Peppas, and R. Langer, “Engineering precision nanoparticles for drug delivery,” *Nat. Rev. Drug Discov.*, vol. 20, no. 2, Art. no. 2, Feb. 2021, doi: 10.1038/s41573-020-0090-8.

[8] Y. (Chezy) Barenholz, “Doxil® — The first FDA-approved nano-drug: Lessons learned,” *J. Controlled Release*, vol. 160, no. 2, pp. 117–134, Jun. 2012, doi: 10.1016/j.jconrel.2012.03.020.

[9] A. H. Ko *et al.*, “A multinational phase 2 study of nanoliposomal irinotecan sucrosofate (PEP02, MM-398) for patients with gemcitabine-refractory metastatic pancreatic cancer,” *Br. J. Cancer*, vol. 109, no. 4, pp. 920–925, Aug. 2013, doi: 10.1038/bjc.2013.408.

[10] A. C. Krauss *et al.*, “FDA Approval Summary: (Daunorubicin and Cytarabine) Liposome for Injection for the Treatment of Adults with High-Risk Acute Myeloid Leukemia,” *Clin. Cancer Res. Off. J. Am. Assoc. Cancer Res.*, vol. 25, no. 9, pp. 2685–2690, May 2019, doi: 10.1158/1078-0432.CCR-18-2990.

[11] N. Hoshyar, S. Gray, H. Han, and G. Bao, “The effect of nanoparticle size on in vivo pharmacokinetics and cellular interaction,” *Nanomed.*, vol. 11, no. 6, pp. 673–692, Mar. 2016, doi: 10.2217/nnm.16.5.

[12] E. Beltrán-Gracia, A. López-Camacho, I. Higuera-Ciapara, J. B. Velázquez-Fernández, and A. A. Vallejo-Cardona, “Nanomedicine review: clinical developments in liposomal

applications," *Cancer Nanotechnol.*, vol. 10, no. 1, p. 11, Dec. 2019, doi: 10.1186/s12645-019-0055-y.

[13] K. Miller *et al.*, "HERMIONE: a randomized Phase 2 trial of MM-302 plus trastuzumab versus chemotherapy of physician's choice plus trastuzumab in patients with previously treated, anthracycline-naïve, HER2-positive, locally advanced/metastatic breast cancer," *BMC Cancer*, vol. 16, p. 352, Jun. 2016, doi: 10.1186/s12885-016-2385-z.

[14] S. S. K. Dasa *et al.*, "Plectin-targeted liposomes enhance the therapeutic efficacy of a PARP inhibitor in the treatment of ovarian cancer," *Theranostics*, vol. 8, no. 10, pp. 2782–2798, 2018, doi: 10.7150/thno.23050.

[15] C.-Y. Yeh, J.-K. Hsiao, Y.-P. Wang, C.-H. Lan, and H.-C. Wu, "Peptide-conjugated nanoparticles for targeted imaging and therapy of prostate cancer," *Biomaterials*, vol. 99, pp. 1–15, 2016, doi: 10.1016/j.biomaterials.2016.05.015.

[16] D.-K. Chang, C.-T. Lin, C.-H. Wu, and H.-C. Wu, "A novel peptide enhances therapeutic efficacy of liposomal anti-cancer drugs in mice models of human lung cancer," *PloS One*, vol. 4, no. 1, p. e4171, 2009, doi: 10.1371/journal.pone.0004171.

[17] C.-H. Wu, Y.-H. Kuo, R.-L. Hong, and H.-C. Wu, "α-Enolase-binding peptide enhances drug delivery efficiency and therapeutic efficacy against colorectal cancer," *Sci. Transl. Med.*, vol. 7, no. 290, p. 290ra91, Jun. 2015, doi: 10.1126/scitranslmed.aaa9391.

[18] X. Han, A. Aslanian, and J. R. Yates, "Mass Spectrometry for Proteomics," *Curr. Opin. Chem. Biol.*, vol. 12, no. 5, pp. 483–490, Oct. 2008, doi: 10.1016/j.cbpa.2008.07.024.

[19] F. Klont *et al.*, "Assessment of Sample Preparation Bias in Mass Spectrometry-Based Proteomics," *Anal. Chem.*, vol. 90, no. 8, pp. 5405–5413, Apr. 2018, doi: 10.1021/acs.analchem.8b00600.

[20] F. Meric-Bernstam *et al.*, "Influence of Biospecimen Variables on Proteomic Biomarkers in Breast Cancer," *Clin. Cancer Res.*, vol. 20, no. 14, pp. 3870–3883, Jul. 2014, doi: 10.1158/1078-0432.CCR-13-1507.

[21] E. C. Nice, "Challenges for omics technologies in the implementation of personalized medicine," *Expert Rev. Precis. Med. Drug Dev.*, vol. 3, no. 4, pp. 229–231, Jul. 2018, doi: 10.1080/23808993.2018.1505429.

[22] Y. Onogi, A. E. M. M. Khalil, and S. Ussar, "Identification and characterization of adipose surface epitopes," *Biochem. J.*, vol. 477, no. 13, pp. 2509–2541, Jul. 2020, doi: 10.1042/BCJ20190462.

[23] Z. Zhao, A. Ukidve, J. Kim, and S. Mitragotri, "Targeting Strategies for Tissue-Specific Drug Delivery," *Cell*, vol. 181, no. 1, pp. 151–167, Apr. 2020, doi: 10.1016/j.cell.2020.02.001.

[24] S. Waaijers *et al.*, "A tissue-specific protein purification approach in Caenorhabditis elegans identifies novel interaction partners of DLG-1/Discs large," *BMC Biol.*, vol. 14, p. 66, Aug. 2016, doi: 10.1186/s12915-016-0286-x.

[25] L. M. Schiapparelli, D. B. McClatchy, H.-H. Liu, P. Sharma, J. R. Yates, and H. T. Cline, "Direct detection of biotinylated proteins by mass spectrometry," *J. Proteome Res.*, vol. 13, no. 9, pp. 3966–3978, Sep. 2014, doi: 10.1021/pr5002862.

[26] D. I. Kim *et al.*, "An improved smaller biotin ligase for BioID proximity labeling," *Mol. Biol. Cell*, vol. 27, no. 8, pp. 1188–1196, Apr. 2016, doi: 10.1091/mbc.E15-12-0844.

[27] B. Lectez *et al.*, "Ubiquitin Profiling in Liver Using a Transgenic Mouse with Biotinylated Ubiquitin," *J. Proteome Res.*, vol. 13, no. 6, pp. 3016–3026, Jun. 2014, doi: 10.1021/pr5001913.

[28] A. Martinez *et al.*, "Quantitative proteomic analysis of Parkin substrates in Drosophila neurons," *Mol. Neurodegener.*, vol. 12, no. 1, p. 29, Apr. 2017, doi: 10.1186/s13024-017-0170-3.

[29] J. T. Ngo *et al.*, "Cell-selective metabolic labeling of proteins," *Nat. Chem. Biol.*, vol. 5, no. 10, pp. 715–717, Oct. 2009, doi: 10.1038/nchembio.200.

[30] I. Erdmann *et al.*, "Cell-selective labelling of proteomes in Drosophila melanogaster," *Nat. Commun.*, vol. 6, no. 1, Art. no. 1, Jul. 2015, doi: 10.1038/ncomms8521.

[31] T. S. Elliott *et al.*, "Proteome labeling and protein identification in specific tissues and at specific developmental stages in an animal," *Nat. Biotechnol.*, vol. 32, no. 5, Art. no. 5, May 2014, doi: 10.1038/nbt.2860.

[32] M. Grammel, M. M. Zhang, and H. C. Hang, "Orthogonal alkynyl-amino acid reporter for selective labeling of bacterial proteomes during infection," *Angew. Chem. Int. Ed Engl.*, vol. 49, no. 34, pp. 5970–5974, Aug. 2010, doi: 10.1002/anie.201002050.

[33] A. Mahdavi *et al.*, "A Genetically Encoded AND Gate for Cell-Targeted Metabolic Labeling of Proteins," *J. Am. Chem. Soc.*, vol. 135, no. 8, pp. 2979–2982, Feb. 2013, doi: 10.1021/ja400448f.

[34] A. Mahdavi *et al.*, "Engineered Aminoacyl-tRNA Synthetase for Cell-Selective Analysis of Mammalian Protein Synthesis," *J. Am. Chem. Soc.*, vol. 138, no. 13, pp. 4278–4281, Apr. 2016, doi: 10.1021/jacs.5b08980.

[35] A. Müller, A. Stellmacher, C. E. Freitag, P. Landgraf, and D. C. Dieterich, "Monitoring Astrocytic Proteome Dynamics by Cell Type-Specific Protein Labeling," *PLOS ONE*, vol. 10, no. 12, p. e0145451, Dec. 2015, doi: 10.1371/journal.pone.0145451.

[36] T. S. Elliott, A. Bianco, F. M. Townsley, S. D. Fried, and J. W. Chin, "Tagging and Enriching Proteins Enables Cell-Specific Proteomics," *Cell Chem. Biol.*, vol. 23, no. 7, pp. 805–815, Jul. 2016, doi: 10.1016/j.chembiol.2016.05.018.

[37] E. Ramberger and G. Dittmar, “Tissue Specific Labeling in Proteomics,” *Proteomes*, vol. 5, no. 3, Jul. 2017, doi: 10.3390/proteomes5030017.

[38] M. Krassowski, V. Das, S. K. Sahu, and B. B. Misra, “State of the Field in Multi-Omics Research: From Computational Needs to Data Mining and Sharing,” *Front. Genet.*, vol. 11, 2020, doi: 10.3389/fgene.2020.610798.

[39] G. P. Smith, “Filamentous fusion phage: novel expression vectors that display cloned antigens on the virion surface,” *Science*, vol. 228, no. 4705, pp. 1315–1317, Jun. 1985, doi: 10.1126/science.4001944.

[40] R. Ashfield and B. K. Jakobsen, “Making high-affinity T-cell receptors: a new class of targeted therapeutics,” *IDrugs Investig. Drugs J.*, vol. 9, no. 8, pp. 554–559, Aug. 2006.

[41] J. Marx, “New Insights Into Metastasis,” *Science*, vol. 294, no. 5541, pp. 281–282, Oct. 2001, doi: 10.1126/science.294.5541.281a.

[42] R. Hassan *et al.*, “Antitumor activity of SS(dsFv)PE38 and SS1(dsFv)PE38, recombinant antimesothelin immunotoxins against human gynecologic cancers grown in organotypic culture in vitro,” *Clin. Cancer Res. Off. J. Am. Assoc. Cancer Res.*, vol. 8, no. 11, pp. 3520–3526, Nov. 2002.

[43] A. E. Nixon, D. J. Sexton, and R. C. Ladner, “Drugs derived from phage display,” *mAbs*, vol. 6, no. 1, pp. 73–85, Jan. 2014, doi: 10.4161/mabs.27240.

[44] C. M. Y. Lee, N. Iorno, F. Sierro, and D. Christ, “Selection of human antibody fragments by phage display,” *Nat. Protoc.*, vol. 2, no. 11, pp. 3001–3008, 2007, doi: 10.1038/nprot.2007.448.

[45] A. Christiansen *et al.*, “High-throughput sequencing enhanced phage display enables the identification of patient-specific epitope motifs in serum,” *Sci. Rep.*, vol. 5, p. 12913, Aug. 2015, doi: 10.1038/srep12913.

[46] K. A. Kelly, M. Nahrendorf, A. M. Yu, F. Reynolds, and R. Weissleder, “In vivo phage display selection yields atherosclerotic plaque targeted peptides for imaging,” *Mol. Imaging Biol.*, vol. 8, no. 4, pp. 201–207, Aug. 2006, doi: 10.1007/s11307-006-0043-6.

[47] K. A. Kelly *et al.*, “Targeted nanoparticles for imaging incipient pancreatic ductal adenocarcinoma,” *PLoS Med.*, vol. 5, no. 4, p. e85, Apr. 2008, doi: 10.1371/journal.pmed.0050085.

[48] S. S. K. Dasa *et al.*, “Development of target-specific liposomes for delivering small molecule drugs after reperfused myocardial infarction,” *J. Control. Release Off. J. Control. Release Soc.*, vol. 220, no. Pt A, pp. 556–567, Dec. 2015, doi: 10.1016/j.jconrel.2015.06.017.

[49] L. T. Brinton, D. K. Bauknight, S. S. K. Dasa, and K. A. Kelly, “PHASTpep: Analysis Software for Discovery of Cell-Selective Peptides via Phage Display and Next-Generation

Sequencing," *PLOS ONE*, vol. 11, no. 5, p. e0155244, May 2016, doi: 10.1371/journal.pone.0155244.

[50] P. H. Faix, M. A. Burg, M. Gonzales, E. P. Ravey, A. Baird, and D. Larocca, "Phage display of cDNA libraries: enrichment of cDNA expression using open reading frame selection," *BioTechniques*, vol. 36, no. 6, pp. 1018–1029, Jun. 2004, doi: 10.2144/04366RR03.

[51] H. Dooley, M. F. Flajnik, and A. J. Porter, "Selection and characterization of naturally occurring single-domain (IgNAR) antibody fragments from immunized sharks by phage display," *Mol. Immunol.*, vol. 40, no. 1, pp. 25–33, Sep. 2003, doi: 10.1016/s0161-5890(03)00084-1.

[52] O. A. Mandrup, N. A. Friis, S. Lykkemark, J. Just, and P. Kristensen, "A novel heavy domain antibody library with functionally optimized complementarity determining regions," *PloS One*, vol. 8, no. 10, p. e76834, 2013, doi: 10.1371/journal.pone.0076834.

[53] R. Abraham, S. Buxbaum, J. Link, R. Smith, C. Venti, and M. Darsley, "Determination of binding constants of diabodies directed against prostate-specific antigen using electrochemiluminescence-based immunoassays," *J. Mol. Recognit. JMR*, vol. 9, no. 5–6, pp. 456–461, Dec. 1996, doi: 10.1002/(sici)1099-1352(199634/12)9:5/6<456::aid-jmr282>3.0.co;2-8.

[54] W. Arap *et al.*, "Steps toward mapping the human vasculature by phage display," *Nat. Med.*, vol. 8, no. 2, pp. 121–127, Feb. 2002, doi: 10.1038/nm0202-121.

[55] C. Liu, G. Bhattacharjee, W. Boisvert, R. Dilley, and T. Edgington, "In vivo interrogation of the molecular display of atherosclerotic lesion surfaces," *Am. J. Pathol.*, vol. 163, no. 5, pp. 1859–1871, Nov. 2003, doi: 10.1016/S0002-9440(10)63545-6.

[56] D. Rajotte, W. Arap, M. Hagedorn, E. Koivunen, R. Pasqualini, and E. Ruoslahti, "Molecular heterogeneity of the vascular endothelium revealed by in vivo phage display.," *J. Clin. Invest.*, vol. 102, no. 2, pp. 430–437, Jul. 1998.

[57] E. A. Peters, P. J. Schatz, S. S. Johnson, and W. J. Dower, "Membrane insertion defects caused by positive charges in the early mature region of protein pIII of filamentous phage fd can be corrected by prlA suppressors," *J. Bacteriol.*, vol. 176, no. 14, pp. 4296–4305, Jul. 1994, doi: 10.1128/jb.176.14.4296-4305.1994.

[58] A. Wada *et al.*, "Efficient Prostate Cancer Therapy with Tissue-Specific Homing Peptides Identified by Advanced Phage Display Technology," *Mol. Ther. Oncolytics*, vol. 12, pp. 138–146, Jan. 2019, doi: 10.1016/j.omto.2019.01.001.

[59] Y. Sui *et al.*, "Phage display screening identifies a prostate specific antigen (PSA)-/lo prostate cancer cell specific peptide to retard castration resistance of prostate cancer," *Transl. Oncol.*, vol. 14, no. 3, p. 101020, Mar. 2021, doi: 10.1016/j.tranon.2021.101020.

[60] D.-K. Chang *et al.*, “Antiangiogenic targeting liposomes increase therapeutic efficacy for solid tumors,” *J. Biol. Chem.*, vol. 284, no. 19, pp. 12905–12916, May 2009, doi: 10.1074/jbc.M900280200.

[61] M. Loi *et al.*, “Combined targeting of perivascular and endothelial tumor cells enhances anti-tumor efficacy of liposomal chemotherapy in neuroblastoma,” *J. Control. Release Off. J. Control. Release Soc.*, vol. 145, no. 1, pp. 66–73, Jul. 2010, doi: 10.1016/j.jconrel.2010.03.015.

[62] H.-Y. Hong *et al.*, “Detection of apoptosis in a rat model of focal cerebral ischemia using a homing peptide selected from in vivo phage display,” *J. Control. Release Off. J. Control. Release Soc.*, vol. 131, no. 3, pp. 167–172, Nov. 2008, doi: 10.1016/j.jconrel.2008.07.020.

[63] L. Larbanoix *et al.*, “Potential amyloid plaque-specific peptides for the diagnosis of Alzheimer’s disease,” *Neurobiol. Aging*, vol. 31, no. 10, pp. 1679–1689, Oct. 2010, doi: 10.1016/j.neurobiolaging.2008.09.021.

[64] C.-H. Wu, I.-J. Liu, R.-M. Lu, and H.-C. Wu, “Advancement and applications of peptide phage display technology in biomedical science,” *J. Biomed. Sci.*, vol. 23, Jan. 2016, doi: 10.1186/s12929-016-0223-x.

[65] B. P. Hodkinson and E. A. Grice, “Next-Generation Sequencing: A Review of Technologies and Tools for Wound Microbiome Research,” *Adv. Wound Care*, vol. 4, no. 1, pp. 50–58, Jul. 2014, doi: 10.1089/wound.2014.0542.

[66] K. H. Wong, Y. Jin, and Z. Moqtaderi, “Multiplex Illumina sequencing using DNA barcoding,” *Curr. Protoc. Mol. Biol.*, vol. Chapter 7, p. Unit 7.11., 2013, doi: 10.1002/0471142727.mb0711s101.

[67] J. Liu *et al.*, “Identification of antigen-specific human monoclonal antibodies using high-throughput sequencing of the antibody repertoire,” *Biochem. Biophys. Res. Commun.*, vol. 473, no. 1, pp. 23–28, Apr. 2016, doi: 10.1016/j.bbrc.2016.03.038.

[68] K. B. Turner, J. Naciri, J. L. Liu, G. P. Anderson, E. R. Goldman, and D. Zabetakis, “Next-Generation Sequencing of a Single Domain Antibody Repertoire Reveals Quality of Phage Display Selected Candidates,” *PLOS ONE*, vol. 11, no. 2, p. e0149393, Feb. 2016, doi: 10.1371/journal.pone.0149393.

[69] W. Yang, A. Yoon, S. Lee, S. Kim, J. Han, and J. Chung, “Next-generation sequencing enables the discovery of more diverse positive clones from a phage-displayed antibody library,” *Exp. Mol. Med.*, vol. 49, no. 3, p. e308, 24 2017, doi: 10.1038/emm.2017.22.

[70] A. Spiliotopoulos, Jonathan. P. Owen, Ben. C. Maddison, I. Dreveny, Helen. C. Rees, and Kevin. C. Gough, “Sensitive recovery of recombinant antibody clones after their in silico identification within NGS datasets,” *J. Immunol. Methods*, vol. 420, pp. 50–55, May 2015, doi: 10.1016/j.jim.2015.03.005.

[71] D. Gfeller *et al.*, “The multiple-specificity landscape of modular peptide recognition domains,” *Mol. Syst. Biol.*, vol. 7, p. 484, Apr. 2011, doi: 10.1038/msb.2011.18.

[72] I. Rentero Rebollo, M. Sabisz, V. Baeriswyl, and C. Heinis, “Identification of target-binding peptide motifs by high-throughput sequencing of phage-selected peptides,” *Nucleic Acids Res.*, vol. 42, no. 22, p. e169, Dec. 2014, doi: 10.1093/nar/gku940.

[73] K. K. Alam, J. L. Chang, and D. H. Burke, “FASTAptamer: A Bioinformatic Toolkit for High-throughput Sequence Analysis of Combinatorial Selections,” *Mol. Ther. Nucleic Acids*, vol. 4, p. e230, Mar. 2015, doi: 10.1038/mtna.2015.4.

[74] L. L. Reich, S. Dutta, and A. E. Keating, “SORTCERY-A High-Throughput Method to Affinity Rank Peptide Ligands,” *J. Mol. Biol.*, vol. 427, no. 11, pp. 2135–2150, Jun. 2015, doi: 10.1016/j.jmb.2014.09.025.

[75] S. Mandava, L. Makowski, S. Devarapalli, J. Uzubell, and D. J. Rodi, “RELIC--a bioinformatics server for combinatorial peptide analysis and identification of protein-ligand interaction sites,” *Proteomics*, vol. 4, no. 5, pp. 1439–1460, May 2004, doi: 10.1002/pmic.200300680.

[76] V. P. Valuev, D. A. Afonnikov, M. P. Ponomarenko, L. Milanesi, and N. A. Kolchanov, “ASPD (Artificially Selected Proteins/Peptides Database): a database of proteins and peptides evolved in vitro,” *Nucleic Acids Res.*, vol. 30, no. 1, pp. 200–202, Jan. 2002, doi: 10.1093/nar/30.1.200.

[77] T. Shtatland, D. Guettler, M. Kossodo, M. Pivovarov, and R. Weissleder, “PepBank--a database of peptides based on sequence text mining and public peptide data sources,” *BMC Bioinformatics*, vol. 8, p. 280, Aug. 2007, doi: 10.1186/1471-2105-8-280.

[78] D. Rajotte and E. Ruoslahti, “Membrane dipeptidase is the receptor for a lung-targeting peptide identified by in vivo phage display,” *J. Biol. Chem.*, vol. 274, no. 17, pp. 11593–11598, Apr. 1999, doi: 10.1074/jbc.274.17.11593.

[79] S. J. Shin *et al.*, “Unexpected gain of function for the scaffolding protein plectin due to mislocalization in pancreatic cancer,” *Proc. Natl. Acad. Sci.*, vol. 110, no. 48, pp. 19414–19419, Nov. 2013, doi: 10.1073/pnas.1309720110.

[80] M. Buckup *et al.*, “Plectin is a regulator of prostate cancer growth and metastasis,” *Oncogene*, vol. 40, no. 3, pp. 663–676, Jan. 2021, doi: 10.1038/s41388-020-01557-9.

[81] C.-C. Cheng *et al.*, “Transient knockdown-mediated deficiency in plectin alters hepatocellular motility in association with activated FAK and Rac1-GTPase,” *Cancer Cell Int.*, vol. 15, no. 1, p. 29, Mar. 2015, doi: 10.1186/s12935-015-0177-1.

[82] M. F. Gutknecht *et al.*, “Identification of the S100 fused-type protein hornerin as a regulator of tumor vascularity,” *Nat. Commun.*, vol. 8, no. 1, Art. no. 1, Sep. 2017, doi: 10.1038/s41467-017-00488-6.

[83] A. F. Peery *et al.*, “Burden and Cost of Gastrointestinal, Liver, and Pancreatic Diseases in the United States: Update 2018,” *Gastroenterology*, vol. 156, no. 1, pp. 254-272.e11, Jan. 2019, doi: 10.1053/j.gastro.2018.08.063.

[84] E. Zerem, “Treatment of severe acute pancreatitis and its complications,” *World J. Gastroenterol. WJG*, vol. 20, no. 38, pp. 13879–13892, Oct. 2014, doi: 10.3748/wjg.v20.i38.13879.

[85] G. M. Cavestro *et al.*, “A single-centre prospective, cohort study of the natural history of acute pancreatitis,” *Dig. Liver Dis.*, vol. 47, no. 3, pp. 205–210, Mar. 2015, doi: 10.1016/j.dld.2014.11.003.

[86] J. D. Machicado, S. T. Chari, L. Timmons, G. Tang, and D. Yadav, “A population-based evaluation of the natural history of chronic pancreatitis,” *Pancreatology*, vol. 18, no. 1, pp. 39–45, Jan. 2018, doi: 10.1016/j.pan.2017.11.012.

[87] A. Seicean, M. Tantău, M. Grigorescu, T. Mocan, R. Seicean, and T. Pop, “Mortality Risk Factors in Chronic Pancreatitis,” *J. Gastrointestin. Liver Dis.*, vol. 15, no. 1, Art. no. 1, Mar. 2006.

[88] D. Fitzsimmons *et al.*, “Symptoms and quality of life in chronic pancreatitis assessed by structured interview and the EORTC QLQ-C30 and QLQ-PAN26,” *Am. J. Gastroenterol.*, vol. 100, no. 4, pp. 918–926, Apr. 2005, doi: 10.1111/j.1572-0241.2005.40859.x.

[89] P. Bansal and A. Sonnenberg, “Pancreatitis is a risk factor for pancreatic cancer,” *Gastroenterology*, vol. 109, no. 1, pp. 247–251, Jul. 1995, doi: 10.1016/0016-5085(95)90291-0.

[90] F. Bray, J. Ferlay, I. Soerjomataram, R. L. Siegel, L. A. Torre, and A. Jemal, “Global cancer statistics 2018: GLOBOCAN estimates of incidence and mortality worldwide for 36 cancers in 185 countries,” *CA. Cancer J. Clin.*, vol. 68, no. 6, pp. 394–424, Nov. 2018, doi: 10.3322/caac.21492.

[91] R. L. Siegel, K. D. Miller, and A. Jemal, “Cancer statistics, 2020,” *CA. Cancer J. Clin.*, vol. 70, no. 1, pp. 7–30, Jan. 2020, doi: 10.3322/caac.21590.

[92] L. Rahib, B. D. Smith, R. Aizenberg, A. B. Rosenzweig, J. M. Fleshman, and L. M. Matrisian, “Projecting cancer incidence and deaths to 2030: the unexpected burden of thyroid, liver, and pancreas cancers in the United States,” *Cancer Res.*, vol. 74, no. 11, pp. 2913–2921, Jun. 2014, doi: 10.1158/0008-5472.CAN-14-0155.

[93] A. Y. Xiao *et al.*, “Global incidence and mortality of pancreatic diseases: a systematic review, meta-analysis, and meta-regression of population-based cohort studies,” *Lancet Gastroenterol. Hepatol.*, vol. 1, no. 1, pp. 45–55, Sep. 2016, doi: 10.1016/S2468-1253(16)30004-8.

[94] R. Chen *et al.*, “Quantitative Proteomics Analysis Reveals That Proteins Differentially Expressed in Chronic Pancreatitis Are Also Frequently Involved in Pancreatic Cancer*,”

Mol. Cell. Proteomics, vol. 6, no. 8, pp. 1331–1342, Aug. 2007, doi: 10.1074/mcp.M700072-MCP200.

[95] J. A. Paulo, L. S. Lee, P. A. Banks, H. Steen, and D. L. Conwell, "Proteomic analysis of formalin-fixed paraffin-embedded pancreatic tissue using liquid chromatography tandem mass spectrometry (LC-MS/MS)," *Pancreas*, vol. 41, no. 2, pp. 175–185, Mar. 2012, doi: 10.1097/MPA.0b013e318227a6b7.

[96] H. Zhou *et al.*, "IGF1 Receptor Targeted Theranostic Nanoparticles for Targeted and Image-Guided Therapy of Pancreatic Cancer," *ACS Nano*, vol. 9, no. 8, pp. 7976–7991, Aug. 2015, doi: 10.1021/acsnano.5b01288.

[97] A. Singh, J. Xu, G. Mattheolabakis, and M. Amiji, "EGFR-targeted gelatin nanoparticles for systemic administration of gemcitabine in an orthotopic pancreatic cancer model," *Nanomedicine Nanotechnol. Biol. Med.*, vol. 12, no. 3, pp. 589–600, Apr. 2016, doi: 10.1016/j.nano.2015.11.010.

[98] Y. Wu *et al.*, "Chimeric peptide supramolecular nanoparticles for plectin-1 targeted miRNA-9 delivery in pancreatic cancer," *Theranostics*, vol. 10, no. 3, pp. 1151–1165, 2020, doi: 10.7150/thno.38327.

[99] L. Monteran and N. Erez, "The Dark Side of Fibroblasts: Cancer-Associated Fibroblasts as Mediators of Immunosuppression in the Tumor Microenvironment," *Front. Immunol.*, vol. 10, Aug. 2019, doi: 10.3389/fimmu.2019.01835.

[100] Q. Sun *et al.*, "The impact of cancer-associated fibroblasts on major hallmarks of pancreatic cancer," *Theranostics*, vol. 8, no. 18, pp. 5072–5087, Oct. 2018, doi: 10.7150/thno.26546.

[101] B. C. Özdemir *et al.*, "Depletion of carcinoma-associated fibroblasts and fibrosis induces immunosuppression and accelerates pancreas cancer with reduced survival," *Cancer Cell*, vol. 25, no. 6, pp. 719–734, Jun. 2014, doi: 10.1016/j.ccr.2014.04.005.

[102] A. D. Rhim *et al.*, "Stromal elements act to restrain, rather than support, pancreatic ductal adenocarcinoma," *Cancer Cell*, vol. 25, no. 6, pp. 735–747, Jun. 2014, doi: 10.1016/j.ccr.2014.04.021.

[103] Y. Hiroshima *et al.*, "Novel targets identified by integrated cancer-stromal interactome analysis of pancreatic adenocarcinoma," *Cancer Lett.*, vol. 469, pp. 217–227, Jan. 2020, doi: 10.1016/j.canlet.2019.10.031.

[104] C. Tian *et al.*, "Proteomic analyses of ECM during pancreatic ductal adenocarcinoma progression reveal different contributions by tumor and stromal cells," *Proc. Natl. Acad. Sci. U. S. A.*, vol. 116, no. 39, pp. 19609–19618, Sep. 2019, doi: 10.1073/pnas.1908626116.

Chapter 2. High-throughput analytic selection of novel targeting ligands for chronic pancreatitis

This chapter is adapted from:
"High-throughput analytic selection of novel targeting ligands for chronic pancreatitis and development of target-specific liposomes for antifibrotic therapy".

Jessica Hung[1], Rohni Awasthi[1], Alexander L. Klibanov[2,3,4,5], Kimberly A. Kelly[2*]

1. Department of Biomedical Engineering, School of Engineering, University of Virginia, Charlottesville, Virginia, 22908, United States of America.
2. Department of Biomedical Engineering, School of Medicine, University of Virginia, Charlottesville, Virginia, 22908, United States of America.
3. Division of Cardiovascular Medicine, University of Virginia, Charlottesville, Virginia, 22908, United States of America.
4. Robert M. Berne Cardiovascular Research Center, University of Virginia, Charlottesville, Virginia, 22908, United States of America.
5. Department of Radiology, University of Virginia, Charlottesville, Virginia, 22908, United States of America.

*Corresponding Author. Email: kak3v@virginia.edu

Keywords: phage display, next-generation sequencing, peptide ligands, targeted liposomes, drug delivery

At this point, the text in this chapter has been submitted for peer review.

2.1 Abstract

Purpose: Chronic pancreatitis is a pancreatic inflammatory disorder that causes fibrosis, duct distortion, parenchymal calcification, and loss of exocrine and endocrine functions. Currently, there are no molecular targeting ligands or non-serum-based biomarkers are available, hindering the development of target-specific interventions. Thus, there is a need for an unbiased, comprehensive discovery and evaluation of pancreatitis-specific ligands.

Methods: In the present study, we utilized a computational-guided in vivo phage display approach to select peptide ligands specific to the caerulein-induced mouse model of chronic pancreatitis. Fluorescent imaging modalities were used to validate the ligand specificity to the inflamed pancreas.

Results: We have incorporated four analyses, including PHASTpep, replicability, enrichment, and clustering analysis, to guild ligand selection from in vivo NGS-phage display of CP. Except for clustering based on the Hobohm algorithm, these methods have successfully discovered seven phage clones that demonstrated increased accumulation in the CP over the healthy pancreas.

Conclusion: In summary, we have developed a systematic approach to guide ligand selection in an in vivo NGS-phage display and profile peptide ligands specific for complex disease models.

2.2 Introduction

Chronic pancreatitis (CP) is an inflammatory disorder that causes irreversible damage in the pancreas and induces long-standing sequelae encompassing recurrent severe pain, fibrosis, duct distortion, parenchymal calcification, and loss of exocrine and endocrine functions at the advanced stage [1, 2]. In addition to physical debilities, patients with CP typically struggle with psychological and financial challenges, resulting in significantly impaired quality of life measures [3, 4]. Patients with a history of CP have an increased risk of developing pulmonary diseases, diabetes mellitus, and pancreatic cancer [5]. The annual incidence of CP worldwide ranges between 5-12 per 100,000 populations, with an approximate prevalence of 50 per 100,000 [6]. Despite low prevalence, the frequent demands of pain management and necessary procedures directly or indirectly caused by CP lead to a disproportional high cost of medical care, inducing an impactful socioeconomic burden on diseased individuals and the health care system in the United States [7, 8].

The lack of molecular targeting ligands and non-serum-based biomarkers hinders the development of targeted interventions for CP. Phage display has been widely used in identifying novel targeting moieties in various biological systems [9]. Despite cell-based in vitro phage display offers a simple and efficient approach to select targeting ligands, its application is limited when there are no stable cell lines available to recapitulate the molecular or cellular profiles of a diseased condition. In addition, in vivo phage display exposes naive libraries to heterogenous repertoires while being subject to the body's clearance system; thus, preselecting homing probes that are less likely to be removed by the reticuloendothelial system, which is a preferable feature in designing targeted drug delivery or imaging agents. Through performing in vivo phage screening in caerulein-induced mouse model of CP, which shares similar morphological features as human pancreatitis, we aim to identify phage clones specific to the inflamed pancreas.

Recent adaptations of next-generation sequencing (NGS) into phage display have increased the sequencing capacity and helped address pitfalls of conventional phage screening, including low-throughput and high false-positive rates [10–12]. While many analytic algorithms and software have been developed to process deep-sequenced phage libraries and guide ligand selection from in vitro screens, little has been explored on their robustness in identifying

targeting moieties in NGS-based in vivo screens. Thus, we have established a standardized process called Quantitative Selection of Available Targets (QSAT) that built upon our previously developed computational algorithm, Phage Analysis for Selective Targeted PEPtides (PHASTpep) [13], and incorporated three other algorithms (replicability, enrichment, and clustering analysis) to provide in silico prediction of disease-specific ligands for in vivo biopanning in the healthy and CP pancreas. From QSAT, we selected 18 candidate clones for validation using fluorescent imaging modalities and showed 7 clones are specific to CP. In this chapter, we demonstrated that QSAT is a high-throughput, robust, and efficient mythology of interpreting the outcomes of the in vivo phage screening, and through which, targeting moieties for CP were identified.

2.3 Methods

2.3.1 Fluorophores for ex vivo imaging and antibodies for immunostaining

Fluorophore VivoTag 680 (VT680), and VivoTag S-750 (VT750) were purchased from PerkinElmer, Waltham, MA, to guide tracking of phage clones by ex vivo imaging systems.

2.3.2 Caerulein-induced pancreatitis in mice

C57BL/6 J mice (6-12 week-old, female) were used for the in vivo phage screening. For chronic pancreatitis, caerulein (Bachem, Torrance, CA) was dissolved in sterile saline and administrated to mice twice a day, 8 hours apart for 14 consecutive days, at a concentration of 250 μg/kg body weight via intraperitoneal injection [14], as shown in Figure S2.1A. During the 14-day course, intraperitoneal injections of 100 μg/kg buprenorphine were given every 3 days to minimize the induced pain. For healthy controls, c57BL/6 J mice were injected intraperitoneally with an equal volume of sterile saline following the same schedule as in the chronic pancreatitis models. All animal experiments were approved by the Animal Care and Use Committee at the University of Virginia and conformed to the NIH “Guide for the Care and Use of Laboratory Animals in Research.” The inflammatory status of the pancreas was confirmed at the end of caerulein treatments via immunohistochemistry using hematoxylin-eosin (H&E) and picrosirius red (Polysciences, Inc., Warrington, PA) staining (Figure S2.1B).

2.3.3 In vivo phage screening

$1x10^{12}$ plaque-forming units (pfu) of the Ph.D.™-7 Phage Display Peptide Library (New England Biolabs, Ipswich, MA) were injected intravenously into CP and healthy c57BL/6J mice (N=3, each) via tail vein. Phage were allowed to circulate in the blood system for 4h post-injection to allow extravasation out of the bloodstream and into tissues to facilitate cellular binding before the mice were euthanized. Various organs including heart, liver, spleen, pancreas, kidneys, and skeletal muscle, were harvested, weighed, and homogenized in a lysis buffer: 1x EDTA and 1x protease inhibitor cocktail (Fisher Scientific, Hampton, NH) in Dulbecco's phosphate-buffered saline (DPBS, HyClone, Logan, UT). Phage titers of the tissues were determined by bacteriophage plaque assay following the manufacturer's instructions (Ph.D.™ Phage Display Libraries Instruction Manual, NEB) and calculated in percent injected dose (%ID) per organ-weight. Phage recovered from the pancreas pool were amplified in *Escherichia coli* strain ER2738 at the early-log phase in LB media for 5h at 37℃. Bacterial debris were spun down at 12,000 rpm, 10 min, and phage in the supernatant were purified via PEG precipitation (PEG/NaCl: 20% w/v polyethylene glycol-8000, 2.5mM NaCl) overnight at 4℃. The amplified phage were then washed with DPBS, precipitated again with PEG/NaCl at 4℃ for 30 min, centrifuged, and resuspended in DPBS for the next round of biopanning. Three rounds of biopanning were performed in both CP and healthy mice.

2.3.4 Phage DNA sequencing

Thirty phage plaques from the pancreas of round-3 were randomly selected for DNA sequencing. The insert oligo in the integrated section of the phage was amplified by polymerase chain reaction (PCR) using the forward primer, 5'-CCTTTAGTGGTACCTTTCTAT-3', and the reverse primer, 5'-GCCCTCATAGTTAGCGTAACG-3', and then Sanger sequenced (Eurofins) (Figure S2.2). Phage DNA of the pancreas pooled at all rounds was extracted using sodium iodide precipitation, followed by PCR amplification using previously published primer sets [13] with KAPA HiFi PCR kit (Fisher Scientific, Hampton, NH). The PCR cycles are initialized with one step of 95℃ for 1min, followed by 17 cycles of 95℃ for 30 s, 60℃ for 30 s, and 72℃ for 30 s. PCR purification was performed using a QIAquick PCR purification kit (Qiagen, Hilden, Germany) following the

manufacturer's instructions. Phage DNA was sent to the UVA Biomolecular Research Core Facility for single-ended Next-generation sequencing (NGS) on an Illumina Miseq Sequencer. FASTA files generated from the Illumina sequencing were processed by PHASTpep software previously published [13]. In brief, PHASTpep recognizes and translates the inserted DNA sequences into 7-amino acids peptides. Combining with the reads obtained from NGS of the NEB naïve PhD library used for screening, PHASTpep generates matrices of ranked, normalized read frequencies, and the corresponding sequences.

2.3.5 Specificity of phage clones

After PHASTpep analysis and candidate clone selection, 18 candidate clones were grouped (4-5 clones per group, 4 groups total) based on sequence similarity using GibbsCluster Server 2.0 [15] by the Technical University of Denmark (Figure S2.3A). Phage clones were pooled in equimolar amounts and labeled with fluorophore VivoTag 680 (VT680, PerkinElmer, Waltham, MA). Wild type M13Ke phage, used as the negative control to account for phage background bindings, was labeled with VivoTag S-750 (VT750, PerkinElmer, Waltham, MA). For each group, the fluorescently labeled candidate and WT phage were mixed and co-injected in CP and healthy mice (n = 5). Phage accumulation was determined by measuring the ex vivo fluorescent intensity of the pancreas at 20h post-injection using the IVIS Spectrum Series (Perkin Elmer, Waltham, MA) using the excitation and emission wavelength at 675nm/720nm for VT680 and 745nm/800nm for VT750. To account for variations of fluorescent labeling efficiency, the raw readouts of VT680 and VT750 were normalized to the dye-per-phage ratio (Figure S2.3B). The specificity ratio was calculated as %ID/g of the normalized VT680 divided by the %ID/g of the normalized VT750 (Figure S2.3C). A similar procedure was applied to determine the specificity of individual phage clones in group 2 and 3. Fluorescent intensity was measured at 20h post-injection of candidate phage (VT680) and WT phage (VT750). Fold change of specificity ratio was calculated as the specificity ratio of CP mice divided by the specificity ratio of the healthy mouse (Table S3.1).

2.3.6 Statistical analysis

Statistical analysis of the data was performed by student t-test, one-way analysis of variance (ANOVA) and Tukey-Kramer test. All data presented are expressed as mean$\pm$ standard error of at least three independent measurements. For all comparisons, p-value < 0.05 was considered significant.

2.4 Results

2.4.1 Enrichment of phage clones specific to the inflamed pancreas.

The Kelly laboratory has pioneered methods to identify novel ligands and targets for various diseases [13, 16–18]. To select phage clones that bind specifically to cells in the complex CP microenvironment, an in vivo phage display screen was performed by injecting the phage library into the caerulein-induced CP mouse model (Figure 2.1A). The PhD.7 phage library ($1x10^{12}$ pfu per mouse) was injected via tail vein in CP mice and allowed to circulate for 4h before animals were euthanized to allow extravasation out of the bloodstream and into tissues to facilitate cellular binding. Phage harvested from the pancreas were amplified and re-injected into CP animals for a total of 3 rounds of biopanning. For each round, tissues other than pancreas were also harvested and phage titered to determine selectivity of the phage pool for CP pancreas. After three rounds of selection, the phage titer in the CP pancreas showed a statistically significant increase from round 1 (0.89 %ID/g) and round 2 (0.39 %ID/g) to round 3 (14.38 %ID/g) (Figure 2.1B). Phage titers in the clearance organs, including liver, spleen, and kidneys, decreased over rounds, implying the selectivity of phage pools shifted towards the inflamed tissues over the enrichment process as expected for a successful enrichment process. At the end of round 3, we Sanger (30 clones per animal, N = 3) and deep sequenced phage clones isolated from pancreata to identify CP-specific peptides using an in silico selection approach from the enriched phage pools.

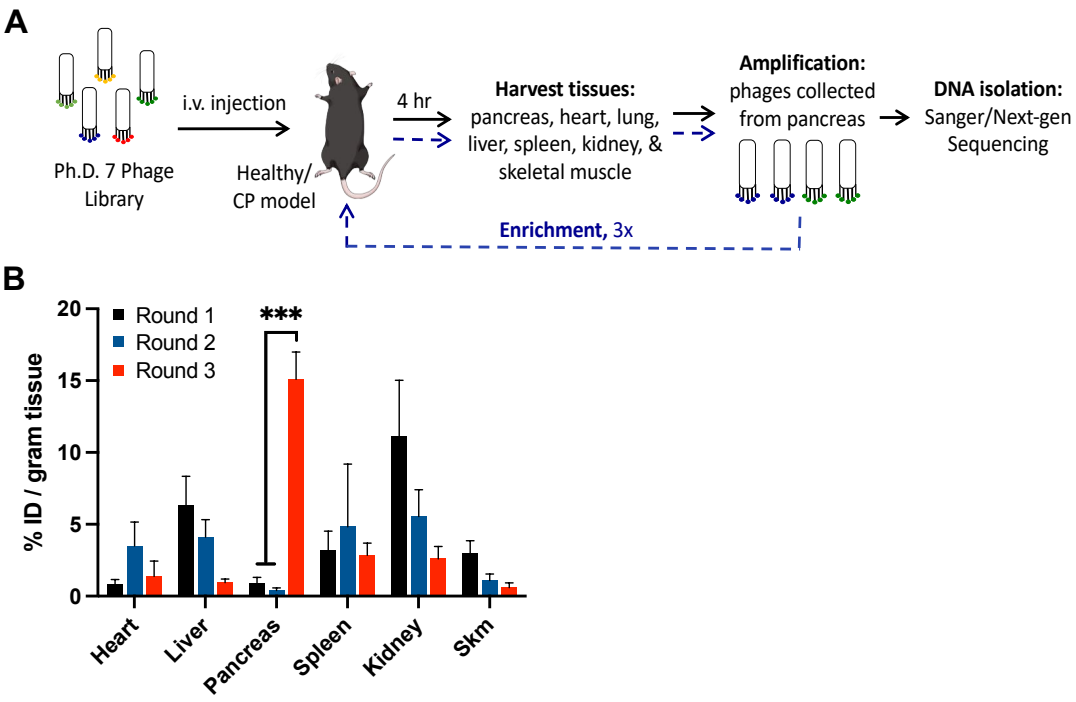

Figure 2.1. In vivo phage screening in the chronic pancreatitis mouse model. (A) A schematic of the in vivo phage biopanning process to screen for clones specific for CP pancreas. (B) Phage titering of in vivo phage screening in caerulein-induced CP mice. Phage pools (% injected dose per gram tissue) were recovered from the pancreas and various organs in 3 rounds of the biopanning process. One-way ANOVA and Tukey-Kramer tests were used to compare round 3 vs. round 1, and round 3 vs. round 2. N = 3; ***p<0.0001. Skm: Skeletal muscle.

2.4.2 QSAT: In silico selection of CP-specific candidate clones.

While many analytic algorithms and software have been developed to process deep-sequenced phage libraries and guide ligand selection from in vitro screens, little has been explored on their robustness in identifying targeting moieties in NGS-based in vivo screens. Previously, our lab has developed the Phage Analysis for Selective Targeted PEPtides (PHASTpep) software to identify target-specific phage clones in screening against recombinant proteins and cells in culture [13]. However, we have not evaluated its efficacy in processing phage pools present with thousands of available targets expressed in the multiple cell types as seen in an in vivo screen. Moreover, in addition to the caerulien-treated mice, we also screened pancreata from the healthy mice of the same mouse strain to ensure the selected clones possess high

selectivity for the inflamed pancreas. In order to achieve in silico comparison on phage pools obtained from the healthy and the CP pancreas, we sought to evaluate four different analytical methods to guide candidate clone selection. In addition to PHASTpep, replicability, clone enrichment, and homologous motifs were also evaluated to address different aspects of biases that could affect selecting algorithms. The identified candidate clones from these four methods were compared to the Kelly laboratory database of all previous phage display experiments. This step functions as an in silico negative selection to remove any phage clone that appears in multiple screens and would therefore, be non-specific or non-selective and capable of binding to multiple targets.

2.4.2.1 PHASTpep for clone selection

Conventional clone picking suffers from high false-positive rates and lacks a robust approach to select target-specific candidate clones. To address this issue, we used the NGS frequency counts from round 3 to allow quantitative sorting. To ensure specificity, PHASTpep normalized each individual clone's frequency count in the target screens to that in the naïve library screen (normalized frequency) to account for amplification and library biases [13]. To ensure selectivity for CP pancreas over the healthy pancreas, normalized frequency of clones from CP pancreas screen were compared with pancreas from healthy animals. Of the 90 clones that Sanger sequencing methods alone would have identified, only 6 clones were selected as meeting the criteria of high normalized frequency counts in the CP pancreas (>50) but low accumulation in the healthy pancreas (<10) (Figure 2.2). This selection criteria ensured a 5~10-fold higher expression of phage clone in the inflamed over benign pancreas. It also removed a non-specific phage clone, ADARYKS [19, 20], from the candidate list, which would have been selected using Sanger sequencing alone since it was the most abundant clone among clones picked (10%).

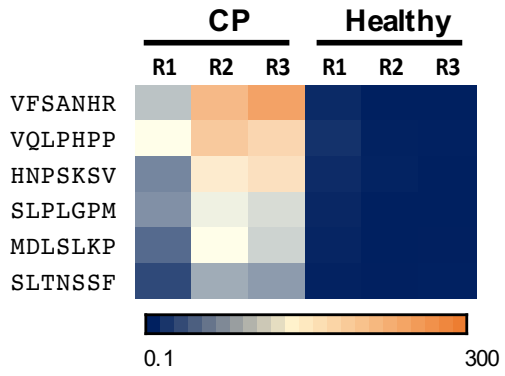

Figure 2.2. Candidate clones selected by PHASTpep.

2.4.2.2 Replicability between libraries.

Lot-to-lot variations of naïve libraries may induce amino acid distribution bias and skew the screening results [21]. Indeed, we observed sequence distribution variabilities in the two PhD7 phage libraries used for the in vivo screens (Figure 2.3A). Lot 1 is dominated by clones that appear less than 10 copies (60% of 1 copy; 28% of 1~10 copies). Lot 2, however, contains a less diverse population but the majority of clones have 100~10000 copies (40% of 100~1000 copies; 25% of 1000~10000 copies). This kind of variability is inherent in the commercially available phage libraries and will affect the screening results. Therefore, we developed a method to take the variability into account and normalize the data in order to be able to compare the sequences from every screen. This allows better selectivity as we can rapidly remove phage clones that are present across multiple diverse selection, which represent non-specific or non-selective binders. To elucidate the variability, we calculated the mean and standard deviation of the normalized frequency of a clone across two lots of phage display libraries (n=3 animals) and selected those clones with coefficient of variant (CV) <1 (CV = the ratio of the standard deviation to the mean) and that have a minimum of 5-fold increase expression in CP over healthy pancreas (Figure 2.3B). Of 9 clones that meet these criteria, 3 unique clones, LVWPAPN, MNSIAIP & SANITNL, were selected.

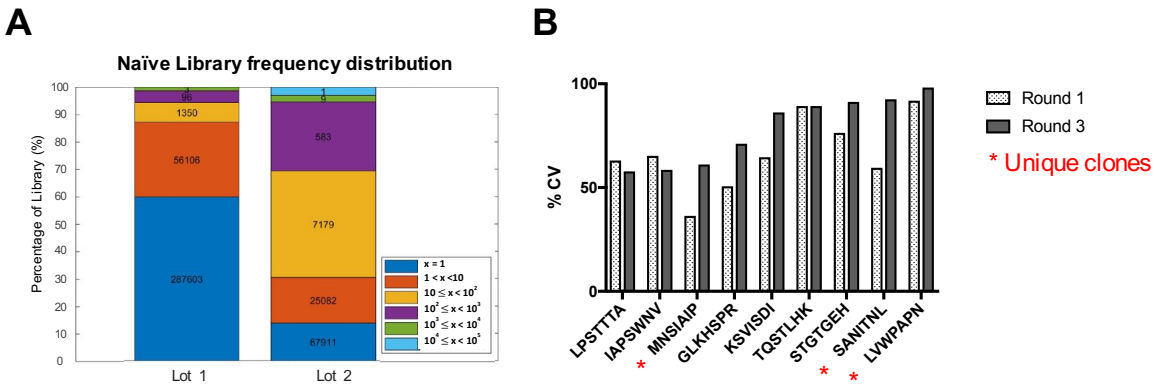

Figure 2.3. Candidate clones selected by replicability. (A) NEB's PhD7 Naïve libraries present high sequence variabilities among two lots we used for in vivo screening for CP. (B) Percent coefficient variant (% CV) of all clones that have normalized frequency counts of round 3 above 20 in the CP screen and below 4 in the healthy pancreas screen of all rounds.

2.4.2.3 Clone enrichments over rounds.

During biopanning, high-affinity binders and/or clones binding to targets with high expression tend to remain in the eluates and be enriched after amplifications. This process is indicated by a clone's increasing frequency present over rounds. As limited amounts (<0.0001%) of clones were sequenced in the traditional clone picking, the loss of potential candidate clones occurs early in the biopanning process, making direct comparisons of individual clone's frequency change between rounds not as informative. With NGS, several orders of magnitude in the quantity of sequences in the library are obtained, enabling the calculation of a more reflective growth rate for each clone in silico. Therefore, we can utilize the growth rate (GR), determined by the ratio of the numbers of clones present between rounds, to select high-affinity clones. In notation, $GR_{2(3)1}$ = frequency in round 2(3) / frequency in round 1. We noticed that the enriched clones do not necessarily go through constant growth in every round. Instead, some clones reached the peak frequency at round 2 then decreased in round 3. To ensure that the analysis was not skewed toward burst growth in a single round of selection, we processed reads in round 2 and 3 in parallel and found intersectional clones that fulfilled both analyses (Figure 2.4A). Compared to reads in round 1, 48 clones were identified from the top 60 frequency counts and a positive growth based on the round 2 reads (Figure 2.4B). The same criteria applied in reads from round 3 resulted in 14 clones (Figure 2.4C). Out of 63 clones selected in parallel, we selected 9 clones that appeared in both analyses (Figure 2.4D). Using this method, we identified clones that would have been discarded using conventional clone picking alone.

2.4.2.4 Homologous motif identification using Hobohm clustering analysis.

As protein interactions are often determined by a few amino acids, motifs conferring phage binding to its target can be repeatedly seen among different clones in the same screen. Recognizing target-specific homology families can offer insights to the libraries that would have been missed when evaluating each sequence as an independent read. Therefore, we clustered phage pools using the Hobohm algorithm [22] to reveal homologous motifs in the CP screens. Hobohm clustering identifies homologous motifs based on the Levenshtein distance [23] between peptide sequences. The smaller Levenshtein distance scores reflect a higher similarity

A

Selection Criteria	Tot # of clones	% Overlap (#) between R2 & R3
1. Top 60 frequency in R2 or R3	120	88.3% (53)
2. $Freq_{all\ rounds}$ in WT <25	110	87.3% (48)
3. GR_2/GR_1 or GR_3/GR_1 >1	63	28.6% (9)

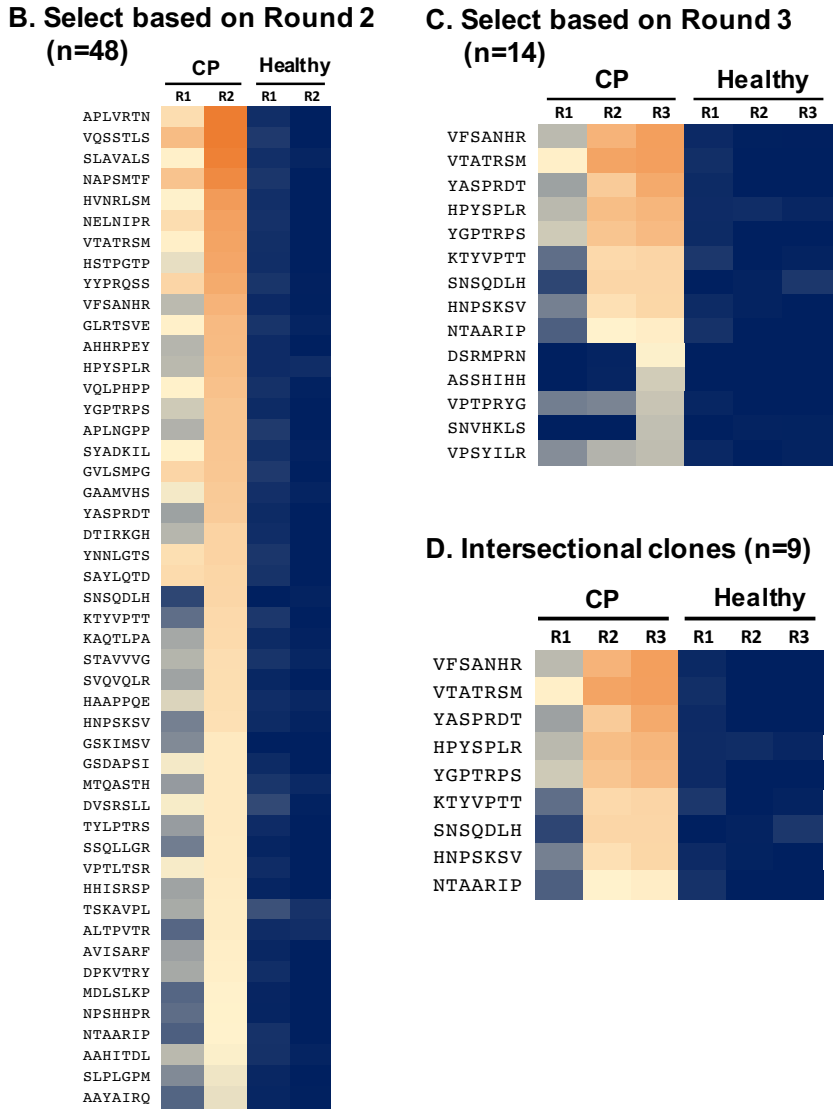

Figure 2.4. Candidate clones selected by enrichments. (A) Selection criteria and percent intersectional clones between round 2 (R2) and round 3 (R3) analysis. (B) 48 clones were identified using enrichment criteria based on reads in round 2. (C) 14 clones were identified using enrichment criteria based on reads in round 3. (D) The two parallel analyses resulted in 9 intersectional clones.

between two strings, thus, a more likely motif (Figure 2.5A). After motifs were identified, the frequency ranks of all peptides in each motif were added up to calculate the total rank sum of the motif. For each motif, we compared the rank sum in the CP screens (i.e., target rank sum) to that in the healthy pancreas screens (i.e., control rank sum) to delineate motifs that favor CP screens. Two clones, QMHARGD and HSGLNKQ, from the two statistically significant (p-value < 0.01) motif families were selected based on their target selectivity and growth rate (Figure 2.5B and C).

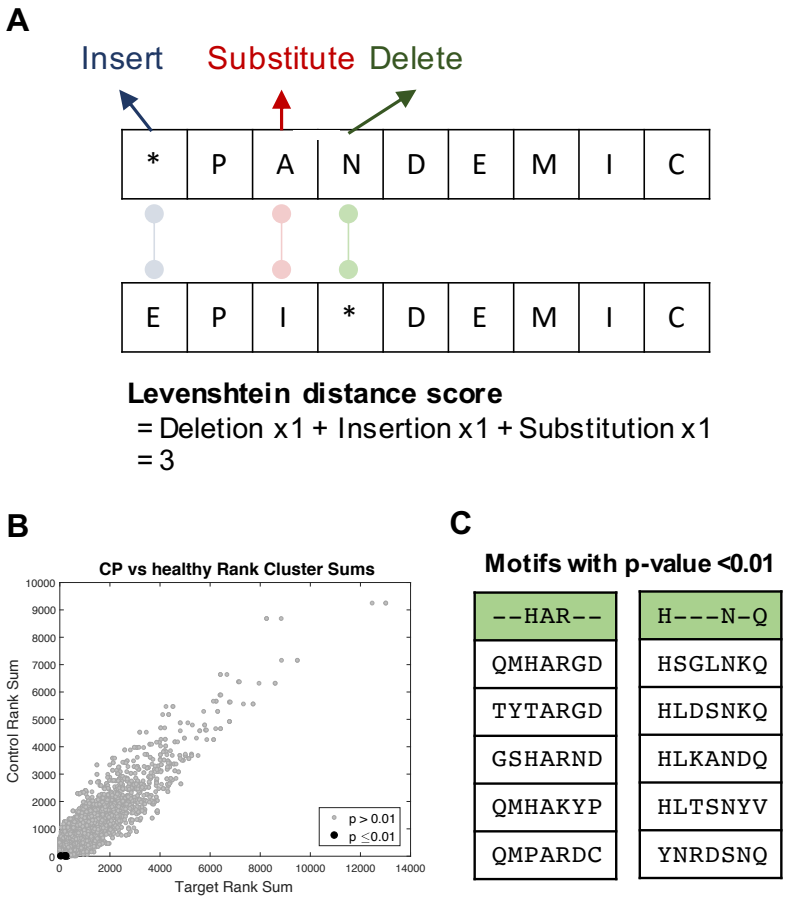

Figure 2.5. Candidate clones selected by Hobohm clustering analysis. (A) The Hobohm algorithm calculates Levenshtein distance [23] to assign scores for sequence similarities. Here we show an example of aligning two similar strings to calculate the least number of edit operations (insertion, deletion, and substitution) required to modify one sting to another. (B) After motifs were identified, a total rank sum was generated by summing the ranks of all peptides existed in each motif. The rank was assigned from the lowest frequency counts to the highest. Healthy screens were used as a control to help delineate motifs that favor CP screens. (C) Significant motifs identified by Hobohm clustering for the CP screens (p<0.01).

2.4.3 In vivo validation of phage clones specific to the inflamed pancreas.

After combining the 4 analysis methods and determining selectivity using the Kelly laboratory database of phage screens that contains tissue-specific phage clones [13], we selected 18 candidate clones for further validation. To efficiently evaluate 18 candidate clones, we divided them into 4 groups (Figure S2.3A) based on sequence similarity using GibbsCluster Server 2.0. [24]. Phage in the selected group and the wildtype M13Ke phage were fluorescently conjugated to fluorophore VT680 and VT750, respectively, pooled then were intravenously injected via tail vein into healthy or CP mice. At 20h post-injection, ex vivo ratiometric imaging of targeted-to-M13Ke phage analysis revealed a significantly higher accumulation of targeting phage clones from group 2 and 3 in the CP pancreas when compared with pancreas from healthy mice ($p<0.05$, Figure 2.6A). A total number of 9 individual clones gathered from group 2 and 3 were subsequently screened individually for their specificity for the inflamed pancreas. Seven out of

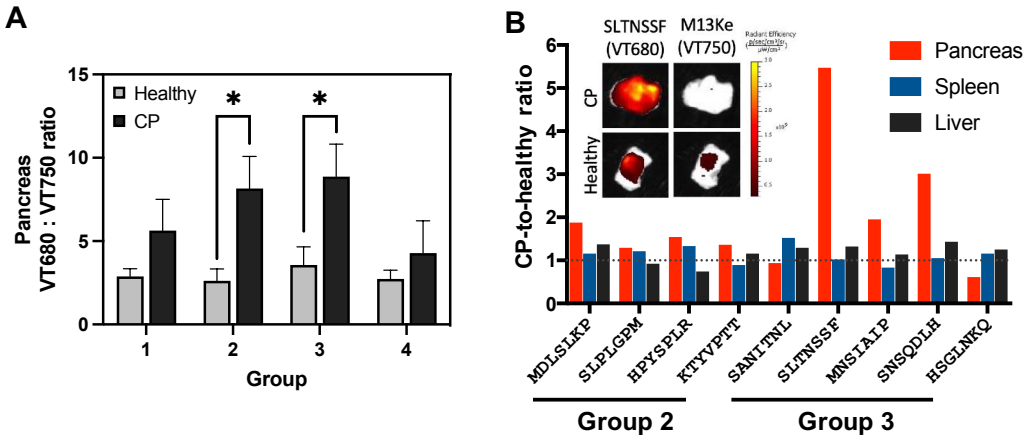

Figure 2.6. In vivo validation of CP targeting candidate clones. (A) Phage clone specificity validation by homology groups revealed preferential bindings of Group 2 and 3 targeting clones to CP pancreas over the healthy pancreas. N = 5. Mean ± SEM. A student t-test was used to compare the targeting phage (VT680)-to-wild type phage (VT750) ratio in CP versus the same ratio in the healthy pancreas. *p-value < 0.05 (p = 0.0275 for Group 2; p = 0.0443 for Group 3). (B) Phage clones from Group 2 and 3 were validated individually in both healthy and CP mice. Fold change represents the ratio of targeting-to-wild type ratio in CP over healthy mice. 7/9 clones showed higher phage accumulation in CP over healthy pancreas (fold change >1).

nine clones (MDLSLKP, SLPLGPM, HPYSPLR, KTYVPTT, SLTNSSF, MNSIAIP, and SNSQDLH) showed increased specificity for CP over healthy pancreas (Figure 2.6B). From the validation results, we concluded that PHASTpep-guided selection, replicates and enrichment algorithm can reveal sequences specific for CP pancreas from an in vivo screen. That none of the clones identified from clustering analysis showed specificity to CP could be a result of the diverse available targets present in tissues, thus, increasing the difficulty to converge valid motifs.

2.5 Discussion

Chronic pancreatitis is a complex inflammatory pancreatic disease that remains incurable [25–28]. Current treatments for CP are limited to palliative care and pain alleviation, and these approaches fail at the advanced stage when invasive surgical procedures such as endoscopic interventions, bypass, and total pancreatectomy are the only available options [29]. The pancreatic community has recently reached a consensus that precision medicine can provide a more sophisticated approach for complex disorders like CP to assist the development of target-specific interventions [28]. Despite omics-based technology being widely used to profile disease-specific biomarkers and therapeutic targets in many diseases [30, 31], transcriptomics reveals little about CP-specific pathways due to the universal genetic backgrounds shared between pancreatitis, pancreatic cancer, and the benign pancreas [32]. Looking only in epithelial cells, Sanh et al. showed differential expression in 34 proteins in malignant and pancreatitis pancreas compared to the benign tissue, but were not able to distinguish pancreatitis from pancreatic cancer [33]. Considering the heterogeneity of cellular components involved in disease progression of CP, there is a definite need to provide an unbiased, comprehensive evaluation of pancreatitis-associated proteomes.

In this chapter, we utilized a computational-guided in vivo phage display approach to profile 7-mer peptide ligands selective for cellular components in the caerulein-induced CP mouse pancreas. In contrast to indirect proteomic techniques, phage display allows probing of proteins in their native context during biopanning, thus increasing clinical relevance of the identified targeting agents [34]. Additionally, in vivo screening ensures identifying targeting agents with high selectivity as deselections or subtractions for all other tissues are carried out

while enrichment occurs in the target tissue [16]. By comparing the in vivo screens against CP, benign pancreas, and pancreatic cancer using our database we were able to ensure peptide selectivity to the diseased pancreas by not choosing peptides in any condition but CP. Phage display combined with Illumina NGS overcomes conventional biopanning limitations, including high false-positive rates and lack of a robust analytical target selection method [35]. Using the PHASTpep-guided approach, our team has successfully identified peptides specific for pancreatic cancer-associated fibroblasts in vitro [13]. Here, we expanded the application in analyzing in vivo phage screens and assessed the identified phage clones with live animal imaging modalities and fluorescent microscopy to show peptide specificity towards inflamed pancreas.

Selecting targeting moieties from an in vivo phage screen has been difficult as it is a more complex system that involves thousands of available targets expressed in multiple cell types. PHASTpep has established rigorous algorithms to transform NGS reads into meaningful frequency counts. However, its application has not been validated for in vivo phage display. In this chapter, we explored four different analysis methods: PHASTpep, replicability, enrichment, and clustering analysis, and selected 18 candidate clones from the CP screens based on these methods. Of all, 7 phage clones that showed increased accumulation in CP over the healthy pancreas were identified using PHASTpep (2), replicability (1), and enrichment (4) analyses. Based on the total amount and the quality (specificity to CP) of the specific clones predicted, PHASTpep and enrichment analyses both contribute to effective ligand selection and are recommended to be used for future in vivo screens. Motifs finding using the Hobohm algorithms, however, failed to discover CP-specific ligands. This could be the result of highly diverse targets present in the in vivo screens significantly increases the diversity of phage pools and surpasses the sequence alignment capacity of the algorithm to provide a meaningful prediction. A more complex algorithm that facilitates multiple protein-protein interactions in large-scale datasets could pave the way to reveal homologous motifs for in vivo NGS-phage display.

2.6 Conclusion

We have developed a systematic approach to reveal targeting moieties for in vivo NGS-phage display. Using our developed method, we have identified seven 7-mer peptides that show

specificity to CP. Taking the advantage of phage display, this approach requires no prior knowledge of the target and can be easily translated to other diseases of interest if representative animal models existed. The results of this work provide tools to mediate the development of target-specific interventions for CP.

2.7 Acknowledgments

The authors would like to thank Y. Bao of the UVA Biomolecular Research Core Facility for NGS; M. Bevard of the UVA Cardiovascular Research Center histology core for paraffin embedding and IHC staining. The work was supported by NIH (R21 CA231196-01, R01 CA233716-01 A1) and NCI (P30 CA044579-26).

2.8 Author Contributions

Conceptualization (JH, ALK, KAK), data curation (JH, RA), formal analysis (JH), investigation (JH, RA, ALK, KAK), methodology (JH, RA, ALK, KAK), project administration (KAK), supervision (ALK, KAK), visualization (JH), writing – original draft (JH), and writing – review & editing (JH, RA, ALK, KAK).

2.9 Declaration of Interests

The authors declare that Dr. Kelly is the CEO and Founder of ZielBio, Inc. ZielBio played no role in funding this work. JH, RA, and ALK declare no conflicts of interest in this work.

2.10 Reference

[1] B. Etemad and D. C. Whitcomb, “Chronic pancreatitis: diagnosis, classification, and new genetic developments,” *Gastroenterology*, vol. 120, no. 3, pp. 682–707, Feb. 2001, doi: 10.1053/gast.2001.22586.

[2] G. Klöppel, “Pathology of chronic pancreatitis and pancreatic pain,” *Acta Chir. Scand.*, vol. 156, no. 4, pp. 261–265, Apr. 1990.

[3] K. Morgan, S. M. Owczarski, J. Borckardt, A. Madan, M. Nishimura, and D. B. Adams, “Pain Control and Quality of Life After Pancreatectomy with Islet Autotransplantation for Chronic Pancreatitis,” *J. Gastrointest. Surg.*, vol. 16, no. 1, pp. 129–134, Jan. 2012, doi: 10.1007/s11605-011-1744-y.

[4] J. D. Machicado *et al.*, “Quality of Life in Chronic Pancreatitis is Determined by Constant Pain, Disability/Unemployment, Current Smoking, and Associated Co-Morbidities,” *Am. J. Gastroenterol.*, vol. 112, no. 4, pp. 633–642, 2017, doi: 10.1038/ajg.2017.42.

[5] U. C. Bang, T. Benfield, L. Hyldstrup, F. Bendtsen, and J.-E. Beck Jensen, “Mortality, cancer, and comorbidities associated with chronic pancreatitis: a Danish nationwide matched-cohort study,” *Gastroenterology*, vol. 146, no. 4, pp. 989–994, Apr. 2014, doi: 10.1053/j.gastro.2013.12.033.

[6] D. Yadav and A. B. Lowenfels, “The epidemiology of pancreatitis and pancreatic cancer,” *Gastroenterology*, vol. 144, no. 6, pp. 1252–1261, Jun. 2013, doi: 10.1053/j.gastro.2013.01.068.

[7] T. C. Hall, G. Garcea, M. A. Webb, D. Al-Leswas, M. S. Metcalfe, and A. R. Dennison, “The socio-economic impact of chronic pancreatitis: a systematic review,” *J. Eval. Clin. Pract.*, vol. 20, no. 3, pp. 203–207, Jun. 2014, doi: 10.1111/jep.12117.

[8] J. Ting *et al.*, “Direct Costs of Acute Recurrent and Chronic Pancreatitis in Children in the INSPPIRE Registry,” *J. Pediatr. Gastroenterol. Nutr.*, vol. 62, no. 3, pp. 443–449, Mar. 2016, doi: 10.1097/MPG.0000000000001057.

[9] C.-H. Wu, I.-J. Liu, R.-M. Lu, and H.-C. Wu, “Advancement and applications of peptide phage display technology in biomedical science,” *J. Biomed. Sci.*, vol. 23, Jan. 2016, doi: 10.1186/s12929-016-0223-x.

[10] J. Liu *et al.*, “Identification of antigen-specific human monoclonal antibodies using high-throughput sequencing of the antibody repertoire,” *Biochem. Biophys. Res. Commun.*, vol. 473, no. 1, pp. 23–28, Apr. 2016, doi: 10.1016/j.bbrc.2016.03.038.

[11] K. B. Turner, J. Naciri, J. L. Liu, G. P. Anderson, E. R. Goldman, and D. Zabetakis, “Next-Generation Sequencing of a Single Domain Antibody Repertoire Reveals Quality of Phage

Display Selected Candidates," *PLOS ONE*, vol. 11, no. 2, p. e0149393, Feb. 2016, doi: 10.1371/journal.pone.0149393.

[12] W. Yang, A. Yoon, S. Lee, S. Kim, J. Han, and J. Chung, "Next-generation sequencing enables the discovery of more diverse positive clones from a phage-displayed antibody library," *Exp. Mol. Med.*, vol. 49, no. 3, p. e308, 24 2017, doi: 10.1038/emm.2017.22.

[13] L. T. Brinton, D. K. Bauknight, S. S. K. Dasa, and K. A. Kelly, "PHASTpep: Analysis Software for Discovery of Cell-Selective Peptides via Phage Display and Next-Generation Sequencing," *PLOS ONE*, vol. 11, no. 5, p. e0155244, May 2016, doi: 10.1371/journal.pone.0155244.

[14] C. J. Halbrook *et al.*, "Mitogen-activated Protein Kinase Kinase Activity Maintains Acinar-to-Ductal Metaplasia and Is Required for Organ Regeneration in Pancreatitis," *Cell. Mol. Gastroenterol. Hepatol.*, vol. 3, no. 1, pp. 99–118, Jan. 2017, doi: 10.1016/j.jcmgh.2016.09.009.

[15] M. Andreatta, O. Lund, and M. Nielsen, "Simultaneous alignment and clustering of peptide data using a Gibbs sampling approach," *Bioinforma. Oxf. Engl.*, vol. 29, no. 1, pp. 8–14, Jan. 2013, doi: 10.1093/bioinformatics/bts621.

[16] S. S. K. Dasa *et al.*, "Development of target-specific liposomes for delivering small molecule drugs after reperfused myocardial infarction," *J. Control. Release Off. J. Control. Release Soc.*, vol. 220, no. Pt A, pp. 556–567, Dec. 2015, doi: 10.1016/j.jconrel.2015.06.017.

[17] D. Bausch *et al.*, "Plectin-1 as a novel biomarker for pancreatic cancer," *Clin. Cancer Res. Off. J. Am. Assoc. Cancer Res.*, vol. 17, no. 2, pp. 302–309, Jan. 2011, doi: 10.1158/1078-0432.CCR-10-0999.

[18] M. F. Gutknecht *et al.*, "Identification of the S100 fused-type protein hornerin as a regulator of tumor vascularity," *Nat. Commun.*, vol. 8, no. 1, Art. no. 1, Sep. 2017, doi: 10.1038/s41467-017-00488-6.

[19] D. Kroiss, J. M. Aramini, S. A. McPhee, T. Tuttle, and R. V. Ulijn, "Unbiased Discovery of Dynamic Peptide-ATP Complexes," *ChemSystemsChem*, vol. 1, no. 1–2, pp. 7–11, 2019, doi: 10.1002/syst.201900013.

[20] "Part:BBa K2043011:Design - parts.igem.org." http://parts.igem.org/Part:BBa_K2043011:Design (accessed Sep. 04, 2019).

[21] A. Ryvkin, H. Ashkenazy, Y. Weiss-Ottolenghi, C. Piller, T. Pupko, and J. M. Gershoni, "Phage display peptide libraries: deviations from randomness and correctives," *Nucleic Acids Res.*, vol. 46, no. 9, p. e52, 18 2018, doi: 10.1093/nar/gky077.

[22] "String::Cluster::Hobohm - Cluster strings using the Hobohm algorithm - metacpan.org." https://metacpan.org/pod/String::Cluster::Hobohm (accessed Sep. 04, 2019).

[23] V. Levenshtein, “Binary codes capable of correcting deletions, insertions, and reversals,” *Sov. Phys. Dokl.*, vol. 10, no. 8, pp. 707–710, 1965.

[24] M. Andreatta, B. Alvarez, and M. Nielsen, “GibbsCluster: unsupervised clustering and alignment of peptide sequences,” *Nucleic Acids Res.*, vol. 45, no. W1, pp. W458–W463, Jul. 2017, doi: 10.1093/nar/gkx248.

[25] D. C. Whitcomb *et al.*, “Chronic pancreatitis: An international draft consensus proposal for a new mechanistic definition,” *Pancreatol. Off. J. Int. Assoc. Pancreatol. IAP Al*, vol. 16, no. 2, pp. 218–224, Apr. 2016, doi: 10.1016/j.pan.2016.02.001.

[26] D. C. Whitcomb, “Peering Into the ‘Black Box’ of the Complex Chronic Pancreatitis Syndrome,” *Pancreas*, vol. 45, no. 10, pp. 1361–1364, Nov. 2016, doi: 10.1097/MPA.0000000000000715.

[27] D. C. Whitcomb *et al.*, “International consensus statements on early chronic Pancreatitis. Recommendations from the working group for the international consensus guidelines for chronic pancreatitis in collaboration with The International Association of Pancreatology, American Pancreatic Association, Japan Pancreas Society, PancreasFest Working Group and European Pancreatic Club,” *Pancreatol. Off. J. Int. Assoc. Pancreatol. IAP Al*, May 2018, doi: 10.1016/j.pan.2018.05.008.

[28] M. E. Lowe *et al.*, “Precision Medicine in Pancreatic Disease-Knowledge Gaps and Research Opportunities: Summary of a National Institute of Diabetes and Digestive and Kidney Diseases Workshop,” *Pancreas*, vol. 48, no. 10, pp. 1250–1258, Dec. 2019, doi: 10.1097/MPA.0000000000001412.

[29] J. G. D‘Haese(1), D. L. Cahen(2), and J. Werner(1), “Current Surgical Treatment Options in Chronic Pancreatitis,” *Pancreapedia Exocrine Pancreas Knowl. Base*, Aug. 2016, doi: 10.3998/panc.2016.26.

[30] H. Matthews, J. Hanison, and N. Nirmalan, “‘Omics’-Informed Drug and Biomarker Discovery: Opportunities, Challenges and Future Perspectives,” *Proteomes*, vol. 4, no. 3, Sep. 2016, doi: 10.3390/proteomes4030028.

[31] Y. Hasin, M. Seldin, and A. Lusis, “Multi-omics approaches to disease,” *Genome Biol.*, vol. 18, no. 1, p. 83, May 2017, doi: 10.1186/s13059-017-1215-1.

[32] S. Li, R. Li, H. Wang, L. Li, H. Li, and Y. Li, “The Key Genes of Chronic Pancreatitis which Bridge Chronic Pancreatitis and Pancreatic Cancer Can be Therapeutic Targets,” *Pathol. Oncol. Res. POR*, vol. 24, no. 2, pp. 215–222, Apr. 2018, doi: 10.1007/s12253-017-0217-3.

[33] N. Sanh *et al.*, “Proteomics Profiling of Pancreatic Cancer and Pancreatitis for Biomarkers Discovery,” *J. Cell Sci. Ther.*, vol. 9, no. 4, 2018, doi: 10.4172/2157-7013.1000287.

[34] Y. Onogi, A. E. M. M. Khalil, and S. Ussar, “Identification and characterization of adipose surface epitopes,” *Biochem. J.*, vol. 477, no. 13, pp. 2509–2541, Jul. 2020, doi: 10.1042/BCJ20190462.

[35] C. Juds *et al.*, “Combining Phage Display and Next-Generation Sequencing for Materials Sciences: A Case Study on Probing Polypropylene Surfaces,” *J. Am. Chem. Soc.*, vol. 142, no. 24, pp. 10624–10628, Jun. 2020, doi: 10.1021/jacs.0c03482.

2.11 Supplement

Figure S2.1. Caerulein-induced CP mouse model. (A) Caerulein injection schedule. (B) Pancreas H&E and Picrosirius red staining of healthy c57bl/6j and caerulein-induced CP mice. Acinar cell atrophy (black arrows) and fibroblast/immune cell infiltrations (red arrows) are observed in CP mice. Brightfield 25x.

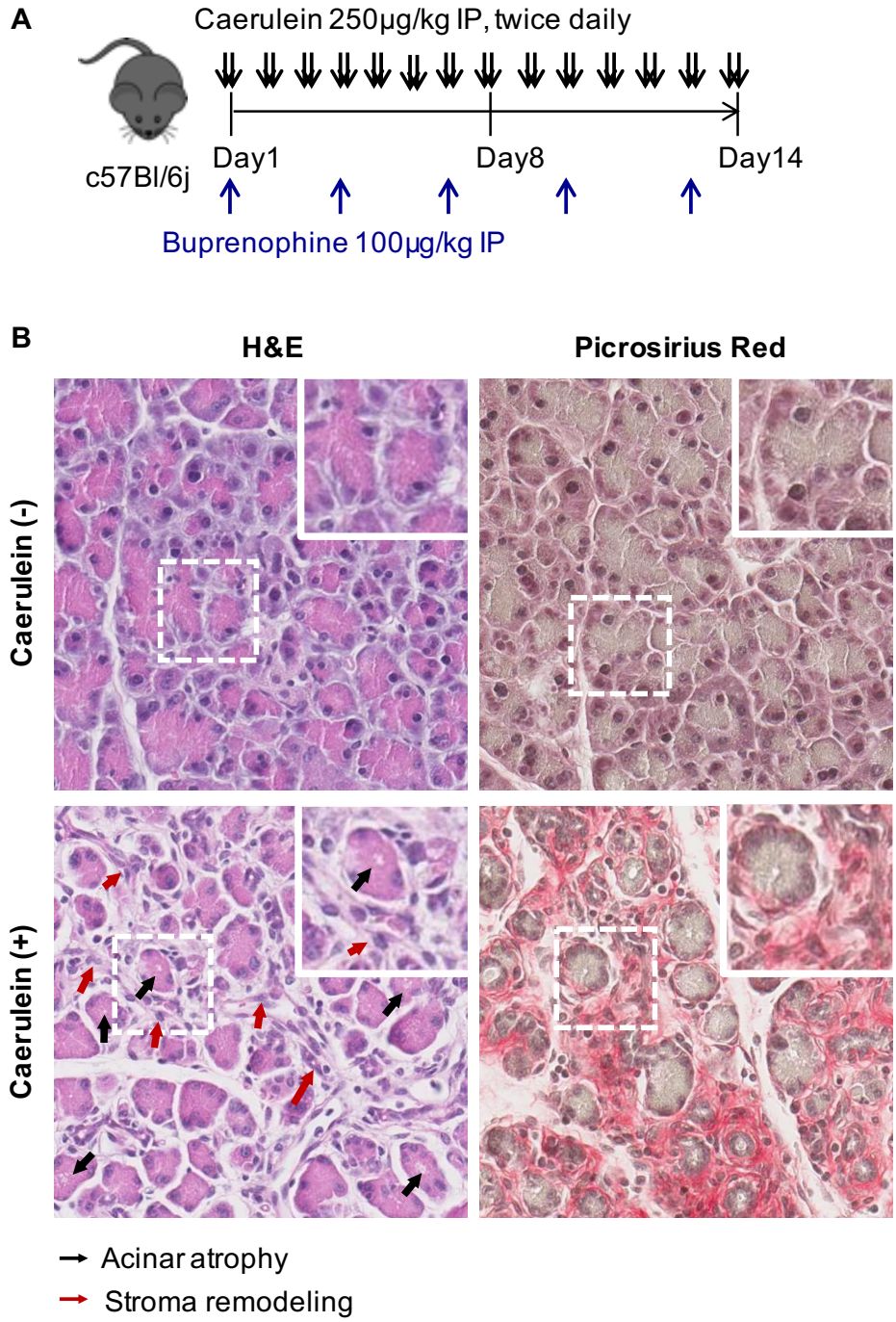

Figure S2.2 Phage cloning of 18 CP-targeting candidate clones. (A) The PCR products of the cloned candidate phage DNA were run on 1.5% agarose gel. A visualizable size difference in base pair (b.p.) was observed in candidate phage compared to the wildtype M13Ke phage, matching the theoretical 21 nucleotides inserts in the cloned phage. (B) The nucleotide sequence of the insert region was Sanger sequenced and translated to amino acid sequence.

A

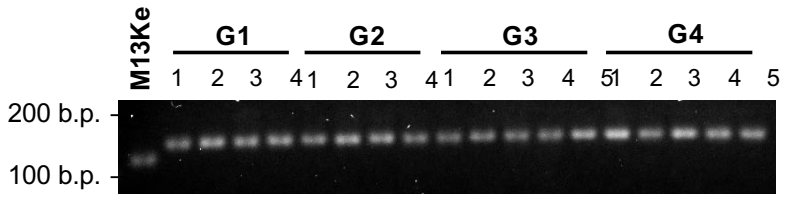

B

Clone ID	Nucleotide sequence of the insert region	Amino acid sequence
M13Ke	...ACCTCCACCAGAGTGAGA...	–
G1 #1	...ACCTCCACC**GTCACCACGAGCGTGCATCTG**AGAGTGAGA...	QMHARGD
G1 #2	...ACCTCCACC**AGGGATTCTAGCAGCGGTGTT**AGAGTGAGA...	NTAARIP
G1 #3	...ACCTCCACC**CATAGAACGGGTAGCGGTAAC**AGAGTGAGA...	VTATRSM
G1 #4	...ACCTCCACC**AGACGGACGGGTCGGACCGTA**AGAGTGAGA...	YGPTRPS
G2 #1	...ACCTCCACC**CGGCTTCAGCGACAGATCCAT**AGAGTGAGA...	MDLSLKP
G2 #2	...ACCTCCACC**CATCGGACCCAGAGGCAGAGA**AGAGTGAGA...	SLPLGPM
G2 #3	...ACCTCCACC**ACGCAGCGGAGAGTACGGGTG**AGAGTGAGA...	HPYSPLR
G2 #4	...ACCTCCACC**GGTGGTCGGAACGTAGGTTTT**AGAGTGAGA...	KTYVPTT
G3 #1	...ACCTCCACC**CAGGTTGGTGATGTTAGCAGA**AGAGTGAGA...	SANITNL
G3 #2	...ACCTCCACC**AAAACTACTATTAGTAAGCGA**AGAGTGAGA...	SLTNSSF
G3 #3	...ACCTCCACC**AGGAATCGCAATCGAATTCAT**AGAGTGAGA...	MNSIAIP
G3 #4	...ACCTCCACC**CTGTTTGTTCAGACCAGAGTG**AGAGTGAGA...	SNSQDLH
G3 #5	...ACCTCCACC**CTGTTTGTTCAGACCAGAGTG**AGAGTGAGA...	HSGLNKQ
G4 #1	...ACCTCCACC**GTTCGGAGCCGGCCAAACCAG**AGAGTGAGA...	LVWPAPN
G4 #2	...ACCTCCACC**CGGCGGATGCGGAAGCTGAAC**AGAGTGAGA...	VQLPHPP
G4 #3	...ACCTCCACC**CCGATGATTAGCAGAAAAAAC**AGAGTGAGA...	VFSANHR
G4 #4	...ACCTCCACC**GGTGTCACGCGGAGAAGCGTA**AGAGTGAGA...	YASPRDT
G4 #5	...ACCTCCACC**AACAGACTTCGAAGGATTATG**AGAGTGAGA...	HNPSKSV

Figure S2.3. Candidate clones grouping and fluorescent labeling. (A) Candidate clones grouping based on sequence similarity by GibbsCluster Server 2.0. for group validation. (B) Table of fluorescent labeling of candidate phage clones. (C) Equations to calculate normalized percent injected dose (%ID) per tissue weight and VT680-to-VT750 ratio.

A

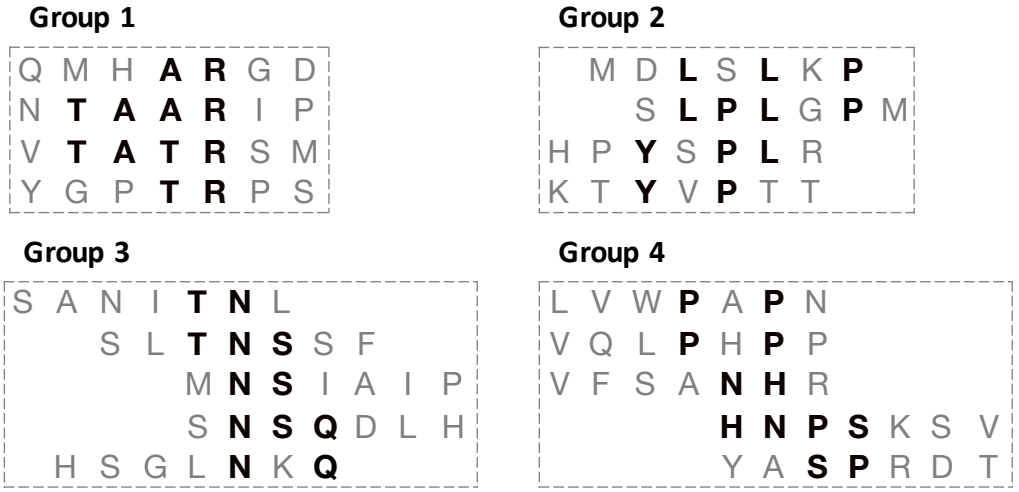

B

Group	# Dye per phage (CP; Healthy)	Phage injected (pfu) equil. to 1nmol dye (CP; Healthy)
1	182.44 ± 29.25 191.36 ± 37.08	$3.08 \times 10^{11} \pm 4.17 \times 10^{10}$ $2.93 \times 10^{11} \pm 5.44 \times 10^{10}$
2	233.43 ± 19.23 215.99 ± 20.35	$4.32 \times 10^{11} \pm 1.42 \times 10^{11}$ $4.82 \times 10^{11} \pm 1.24 \times 10^{11}$
3	234.32 ± 31.21 212.04 ± 35.68	$3.14 \times 10^{11} \pm 7.68 \times 10^{10}$ $4.02 \times 10^{11} \pm 5.10 \times 10^{10}$
4	240.93 ± 37.01 203.53 ± 35.50	$3.36 \times 10^{11} \pm 8.78 \times 10^{10}$ $4.35 \times 10^{11} \pm 6.76 \times 10^{10}$
WT	321.09 ± 45.03 376.06 ± 20.37	$5.18 \times 10^{11} \pm 6.69 \times 10^{10}$ $3.70 \times 10^{11} \pm 2.13 \times 10^{10}$

C

$$\%ID/g = \frac{dye\ in\ panc}{phage\ injected \times dye/phage} \times \frac{1}{mass_{panc}} \times 100\%$$

$$\text{VT680-to-VT750 ratio} = \frac{\%ID/g_{VT680}}{\%ID/g_{VT750}}$$

Table S2.1. Phage clone individual validation raw data and calculation.

		Organ		Targeting Phage-VT680				M13Ke Phage-VT750				Radiant efficiency Targeting:M13Ke
Phage	Mouse model	Organ	weight (mg)	# of phage injected	# dye/phage	IVIS readouts: total radiant efficiency	Normalized radiant efficiency*	# of phage injected	# dye/phage	IVIS readouts: total radiant efficiency	Normalized radiant efficiency*	
HPYSPLR	CP	Liver	898.12	4.0E+11	144.97	8.81E+09	1.69E-04	4.0E+11	372.35	3.82E+10	2.86E-04	0.59
		Pancreas	391.21	4.0E+11	144.97	7.09E+09	3.13E-04	4.0E+11	372.35	2.84E+09	4.87E-05	6.42
		Spleen	67.22	4.0E+11	144.97	3.75E+09	9.61E-04	4.0E+11	372.35	3.10E+09	3.10E-04	3.10
	Healthy	Liver	394.32	4.0E+11	140.20	1.48E+10	6.71E-04	4.0E+11	406.94	5.42E+10	8.44E-04	0.80
		Pancreas	52.36	4.0E+11	140.20	2.77E+09	9.44E-04	4.0E+11	406.94	1.94E+09	2.27E-04	4.16
		Spleen	103.91	4.0E+11	140.20	3.92E+09	6.73E-04	4.0E+11	406.94	4.18E+09	2.47E-04	2.73
KTYVPTT	CP	Liver	854.8	4.0E+11	167.47	1.11E+10	1.93E-04	4.0E+11	372.35	4.02E+10	3.16E-04	0.61
		Pancreas	218.97	4.0E+11	167.47	8.11E+09	5.53E-04	4.0E+11	372.35	1.51E+09	4.64E-05	11.90
		Spleen	85.2	4.0E+11	167.47	3.58E+09	6.28E-04	4.0E+11	372.35	2.61E+09	2.06E-04	3.05
	Healthy	Liver	1067.16	4.0E+11	167.47	1.18E+10	1.65E-04	4.0E+11	381.14	5.10E+10	3.13E-04	0.53
		Pancreas	410.1	4.0E+11	167.47	3.65E+09	1.33E-04	4.0E+11	381.14	9.51E+08	1.52E-05	8.74
		Spleen	98.27	4.0E+11	167.47	7.17E+09	1.09E-03	4.0E+11	381.14	4.76E+09	3.18E-04	3.43
MDLSLKP	CP	Liver	780.82	4.0E+11	146.93	8.22E+09	1.79E-04	4.0E+11	372.35	2.91E+10	2.50E-04	0.72
		Pancreas	243.54	4.0E+11	146.93	5.85E+09	4.09E-04	4.0E+11	372.35	1.37E+09	3.77E-05	10.85
		Spleen	80.31	4.0E+11	146.93	5.25E+09	1.11E-03	4.0E+11	372.35	4.92E+09	4.11E-04	2.70
	Healthy	Liver	1012.42	4.0E+11	146.93	8.59E+09	1.44E-04	4.0E+11	372.35	4.16E+10	2.76E-04	0.52
		Pancreas	264.06	4.0E+11	146.93	4.36E+09	2.81E-04	4.0E+11	372.35	1.91E+09	4.85E-05	5.79
		Spleen	91.74	4.0E+11	146.93	3.35E+09	6.22E-04	4.0E+11	372.35	3.64E+09	2.66E-04	2.34
SLPLGPM	CP	Liver	1006.12	4.0E+11	257.35	1.81E+10	1.75E-04	4.0E+11	372.35	4.12E+10	2.75E-04	0.64
		Pancreas	322.24	4.0E+11	257.35	7.93E+09	2.39E-04	4.0E+11	372.35	1.79E+09	3.72E-05	6.42
		Spleen	90.42	4.0E+11	257.35	9.12E+09	9.79E-04	4.0E+11	372.35	3.78E+09	2.81E-04	3.49
	Healthy	Liver	980.82	4.0E+11	257.35	2.24E+10	2.21E-04	4.0E+11	381.14	4.79E+10	3.20E-04	0.69
		Pancreas	343.27	4.0E+11	257.35	3.83E+09	1.08E-04	4.0E+11	381.14	1.13E+09	2.17E-05	5.00
		Spleen	95.61	4.0E+11	257.35	7.60E+09	7.72E-04	4.0E+11	381.14	3.92E+09	2.69E-04	2.87
HSGLNKQ	CP	Liver	240.02	4.0E+11	141.41	8.85E+09	6.51E-04	4.0E+11	372.81	3.70E+10	1.03E-03	0.63
		Pancreas	40.94	4.0E+11	141.41	4.99E+09	2.15E-03	4.0E+11	372.81	2.17E+09	3.55E-04	6.07
		Spleen	802.42	4.0E+11	141.41	4.69E+09	1.03E-04	4.0E+11	372.81	3.62E+09	3.02E-05	3.42
	Healthy	Liver	842.48	4.0E+11	106.78	6.03E+09	1.68E-04	4.0E+11	372.35	4.18E+10	3.33E-04	0.50
		Pancreas	239.5	4.0E+11	106.78	4.25E+09	4.16E-04	4.0E+11	372.35	1.49E+09	4.19E-05	9.93
		Spleen	90.63	4.0E+11	106.78	3.45E+09	8.92E-04	4.0E+11	372.35	4.07E+09	3.01E-04	2.96
MNSIAIP	CP	Liver	257.09	4.0E+11	115.32	9.36E+09	7.89E-04	4.0E+11	372.81	4.96E+10	1.29E-03	0.61
		Pancreas	45.9	4.0E+11	115.32	6.63E+09	3.13E-03	4.0E+11	372.81	2.19E+09	3.19E-04	9.81
		Spleen	887.72	4.0E+11	115.32	2.27E+09	5.54E-05	4.0E+11	372.81	2.03E+09	1.53E-05	3.61
	Healthy	Liver	758.75	4.0E+11	151.45	8.22E+09	1.79E-04	4.0E+11	372.35	3.79E+10	3.35E-04	0.53
		Pancreas	309.56	4.0E+11	151.45	3.98E+09	2.12E-04	4.0E+11	372.35	1.94E+09	4.20E-05	5.04
		Spleen	77.89	4.0E+11	151.45	3.93E+09	8.34E-04	4.0E+11	372.35	2.22E+09	1.91E-04	4.36
SANITNL	CP	Liver	377.24	4.0E+11	136.80	1.31E+10	6.35E-04	4.0E+11	372.81	4.82E+10	8.57E-04	0.74
		Pancreas	35.65	4.0E+11	136.80	3.74E+09	1.92E-03	4.0E+11	372.81	2.54E+09	4.77E-04	4.02
		Spleen	867.87	4.0E+11	136.80	5.11E+09	1.08E-04	4.0E+11	372.81	3.03E+09	2.34E-05	4.60
	Healthy	Liver	829.3	4.0E+11	87.24	6.56E+09	2.27E-04	4.0E+11	372.35	4.86E+10	3.93E-04	0.58
		Pancreas	375.21	4.0E+11	87.24	3.27E+09	2.50E-04	4.0E+11	372.35	3.27E+09	5.85E-05	4.27
		Spleen	87.12	4.0E+11	87.24	2.61E+09	8.59E-04	4.0E+11	372.35	3.68E+09	2.83E-04	3.03
SLTNSSF	CP	Liver	961.08	2.5E+11	182.53	1.82E+10	4.43E-04	2.5E+11	381.14	3.01E+10	3.34E-04	1.33
		Pancreas	217.65	2.5E+11	182.53	1.35E+09	1.45E-04	2.5E+11	381.14	3.33E+08	1.63E-05	8.86
		Spleen	93.18	2.5E+11	182.53	1.11E+09	2.78E-04	2.5E+11	381.14	9.19E+08	1.05E-04	2.65
	Healthy	Liver	810.23	4.0E+11	447.23	9.27E+09	6.39E-05	4.0E+11	372.35	7.25E+09	6.01E-05	1.06
		Pancreas	314.3	4.0E+11	447.23	7.86E+09	1.40E-04	4.0E+11	372.35	4.04E+09	8.63E-05	1.62
		Spleen	108.22	4.0E+11	447.23	7.59E+09	3.92E-04	4.0E+11	372.35	2.35E+09	1.46E-04	2.69
SNSQDLH	CP	Liver	302.49	4.0E+11	167.62	1.31E+10	6.45E-04	4.0E+11	372.81	3.98E+10	8.82E-04	0.73
		Pancreas	28.81	4.0E+11	167.62	4.05E+09	2.10E-03	4.0E+11	372.81	1.45E+09	3.37E-04	6.22
		Spleen	962.65	4.0E+11	167.62	7.33E+09	1.13E-04	4.0E+11	372.81	4.98E+09	3.47E-05	3.27
	Healthy	Liver	820.63	4.0E+11	142.64	8.55E+09	1.82E-04	4.0E+11	372.35	4.35E+10	3.56E-04	0.51
		Pancreas	336.62	4.0E+11	142.64	1.43E+09	7.43E-05	4.0E+11	372.35	1.80E+09	3.59E-05	2.07
		Spleen	70.03	4.0E+11	142.64	2.80E+09	7.00E-04	4.0E+11	372.35	2.35E+09	2.25E-04	3.11

*Normalized radiant efficienty = total radiant efficiency/(# of phage injected × # of dye/phage × tissue weight in gram)

Table S2.1. Phage clone individual validation raw data and calculation (continued).

CP-to-healthy ratio = normalized radiant efficiency of CP / normalized radiant efficiency of healthy tissue

	CP-to-healthy Ratio		
Phage	Liver	Pancreas	Spleen
HPYSPLR	0.744	1.544	1.138
KTYVPTT	1.161	1.362	0.890
MDLSLKP	1.370	1.875	1.156
SLPLGPM	0.921	1.286	1.215
HSGLNKQ	1.254	0.611	1.157
MNSIAIP	1.144	1.945	0.829
SANITNL	1.287	0.943	1.518
SLTNSSF	1.248	5.469	0.985
SNSQDLH	1.428	3.009	0.165

Chapter 3. Development of chronic pancreatitis-specific liposomes for antifibrotic therapy

This chapter is adapted from:
"High-throughput analytic selection of novel targeting ligands for chronic pancreatitis and development of target-specific liposomes for antifibrotic therapy".

Jessica Hung[1], Rohni Awasthi[1], Alexander L. Klibanov[2,3,4,5], Kimberly A. Kelly[2*]

1. Department of Biomedical Engineering, School of Engineering, University of Virginia, Charlottesville, Virginia, 22908, United States of America.
2. Department of Biomedical Engineering, School of Medicine, University of Virginia, Charlottesville, Virginia, 22908, United States of America.
3. Division of Cardiovascular Medicine, University of Virginia, Charlottesville, Virginia, 22908, United States of America.
4. Robert M. Berne Cardiovascular Research Center, University of Virginia, Charlottesville, Virginia, 22908, United States of America.
5. Department of Radiology, University of Virginia, Charlottesville, Virginia, 22908, United States of America.

*Corresponding Author. Email: kak3v@virginia.edu

Keywords: phage display, next-generation sequencing, peptide ligands, targeted liposomes, drug delivery

At this point, the text in this chapter has been submitted for peer review.

3.1 Abstract

Purpose: Fibrosis is a characteristic feature of chronic pancreatitis, which initiates a cascade of events and results in organ dysfunction and ultimate failure as the disease progresses. Despite apigenin has shown antifibrotic and anti-inflammatory effects in chronic pancreatitis, its clinical use is limited by low aqueous solubility, high metabolic instability, and adverse effects. Thus, developing a targeted liposomal form of apigenin could provide antifibrotic therapy for chronic pancreatitis.

Methods: In the present study, we utilized immunofluorescent imaging to identify the cellular targets of pancreatitis-specific peptides in the caerulein-induced mouse model of chronic pancreatitis. The chronic pancreatitis targeting ligands were conjugated to pegylated DOPC liposomes to evaluate the pharmacokinetics and pharmacodynamics of targeted delivery of apigenin in CP mice.

Results: We have identified cellular selectivity of the five chronic pancreatitis-specific peptides to activated pancreatic stellate cells, acinar cells, macrophages, and extracellular matrix, respectively. As a proof of concept, we conjugated the collagen IIIa^{+} cell-targeted peptide to liposomes and demonstrated targeted delivery of an antifibrotic small molecule drug, apigenin. After 3 weeks of treatment, acini preservation and stromal-fibrosis-reduction were observed. There was a 37.2% and 33.1% respective reduction in collagen and fibronectin expression in mice receiving apigenin-encapsulated targeted liposomes compared to the free drug.

Conclusion: In summary, we have developed a liposome-based anti-fibrotic therapies for chronic pancreatitis. Targeted delivery of apigenin has shown to improve tissue remodeling in the inflamed pancreas.

3.2 Introduction

Fibrosis is a characteristic feature of chronic pancreatitis (CP), which is not only an outcome of recurrent pancreatic parenchymal cell necrosis but is also responsible for the post-injury reactions that induce a cascade of events and signifies molecular and cellular damage. Various cellular components and molecular crosstalk are involved in fibrogenesis, and each of the components contributes to the clinical outcome of pancreatic remodeling. However, no FDA-approved drug is available to address the fundamental causes of inflammation and fibrogenesis to halt and reverse the damage of pancreatitis. In fact, current therapeutic strategies for CP are limited to palliative care and pain alleviation, and these approaches fail at the advanced stage when invasive surgical procedures are the only available options. Thus, addressing fibrotic conditions has become one of the main focuses to improve pancreatitis outcomes. Apigenin, a small molecule natural compound, has been shown preclinically to have antifibrotic, anti-inflammatory, antioxidant, and proapoptotic properties in CP and various cancers in vitro and in vivo [1–3]. Despite these promising features, apigenin suffers from low aqueous solubility, metabolic instability, and off-target effects [4]; and thus, no approved clinical applications of apigenin are available.

Liposome-based drug delivery has been clinically proven in the cancer setting to successfully encapsulate small molecule drugs for enhanced bioavailability, prolonged drug circulation half-life, and improved patient outcomes [5]. Surface modifications with targeting ligands such as antibodies, antibody fragments, and peptides enable specific binding at the diseased sites while minimizing undesired side-effects induced by off-targeting. In the tissue remodeling process of CP, various cellular and molecular components are involved and contribute to the progression, which make them potential targets. There are, however, no molecular targeting ligands or non-serum-based biomarkers available, limiting the development of imaging agents and therapeutics for pancreatitis. To fill that void, we used phage display and our innovative and computational guided target selection approach, PHASTpep [6], to identify peptides specific for key cellular components involved in fibrogenesis. Through in vivo imaging and colocalization analysis, we have demonstrated cell selectivity of five 7-mer peptides for acinar cells, activated pancreatic stellate cells (aPSCs), extracellular matrix (ECM), and

macrophages present in the CP microenvironment. As a proof of concept, we developed an apigenin-encapsulated liposomal formulation with surface modified with the ECM selective peptide, MDLSLKP, and demonstrated ligand-mediated drug delivery to the inflamed pancreas. After three weeks of treatment, we demonstrated a 37.2% and 33.1% reduction in collagen deposition and fibronectin expression, respectively, in the liposomal preparation compared to the free drug form and a 55.1% and 54.7% reduction in collagen and fibronectin expression, respectively, compared to no drug. The enhanced remodeling outcomes of the MDLSKLP-conjugated compared to the no-ligand liposomes and free drug indicates that for chronic pancreatitis cell type-selective targeting improved antifibrotic efficacy of a small molecule drug, which had undesirable properties. In this chapter, we identified the cellular targets of CP-specific ligands and demonstrated the application of these targeting peptides in drug delivery. The results of this work provide tools to mediate the development of target-specific interventions for CP.

3.3 Methods

3.3.1 Lipids for liposome preparation

1,2-Dioleoyl-sn-glycerol-3-phosphocholine (DOPC), and 1,2-distearoyl-sn-glycero-3-phosphoethanolamine-N-[methoxy(polyethylene glycol)-2000] (DSPE-PEG_{2000}) were purchased from Avanti Polar Lipids, Alabaster, AL; DSPE-PEG_{3400}-maleimide was purchased from Laysan Bio Inc., Arab, AL; 1,1'-dioctadecyl-3,3,3',3'- tetramethylindodicarbocyanine, 4-chlorobenzenesulfonate salt (DiD) was purchased from Biotium Inc., Hayward, CA; cholesterol was purchased from Millipore Sigma, Burlington, MA. Peptides were synthesized by the Tufts University Peptide Synthesis Core Facility using standard FMOC chemistry and Rink-Amide resin (Tufts University, Boston, MA). Caerulein was purchased from Bachem, Torrance, CA. Apigenin was purchased from Sigma, St. Louis, MO.

3.3.2 Fluorophores for ex vivo imaging and antibodies for western blot and immunohistochemistry

Fluorophore VivoTag 680 (VT680) was purchased from PerkinElmer, Waltham, MA, to guide tracking of phage clones by ex vivo imaging systems. Antibodies used for western blots are

rabbit anti-mouse SOD1 at 1:1000 dilution (Cell signaling, Danvers, MA), rabbit anti-mouse HSP70 at 1:1000 dilution (Cell Signaling, Danvers, MA), and mouse anti-mouse β-actin at 1:1000 (Cell Signaling, Danvers, MA). The antibody used for immunohistochemistry is anti-fibronectin at 1:50 dilution (Abcam, Cambridge, MA).

3.3.3 Caerulein-induced pancreatitis in mice

C57BL/6 J mice (6-12 week-old, female) were used for the in vivo phage screening. For chronic pancreatitis, caerulein (Bachem, Torrance, CA) was dissolved in sterile saline and administrated to mice twice a day, 8 hours apart for 14 consecutive days, at a concentration of 250 μg/kg body weight via intraperitoneal injection [7], as shown in Figure S2.1A. During the 14-day course, intraperitoneal injections of 100 μg/kg buprenorphine were given every 3 days to minimize the induced pain. For healthy controls, c57BL/6 J mice were injected intraperitoneally with an equal volume of sterile saline following the same schedule as in the chronic pancreatitis models. All animal experiments were approved by the Animal Care and Use Committee at the University of Virginia and conformed to the NIH "Guide for the Care and Use of Laboratory Animals in Research." The inflammatory status of the pancreas was confirmed at the end of caerulein treatments via immunohistochemistry using hematoxylin-eosin (H&E) and Picrosirius red (Polysciences, Inc., Warrington, PA) staining (Figure S2.1B).

3.3.4 Immunofluorescence (IF)

Post ex vivo imaging, mouse pancreata were submerged in Neg-50 Frozen Section Medium (Thermo Scientific, Waltham, MA) and snap-freezing over liquid nitrogen vapor. The embedded tissues were cut into 5 μm sections using a cryostat (Leica Microsystems Inc., Buffalo Grove, IL) for subsequent imaging with ZEISS LSM-880 Confocal Laser Scanning Microscope (Carl Zeiss Meditec, Inc., Jena, Germany) at the Advanced Microscopy Facility at the University of Virginia. Cell types of interest in the pancreatitis microenvironment were identified by immunohistochemistry using the following antibodies: rat anti-mouse CD31 at 1:200 dilution (endothelial markers) (BD Biosciences, San Jose, CA), rat anti-mouse CD206 at 1:1000 dilution (M2 macrophage markers) (Bio-Rad, Hercules, CA), rabbit anti-mouse cytokeratin 7 at 1:3000

dilution (CK-7, epithelial markers) (Abcam, Cambridge, MA), rabbit anti-mouse collagen IIIa at 1:200 dilution (ECM markers) (Abcam, Cambridge, MA), goat anti-mouse carboxypeptidase A1 at 1:200 dilution (CPA1, acini markers) (R&D Systems, Inc., Minneapolis, MN), rat anti-mouse F4/80 at 1:500 (macrophage markers) (Bio-Rad, Hercules, CA), and FITC-conjugated, mouse anti-mouse α-SMA at 1:200 dilution (Sigma, St. Louis, MO). Alexa Fluor 488 (Abcam, Cambridge, MA) antibodies from appropriate species, including donkey anti-goat, donkey anti-rat, donkey anti-rabbit at 1:500 dilution, were used as secondary antibodies to locate the primary antibodies. IF-stained pancreatic sections were mounted with ProLong Gold Antifade Mountant with DAPI (Thermo Fisher Scientific Inc, Waltham, MA).

3.3.5 Preparation and characterization of liposomes

Peptide 7-mers identified in the phage screen were chemically synthesized to include a C terminal addition of the amino acid linker, GGSK(FAM). Liposome preparation was carried out as previously described with minor modifications [8]. In brief, 4mg of peptides were first conjugated to 9.5mg of DSPE-PEG_{3400}-maleimide in 1mL of 0.5mM EDTA/PBS under argon to prepare the aqueous micellar solution. The micelle mixture was left 1h at room temperature, followed by overnight incubation at 4℃. Overnight dialysis was performed in PBS and then in MilliQ H_2O twice to remove free peptides and salts from the conjugated micelles. The purified DSPE-PEG_{3400}-peptide was then lyophilized and ready for use in liposome preparations. Liposomes were prepared by hydration of lipid film composed of the following reagents: DOPC (9.5mg), cholesterol (4.5mg), DSPE-PEG_{2000} (4.5mg), DSPE-PEG_{3400}-peptide (1mg), and DiD (0.5mg). DiD was incorporated into the lipid bilayer as a non-exchangeable near-infrared lipid dye, allowing in vivo detection of liposomes by IVIS (PerkinElmer, Waltham, MA). The lipid contents were mixed by sonication in 1 mL of chloroform, 1 mL of saline, and 3 mL of ether followed by placing on a rotary evaporator overnight to remove residual organic solvents. The lipid mixtures were then size-extruded 21 times through a syringe extruder with a 0.2 µm Nuclepore filter (Thermo Fisher Scientific, Inc., Waltham, MA). The size-extruded liposomes were centrifuged on A-100/18 Fixed-Angle Rotor (Beckman Coulter, Brea, CA) by Airfuge Air-Driven Ultracentrifuge (Beckman Coulter, Brea, CA) at 20 psig for 1h to separate micelles and unattached lipids from liposomes. The

resulting liposomal pellets were resuspended in saline and characterized by Nanosight NS300 (Malvern Instruments Ltd., Worcestershire, UK) to determine particle size and concentration (Figure 3.2 and S3.1). The absorbance of FAM at 495nm was used to determine the number of peptides incorporated in each liposome formulation.

3.3.6 Specificity and selectivity of peptide-conjugated liposomes

Peptide-conjugated liposomes (150 µL containing5×10^{11} particles) were injected via tail vein in CP mice (N=3) to determine the pharmacokinetic properties using IVIS. No peptide liposomes were used as negative controls to account for background bindings of liposomes. Mice hair were shaved and removed by depilatory creams prior to in vivo imaging on IVIS at 0, 6, 24, 48 and 72h post injections. 4, 24, 48, and 72h post injections, animals were perfused with saline, and pancreata were harvested for ex vivo imaging on IVIS using the Ex/Em 640/680 nm filter sets to detect DiD accumulation in the pancreas. The cellular targets of targeting liposomes were determined by IF using antibodies against the acinar cell marker (CPA1), aPSC marker (αSMA), ECM marker (collagen IIIa), epithelial marker (CK7), endothelial marker (CD31), and macrophage marker (F4/80). Co-localization analysis was done on the JACoP plugin of the ImageJ software (National Institute of Health, Bethesda, MD). Mander's co-localization coefficient (MCC), which represents the percentage of liposomes overlapping with cell markers, was used as an indicator to quantitate the extent of co-localization of liposomes with each cell type [9]. The ImageJ macro code and R code to batch-process IF images for colocalization analysis are attached in Appendix.

3.3.7 Apigenin drug loading and release kinetics

The lipid mixture, containing DOPC (9.5mg), cholesterol (4.5mg), DSPE-PEG_{2000} (4.5mg), DSPE-PEG_{3400}-peptide (1mg), and 2mg apigenin were pre-dissolved in 100uL ethanol, respectively. The drug and lipid mixture were mixed and added to 1mL PBS at 55℃, 1h. Liposomes were prepared by passing through a 0.2 µm Nucleopore filter using a syringe extruder. The free drug was removed by Zeba Spin Desalting Column, 40K MWCO (Thermo Scientific, Waltham, MA), which was pre-washed three times with saline. The resulting liposomes were characterized by Nanosight NS300. The drug loading per liposome was determined by Ultrospec 3000 UV/visible

spectrophotometer (Pharmacia Biotech, Sweden). The extinction coefficient of apigenin in saline is 664.02 ($M^{-1}cm^{-1}$) at 337nm, which was determined using Beer's law on serial-diluted samples. To determine the degree of apigenin maintained encapsulated in the purified liposomes at storage condition (PBS, 4℃), a release kinetic study was performed for 14 days. The purified liposomes were spun down in Pierce Protein Concentrators PES, 10K MWCO (Thermo Scientific, Waltham, MA) on day 0, 9, and 14 at storage conditions. The free drug concentration in the filtrate was determined by UV spectrometer to calculate the amount of free apigenin released from the purified liposomes. In vitro release kinetics was determined by placing drug-loaded liposomes in the cartridge of Slide-A-Lyzer Mini Dialysis devices, 10K MWCO (Thermo Fisher Scientific Inc, Waltham, MA), with the conical tube filled with 50% FBS/saline at 37℃. The FBS buffer was used as a blank to set up UV spectrometer readouts. Free drug released into FBS buffer was collected at day 0, 1, 3, and 4 post incubation and determined by UV spectrometer.

3.3.8 Pharmacodynamic measurement and evaluation of therapeutic efficacy of targeted delivery of apigenin

6 weeks old C57bl/6j mice were given intraperitoneal injections of caerulein (125 μg/kg, twice daily, 5 weeks). Following 2 weeks of caerulein treatment, animals were randomly divided into 4 groups, N = 5 per group: 1) vehicle — intravenous injections of MDLSLKP-conjugated liposomes (ECM Lip), twice-weekly 2) free drug – oral gavage of apigenin, 2mg/kg, 6 days per week [3], 3) Api-NP Lip — intravenous injections of apigenin encapsulated no peptide liposomes, 6mg/kg, twice per week, and 4) Api-ECM Lip — intravenous injections of apigenin encapsulated, MDLSLKP-conjugated liposomes, 6mg/kg, twice per week. Apigenin treatments lasted for 3 weeks for the remaining 3 weeks of caerulein induction. At the end of week 5, mice were euthanatized and cardiac punched for serum isolation. Pancreata were perfused, harvested and paraffin-embedded for immunohistochemistry staining. Livers were perfused, harvested, and partially paraffin-embedded for histology staining. The rest of the liver tissues were homogenized in the lysis buffer (200mM HEPES, pH7.5, 10mM KCl, 1.5mM $MgCl_2$, 1mM EDTA, 1mM EGTA, 2mM PMSF, 1mM DTT, and 1x Protease Inhibitor Cocktail (Thermo Fisher Scientific Inc, Waltham, MA)) [10]. Pancreata sectioned at 5 μm were stained with H&E, Picrosirius red, and fibronectin (1:50,

Abcam, Cambridge, MA). Visualization of fibronectin was done with DAB (Acros Organics, Fair Lawn, NJ) with counter staining using Hematoxylin 1 (Richard Allen Scientific, San Diego, CA). The quantification of Picrosirius red was determined by Image J, using threshold applied on the red composites of the RGB images. In the analysis, a total of 60 images per group (12 images per animal) were used for Picrosirius red quantification. Fibronectin expression was quantified using the positive pixel count function on QuPath [11]. Number of acini atrophy was determined by counting of atrophy center in a 256 μm x 256 μm field of view in pancreas H&E images. 5 images/animal, 3 animals/group were analyzed. Hepatoxicity induced by the treatments was evaluated by western blot of the liver lysates probing against SOD1 (Rabbit anti mouse 1:1000, Cell Signaling, Danvers, MA) and HSP70 (Rabbit anti mouse 1:1000, Cell Signaling, Danvers, MA). Serum alanine aminotransferase (ALT) and blood urea nitrogen (BUN) was determined on VetTest 8008 Chemistry Analyzer (IDEXX, Westbrook, ME).

3.3.9 Statistical analysis

Statistical analysis of the data was performed by student t-test, one-way analysis of variance (ANOVA) and Tukey-Kramer test. All data presented are expressed as mean$\pm$ standard error of at least three independent measurements. For all comparisons, p-value < 0.05 was considered significant.

3.4 Results

3.4.1 Identifying cellular targets of the CP-specific peptides

To identify the cell types that the CP targeting clones were binding, we performed immunofluorescent analysis on common cellular components in the CP microenvironment in the inflamed pancreas sections following in vivo validation of individual clones (Figure 3.1A). Mander's correlation coefficient (MCC) analysis was performed to determine colocalization of the targeting phage to the cell markers. Among each clone, we compared the MCC value of each cell marker to the rest of the markers using the Tukey-Kramer test (Table S3.1). Five clones were identified to demonstrate statistically significant colocalization to one single cell type; thus, an indication for cellular selectivity. Through this analysis, we showed KTYVPTT was selective for αSMA$^+$ cells (MCC = 0.521 $\pm$ 0.067), MDLSLKP for collagen IIIa$^+$ cells (MCC = 0.828 $\pm$ 0.089), MNSIAIP for CPA-1$^+$ cells (MCC = 0.633 $\pm$ 0.179), and SLTNSSF and SNSQDLH for F4/80$^+$ cells (MCC = 0.804 $\pm$ 0.090 and 0.800 $\pm$ 0.197, respectively) (Figure 3.1B). Phage clones and the associated cellular components in the inflamed pancreas are summarized in Figure 3.1C.

3.4.2 Peptide-conjugated liposomes altered nanoparticle pharmacokinetics and showed cellular selectivity in the inflamed pancreas.

Peptide MDLSKLP and MNSIAIP were conjugated to pegylated liposomes for their targeting cellular components, collagen IIIa$^+$ and CPA-1$^+$ cells, respectively present abundantly in the CP microenvironment. Despite demonstrating the highest in vivo ratio for specificity between the inflamed and healthy pancreas, we did not select the macrophage targeting peptides for this proof-of-concept drug delivery system because macrophages present in a wide spectrum of activated phenotypes in inflammatory and fibrotic diseases and are subjected to change in response to microenvironmental stimuli [12–14]. Better understanding the roles of macrophages in CP and further characterizations on the targeting specificity of SLTNSSF and SNSQDLH and subtypes of macrophage targeted will be needed. Peptide-conjugated liposomes were prepared by the reverse phase evaporation method with an average size of 90-110 nm in diameters, and the number of peptides displayed on the surface ranged from 400-450 per liposome (Figure 3.2A).

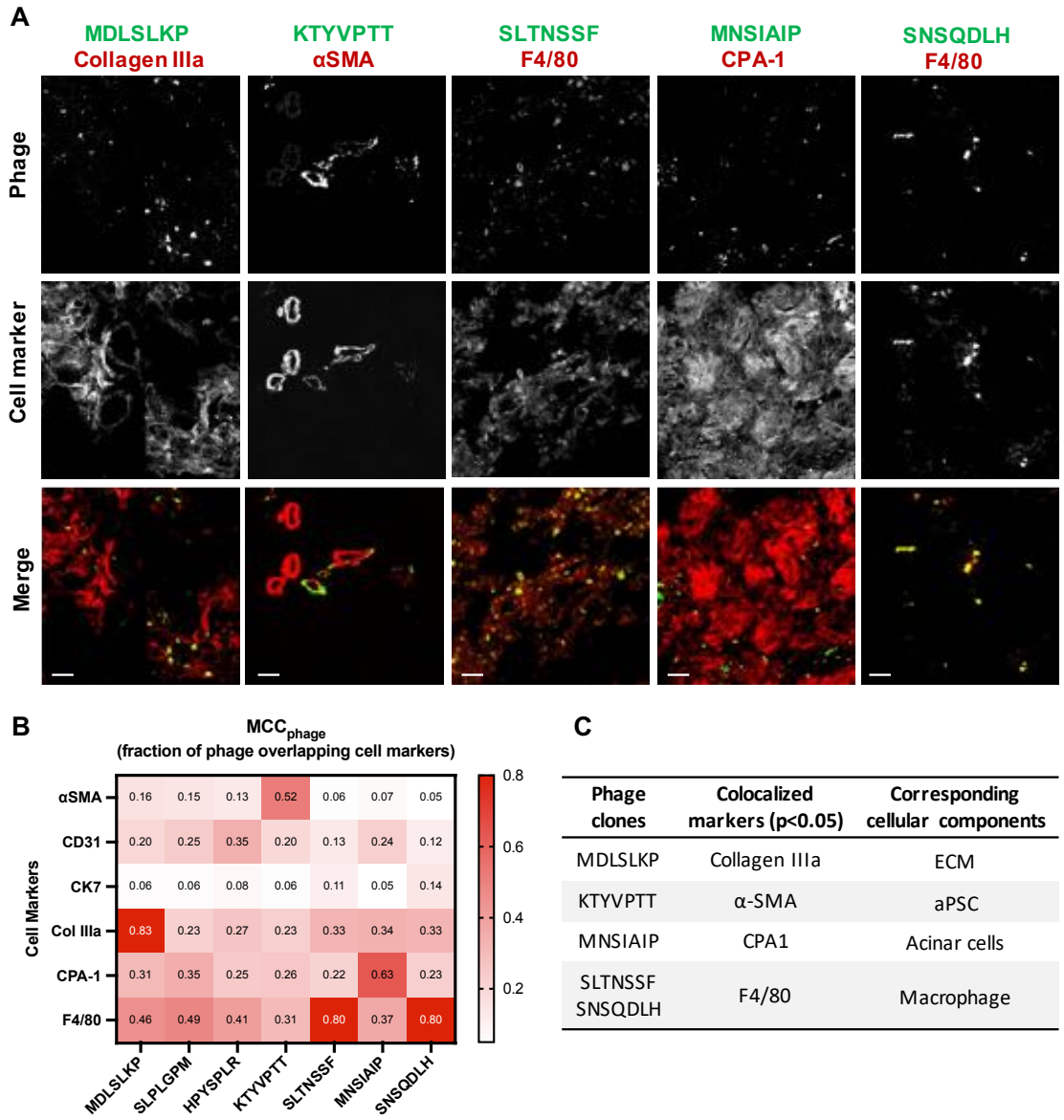

Phage clones	Colocalized markers (p<0.05)	Corresponding cellular components
MDLSLKP	Collagen IIIa	ECM
KTYVPTT	α-SMA	aPSC
MNSIAIP	CPA1	Acinar cells
SLTNSSF SNSQDLH	F4/80	Macrophage

Figure 3.1. CP-homing phage clones show selectivity for cellular components in the CP pancreas. (A) Immunofluorescence images of VT680-labeled phage colocalized with cell markers in the inflamed pancreas. Six cell markers were stained to represent six common cellular components in CP: αSMA (activated PSC), CD31 (endothelium), CK7 (epithelium), Collagen IIIa (ECM), CPA-1 (acinar cells), and F4/80 (macrophages). Colors in the merged images represent phage (green) and cell markers (red). Scale bar: 20 µm. (B) Heatmap of mean Manders' correlation coefficient (MCC) representing the fraction of phage overlapping with the cell markers. Manders' colocalization analysis was performed using the ImageJ plug-in JACoP. N = 10-12 images per marker, per clone. Col IIIa: collagen IIIa. (C) A table summarizing phage clones shown statistically significant selectivity for a single cellular component in CP. One-way ANOVA and Tukey-Kramer tests were used to compare MCC of all cell markers for each clone. The result was considered significant if the p-value ≤ 0.05.

All peptides used in the study have a net charge of +1 at pH 7.0. A non-exchangeable Lipid dye, DiD, was incorporated into the lipid formula at an average of 350-450 dye per liposome to allow particle tracking by non-invasive imaging modalities (Figure 3.2A). Liposomes without surface modifications (No-peptide liposomes, NP) were used as negative controls in the pharmacokinetics studies as liposomes are readily taken up by the abundant phagocytic cells present in CP. $5x10^{11}$ liposomes were injected into CP mice via tail vein, and the animals were imaged at 0, 6, 24, 48, and 72h post injection using IVIS. Starting at 6h and lasting until the 72h timepoint, fluorescent accumulation observed in the area of the left abdomen was consistent with the location of the pancreas in the MDLSLKP liposome-injected mice (Figure 3.2B). At 48h post injection, a 1.3-fold increase of MDLSLKP liposomal accumulation was detected in the inflamed pancreas compared to the NP liposomes (Figure 3.2C & D). Liposome accumulations were also observed in the clearance organs (liver, spleen, and kidney) as previously reported [15–17]. A significant reduction in liver and kidney accumulation of the MDLSLKP liposomes was observed in the biodistribution study, suggesting the addition of targeting ligands altered the particle distribution away from the clearance organs to the inflamed pancreas. We, however, did not observe significant difference in pancreas and liver accumulation of the MNSIAIP liposome compared to the NP liposome.

The cellular selectivity of the targeting liposomes in the inflamed pancreas at 48h-post injection was systematically validated via colocalization analyses on IF-stained tissue sections stained for 6 cell markers (Figure 3.3A). As expected, a significant amount of NP liposomes were colocalized to macrophages (MCC = 0.534 ± 0.178) as liposomes are readily phagocytosed by macrophages, which are abundant in the inflamed pancreas [18]. The addition of peptide ligands shifted the cellular targets of the MDLSLKP liposome to collagen $IIIa^+$ cells (MCC = 0.493 ± 0.142), demonstrating the preservation of similar ECM selectivity as it was in the phage from (Figure 3.3B). The MNSIAIP liposome, however, did not show statistically significant selectivity towards CPA-1^+ cells, suggesting that this peptide lost its selectivity once conjugated to a liposome. The loss of cell selectivity may explain the result of the in vivo studies where increased pancreas accumulation was observed in the phage form but not in the liposomal form. Combining the

A

Liposome	No peptide	MDLSLKP	MNSIAIP
Size (nm)	103.3 ± 1.3	105.1 ± 3.1	110.5 ± 1.7
Concentration (particle/mL)	$1.30x10^{14}$	$8.18×10^{13}$	$1.47×10^{14}$
# peptide per liposome	-	436.52	405.05
# DiD per liposome	372.20	429.30	358.21
Zeta potential (mV)	-37.2	-29.9	-30.7

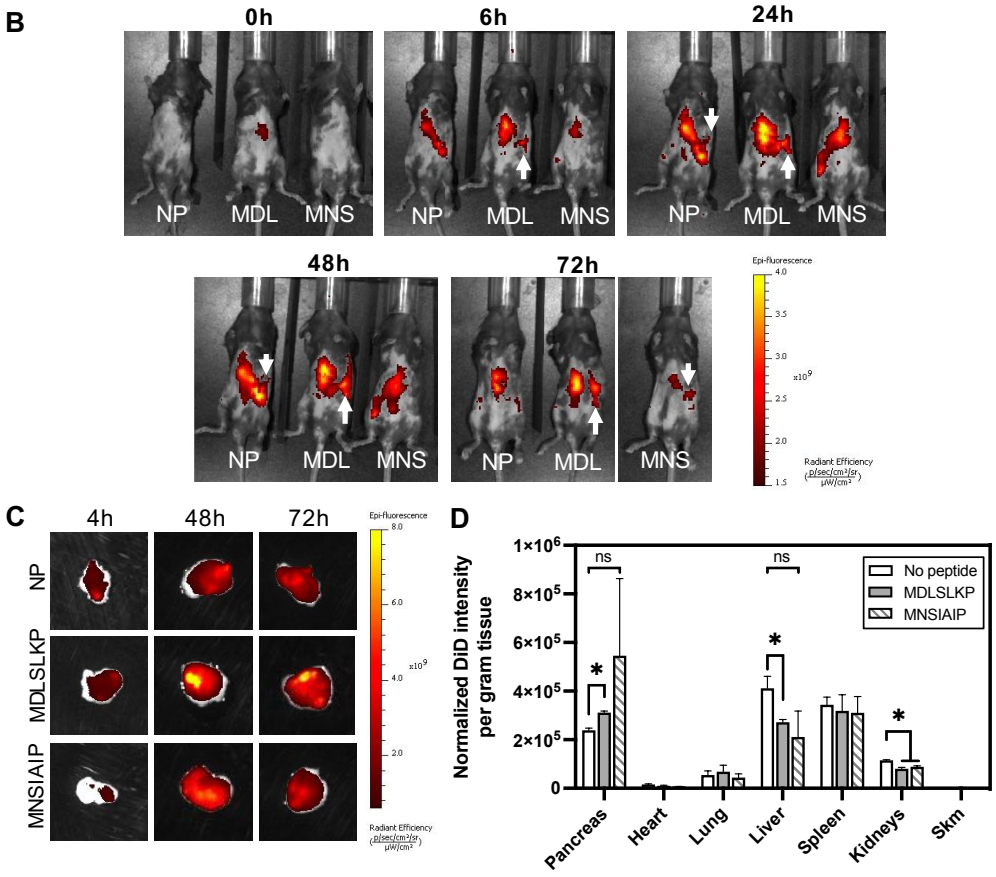

Figure 3.2. Pharmacokinetics of peptide-modified liposomes. (A) Table showing characteristic features of surface-modified liposomes with peptides identified to target collagen IIIa^{+} and acinar cells. (B) In vivo IVIS images of CP mice over 72h time course post-injection of peptide-modified liposomes. The white arrow indicates fluorescent signal detected at the pancreas region. (C) Ex vivo IVIS images of pancreas at 4, 48, and 72h post liposome injection. (D) Biodistribution of DiD-labeled liposomes in CP mice at 48h post injection. Fluorescent intensity is normalized to the number of particles injected, the number of DiD per liposome, and mass of the pancreas. N = 3. Student t-test was used to compare the targeted liposomes to the no peptide liposomes. *p < 0.05. Skm: Skeletal muscle.

pharmacokinetics and cell colocalization results, we concluded that MDLSLKP peptide improved liposome targeting of collagen IIIa^{+} cells by 1.5-3 fold as compared with other cell types, which result in increased pancreas accumulation. The targeting ligands identified could shift liposomes away from macrophage uptake and towards target cells as supported by the Tukey-Kramer test of MCCs of all cell types in the NP and MDLSLKP liposomes (Table S3.2).

3.4.3 Targeted delivery of apigenin enhances anti-fibrotic effects in CP mice.

Apigenin is a small molecule natural compound, that has been demonstrated preclinically to have antifibrotic and anti-inflammatory properties in CP [1, 3]. Apigenin, however, suffers from low aqueous solidity, metabolic instability, and off-target effects that there are no approved clinical applications of apigenin available [10, 19, 20]. Therefore, we used apigenin as a proof of concept and directly loaded it into the MDLSLKP-conjugated liposomes (ECM liposome). Free apigenin was removed from liposomes by size exclusion chromatography. The drug loading was determined using UV spectrometer and showed a 40-50% encapsulation rate in both NP and ECM liposomes. The final drug-to-lipid ratio was estimated at an average of 80-100 ug apigenin per mg of lipid, and each liposome contains 28000~34000 drug per particle (Figure 3.4C). Both apigenin-loaded NP and ECM liposomes had a diameter of 90-100 nm measured by NanoSight. We also determined the shelf-life of the drug- encapsulated liposomes and showed >95% of the encapsulated apigenin remained in liposomes in the storage condition (PBS, 4℃) over 14 days (Figure 3.4D). Hydrophobic molecules are usually encapsulated in the lipid layer of liposomes and may burst release out from the particles in vivo [21]. To test whether apigenin will burst release in our system, we performed an in vitro release study in 50% FBS/PBS at 37℃. We did not see burst release of apigenin in the first couple hours upon placing liposomes in 50% FBS. Instead, 14.02% of the encapsulated apigenin molecules were released by day 1 and 52.69% by day 4 (Figure 3.4E).

To test the anti-fibrotic efficacy of targeted liposomes, we evaluated pharmacodynamics of apigenin in the free drug form, encapsulated in non-targeted liposome and in ECM liposome (Figure 3.5A). ECM liposomes without drug loading were included in the study as a vehicle control.

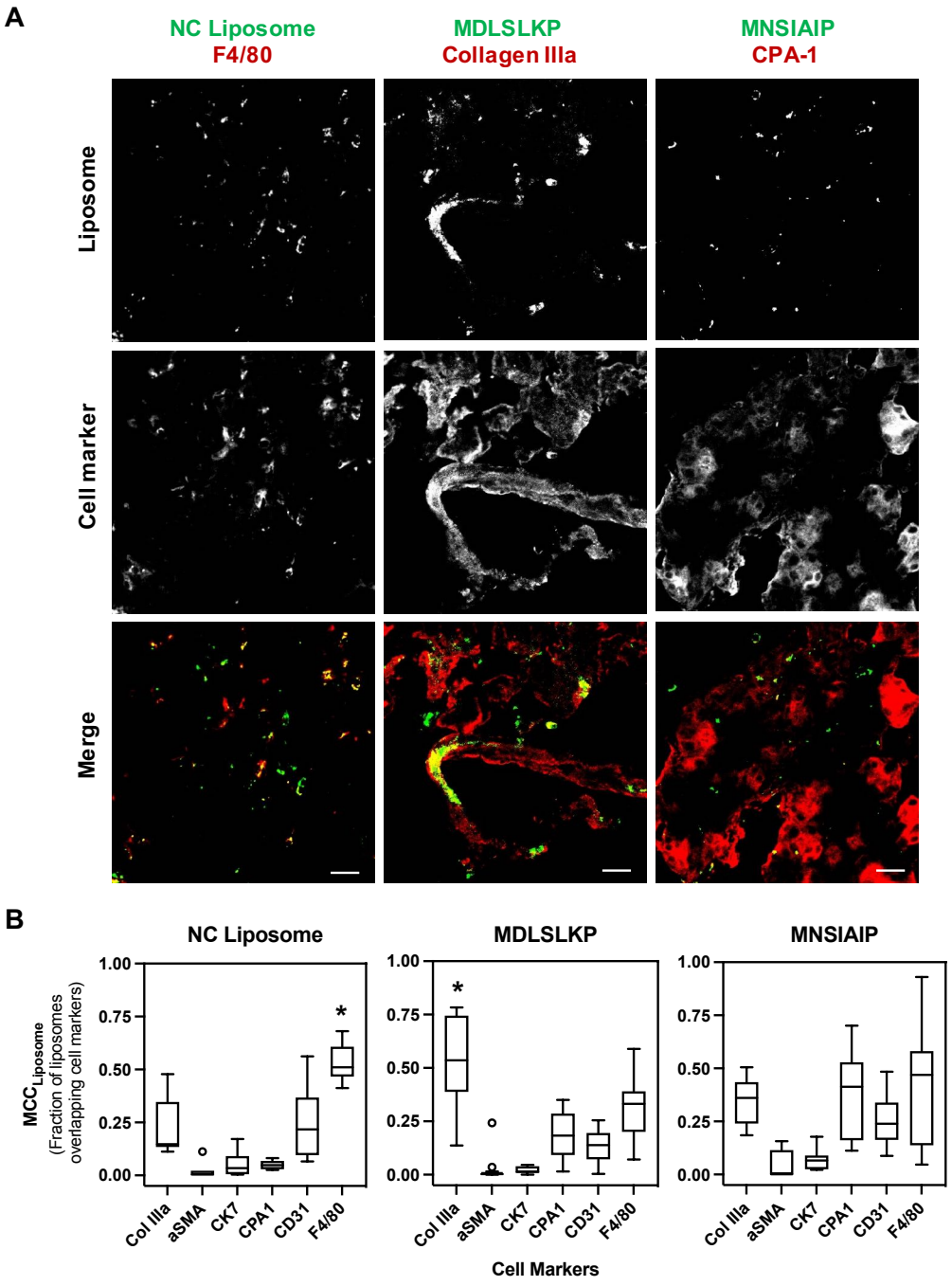

Figure 3.3. Immunofluorescence of peptide conjugated liposomes in CP pancreas. (A) NC liposomes were non-specifically taken up by macrophages presented in the inflamed pancreas. MDLSLKP liposomes colocalized with extracellular matrix (collagen IIIa^{+} cells). Color code: green for liposome (DiD), and red for cell markers. Scale bar: 20 μm. (B) Box-and whisker plot of MCC values of liposomes overlapping cell markers. Liposome selectivity for the corresponding cell types was analyzed using the ImageJ plug-in JACoP. N = 7~12 images per group. One-way ANOVA and Tukey-Kramer tests were used to compare MCC of all cell markers for each liposome. *$p < 0.05$. No statistically significant difference was observed in spatial localization of MNSIAIP liposomes with any stained cell types.

C57BL/6J mice were injected with caerulein 14 days before treatments started to establish inflammatory status in the pancreas. Apigenin, in the free drug or liposomal form, were given in the remaining 3-week course along with caerulein. As expected, increased acini atrophy and cellular heterogeneity in size and shape, in addition to increased interstitial space, fibrosis, and collagen deposition (34.83% area) were observed in the control group [3] (Figure 3.5B-D). Compared to free drug and NP liposomes, targeted delivery of apigenin resulted in enhanced preservation of acini units with less acinar atrophy observed in tissues, and the reduction of interstitial space between acinus (Figure 3.5B and E). Although NP liposomes have substantial macrophage uptake, the enhanced pharmacodynamic activity of apigenin loaded into ECM

A

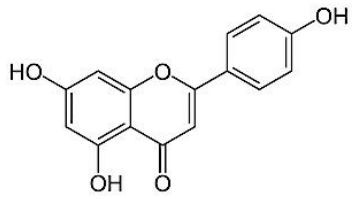

B

Properties	Apigenin, $C_{15}H_{10}O_5$
Molecular weight	270.24 g/mol
Water Solubility	0.183 g/mL
Charge (pH 7.4)	0
pKa	pKa_1 = 7.12; pKa_2 = 8.10
Log P	1.7

C

	No peptide liposomes	ECM liposomes
Size (nm)	93.1 ± 3.6	94.3 ± 1.4
Batch concentration (particle/mL)	1.09E+14	1.52E+14
Drug per liposome	33930	28501

D

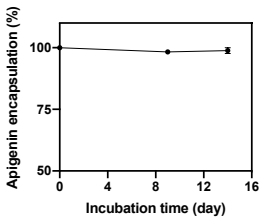

E

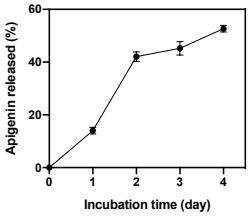

Figure 3.4. Apigenin loading in peptide-modified liposomes. (A) Chemical structure and (B) physiochemical properties of apigenin reported on PubChem. (C) A characteristic table shows the properties of apigenin-loaded liposomes. (D) The release profile of apigenin in PBS at 4C, pH7.4, from liposomes. N=3. (E) In vitro release study in 50% FBS at 37C. N =3.

targeted liposomes demonstrated the importance of cell-specific targeting to drug activity. Using Picrosirius red to stain for collagen, we found that collagen deposition was reduced from 24.90% area to 15.63% in the free apigenin versus targeted liposomal form, respectively (p-value < 0.0001, Figure 3.5D and G). Apigenin loaded in NP liposomes reduced collagen to 19.18% area of the inflamed tissue, suggesting that liposomal formulation of apigenin alone resulted in better therapeutic efficacy than free drug but was not as effective as targeted delivery to the ECM. Targeted liposomes resulted in 33.1% better reduction in fibronectin expression when compared to free drug alone and 41.0% reduction compared to NP liposomes (p-value < 0.05. Figure 3.5C and F). In addition to therapeutic efficacy, we also evaluated hepatotoxicity induced by apigenin [10] in free drug and liposomal form and showed a 1.2-fold increase of SOD1 expression in targeted liposomes, indicating reduction of oxidative stress in the liver (Figure S3.2C), matching the reduced liver accumulation in liposome biodistribution study. Liposome-based anti-fibrotic therapies have been evaluated in many pre-clinical studies [22–25]. Lacking a selective and specific targeting ligand, however, has limited the clinical implementation. The 7-mer peptides we identified from the inflamed pancreas can be applied to other cell type-selective therapeutic molecules to potentially improve tissue remodeling and reduce fibrosis and inflammation in CP.

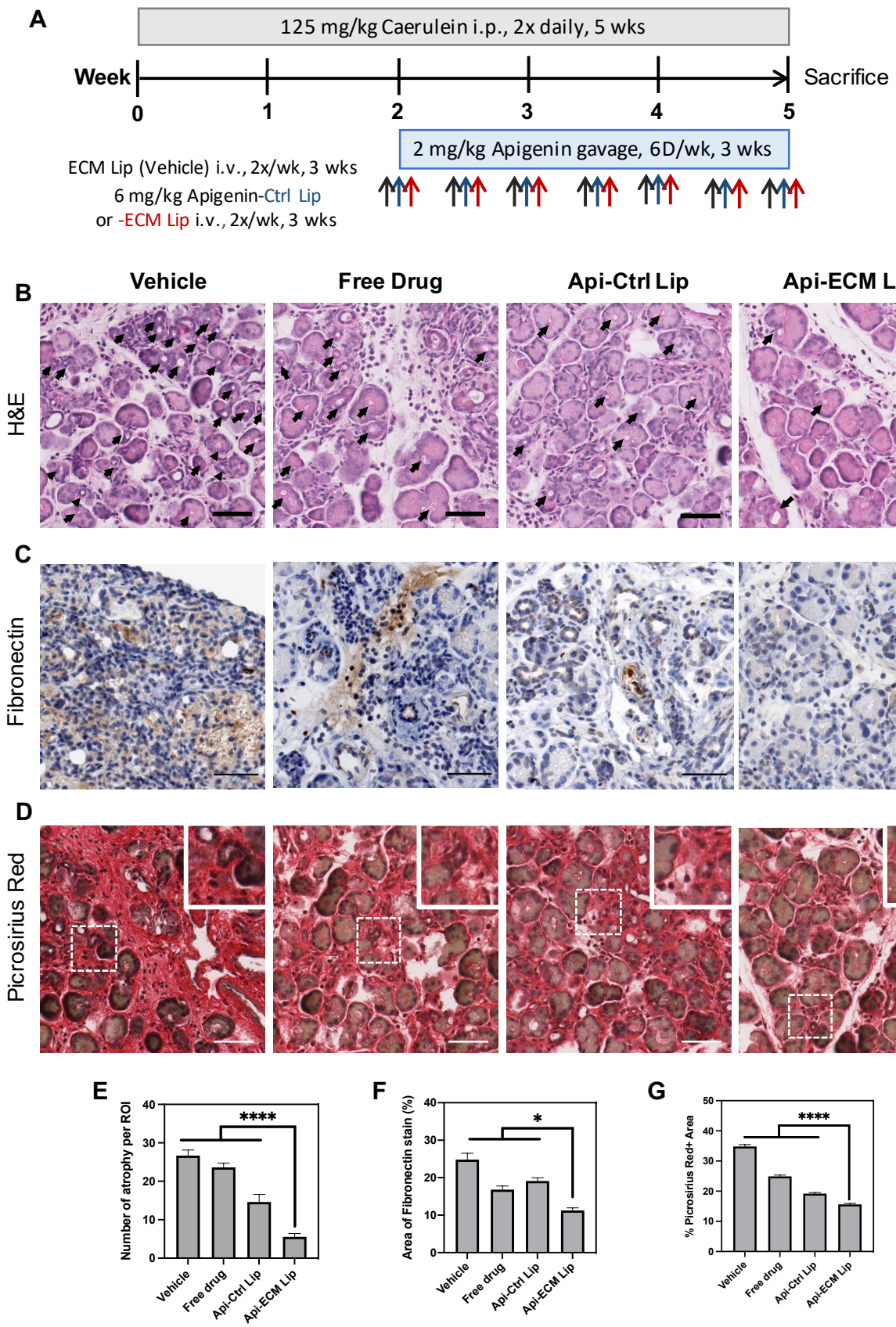
A
125 mg/kg Caerulein i.p., 2x daily, 5 wks
Week
0
1
2
3
4
5
Sacrifice
2 mg/kg Apigenin gavage, 6D/wk, 3 wks
ECM Lip (Vehicle) i.v., 2x/wk, 3 wks
6 mg/kg Apigenin-Ctrl Lip
or -ECM Lip i.v., 2x/wk, 3 wks
B
Vehicle
Free Drug
Api-Ctrl Lip
Api-ECM Lip
H&E
C
Fibronectin
D
Picrosirius Red
E
Number of atrophy per ROI
****
Vehicle
Free drug
Api-Ctrl Lip
Api-ECM Lip
F
Area of Fibronectin stain (%)
*
G
% Picrosirius Red+ Area
****

Figure 3.5. Targeted delivery of Apigenin reduces fibrosis. (A) Schematic of CP mouse model followed by 3-week treatments of either empty ECM liposome (vehicle), free apigenin (free drug), apigenin-encapsulated naked liposomes (Api-Naked Lip), or apigenin-encapsulated MDLSLKP liposomes (Api-ECM Lip) (N=5). (B) H&E staining of pancreas by the end of 3-week treatments. A reduced interstitial space and acinar atrophy (indicated by arrows) was observed in the pancreas treated by targeted liposomes compared to free drug and the control liposomes. Scale bar: 50 μm. (C) Pancreas immuno-stained for fibronectin demonstrated targeted delivery of apigenin significantly decreased fibronectin expression. Scale bar: 100 μm. (D) Picrosirius red staining of pancreas. Scale bar: 50 μm. (E) Number of acini atrophy found in a 256 μm x 256 μm image. N = 5 images/animal, 3 animals/group. (F) Quantification of fibronectin-positive area. N = 8 images/animal, 5 animals/group. (G) Quantification of Picrosirius red-positive area. N = 12 images/animal, 5 animals/group. In all images, ANOVA and Tukey test were used to compare Api-ECM Lip to the rest of the treatment groups. *p<0.05, ****p<0.0001.

3.5 Discussion

Chronic pancreatitis is a complex inflammatory pancreatic disease that remains incurable [26–29]. Current treatments for CP are limited to palliative care and pain alleviation, and these approaches fail at the advanced stage when invasive surgical procedures such as endoscopic interventions, bypass, and total pancreatectomy are the only available options [30]. The pancreatic community has recently reached a consensus that precision medicine can provide a more sophisticated approach for complex disorders like CP to assist the development of target specific interventions [29]. Despite omics-based technology being widely used to profile disease-specific biomarkers and therapeutic targets in many diseases [31, 32], transcriptomics reveals little about CP-specific pathways due to the universal genetic backgrounds shared between pancreatitis, pancreatic cancer, and the benign pancreas [33]. Looking only in epithelial cells, Sanh et al showed differential expression in 34 proteins in malignant and pancreatitis pancreas compared to the benign tissue, but were not able to distinguish pancreatitis from pancreatic cancer [34]. Considering the heterogeneity of cellular components involved in disease progression of CP, there is a definite need to provide an unbiased, comprehensive evaluation of pancreatitis-associated proteomes.

In chapter 2, we have identified seven 7-mer peptides specific to CP using a computational-guided in vivo phage display approach. To explore the potential of the CP targeting peptides in cell type-specific drug delivery, we conjugated the peptides to pegylated DOPC liposomes and characterized the pharmacokinetics. A hallmark of CP is the presence of large numbers of phagocytic cells, and indeed, NP liposomes were taken up by the macrophage cell population. The addition of targeting ligands, however, shifted the cellular targets of the MDLSLKP-conjugated liposomes away from macrophages and demonstrated selectivity to collagen IIIa^{+} cells, which is consistent with its phage clone. The MNSIAIP liposome, however, did not show statistically significant selectivity towards CPA-1^{+} cells, suggesting that this peptide lost its selectivity once conjugated to a liposome. A shift in organ accumulations from the clearance organs to the inflamed pancreas was also achieved when injecting liposomes displaying MDLSLKP peptide. The improvement in increasing the ratio of on-target to off-target effects could address the side-effects induced by antifibrotic drugs that act on canonical extracellular factors, including growth factors, cytokines, and MMPs. For example, TGF-β inhibitors are amongst the majority of approved or investigational anti-fibrosis drug families and have demonstrated efficacy in reducing cardiac, liver and kidney fibrosis [35]. However, galnisertib, a TGF-β R1 kinase inhibitor, caused cardiac toxicity, bone development abnormality and induced irregular inflammatory responses in skin and gut at long-term use, which ended with termination on Phase II clinical trial (NCT0113801) [36]. The ability to selectively target multiple different cell types in CP can open a new avenue for therapeutic strategies that address the crosstalk between ECM components and aPSCs, which initiates multiple cascades of events in fibrogenesis and inflammation in CP [1, 37]. Indeed, we demonstrated that targeting apigenin to the ECM demonstrated enhanced pharmacodynamic effects beyond that of targeting macrophages alone with NP liposomes underscoring the importance of targeting. Apigenin is a small molecule drug that has been shown to have antifibrotic, anti-inflammatory, and proapoptotic effects in cancer and chronic inflammatory diseases in vitro and in vivo [1–3, 38, 39]. The clinical use of apigenin, however, is limited by low aqueous solubility, high metabolic instability, and potential hepatotoxicity at acute use [10, 19, 20]. As a proof of concept, we encapsulated apigenin in liposomes and evaluated the antifibrotic effects through cellular component-specific delivery to the ECM in CP pancreas. After

3 consecutive weeks of treatments, mice receiving drug-encapsulated, ECM-targeted liposomes showed the best tissue remodeling effects, including acini unit preservation and stroma reduction, compared to free drug and non-targeted liposomes. In addition, targeted delivery reduced off-target effects [40] as mice receiving apigenin encapsulated in targeted liposomes showed reduced ALT and liver SOD1 expression and preserved liver histology compared to the non-targeted delivery (Figure S3.2A & C). The results of our work demonstrated that cell type-specific targeting of small molecule drugs can improve pharmacodynamics and alter the anatomical endpoint (fibrosis) in the inflamed pancreas.

3.6 Conclusion

Five 7-mer peptides that show specificity to aPSCs, acinar cells, macrophages, and ECM in CP, respectively, were identified and demonstrated the biomedical applications of targeted delivery of a small molecule drug to achieve tissue remodeling in the inflamed pancreas.

3.7 Acknowledgments

The authors would like to thank Y. Bao of the UVA Biomolecular Research Core Facility for NGS; M. Bevard of the UVA Cardiovascular Research Center histology core for paraffin embedding and IHC staining. The work was supported by NIH (R21 CA231196-01, R01 CA233716-01 A1) and NCI (P30 CA044579-26).

3.8 Author Contributions

Conceptualization (JH, ALK, KAK), data curation (JH, RA), formal analysis (JH), investigation (JH, RA, ALK, KAK), methodology (JH, RA, ALK, KAK), project administration (KAK), supervision (ALK, KAK), visualization (JH), writing – original draft (JH), and writing – review & editing (JH, RA, ALK, KAK).

3.9 Declaration of Interests

The authors declare that Dr. Kelly is the CEO and Founder of ZielBio, Inc. ZielBio played no role in funding this work. JH, RA, and ALK declare no conflicts of interest in this work.

3.10 Reference

[1] A. A. Mrazek, V. Bhatia, M. Falzon, H. Spratt, C. Chao, and M. R. Hellmich, "Apigenin Decreases Acinar Cell Damage in Pancreatitis," *Pancreas*, vol. 48, no. 5, p. 711, Jun. 2019, doi: 10.1097/MPA.0000000000001310.

[2] S. Shukla and S. Gupta, "Apigenin: A Promising Molecule for Cancer Prevention," *Pharm. Res.*, vol. 27, no. 6, pp. 962–978, Jun. 2010, doi: 10.1007/s11095-010-0089-7.

[3] A. A. Mrazek *et al.*, "Apigenin inhibits pancreatic stellate cell activity in pancreatitis," *J. Surg. Res.*, vol. 196, no. 1, pp. 8–16, Jun. 2015, doi: 10.1016/j.jss.2015.02.032.

[4] H. Chen *et al.*, "Design, synthesis, and characterization of novel apigenin analogues that suppress pancreatic stellate cell proliferation in vitro and associated pancreatic fibrosis in vivo," *Bioorg. Med. Chem.*, vol. 22, no. 13, pp. 3393–3404, Jul. 2014, doi: 10.1016/j.bmc.2014.04.043.

[5] C. Bornmann *et al.*, "A new liposomal formulation of Gemcitabine is active in an orthotopic mouse model of pancreatic cancer accessible to bioluminescence imaging," *Cancer Chemother. Pharmacol.*, vol. 61, no. 3, pp. 395–405, Mar. 2008, doi: 10.1007/s00280-007-0482-z.

[6] L. T. Brinton, D. K. Bauknight, S. S. K. Dasa, and K. A. Kelly, "PHASTpep: Analysis Software for Discovery of Cell-Selective Peptides via Phage Display and Next-Generation Sequencing," *PLOS ONE*, vol. 11, no. 5, p. e0155244, May 2016, doi: 10.1371/journal.pone.0155244.

[7] C. J. Halbrook *et al.*, "Mitogen-activated Protein Kinase Kinase Activity Maintains Acinar-to-Ductal Metaplasia and Is Required for Organ Regeneration in Pancreatitis," *Cell. Mol. Gastroenterol. Hepatol.*, vol. 3, no. 1, pp. 99–118, Jan. 2017, doi: 10.1016/j.jcmgh.2016.09.009.

[8] S. S. K. Dasa *et al.*, "Development of target-specific liposomes for delivering small molecule drugs after reperfused myocardial infarction," *J. Control. Release Off. J. Control. Release Soc.*, vol. 220, no. Pt A, pp. 556–567, Dec. 2015, doi: 10.1016/j.jconrel.2015.06.017.

[9] E. M. M. Manders, F. J. Verbeek, and J. A. Aten, "Measurement of co-localization of objects in dual-colour confocal images," *J. Microsc.*, vol. 169, no. 3, pp. 375–382, 1993, doi: https://doi.org/10.1111/j.1365-2818.1993.tb03313.x.

[10] P. Singh, S. K. Mishra, S. Noel, S. Sharma, and S. K. Rath, "Acute Exposure of Apigenin Induces Hepatotoxicity in Swiss Mice," *PLOS ONE*, vol. 7, no. 2, p. e31964, Feb. 2012, doi: 10.1371/journal.pone.0031964.

[11] P. Bankhead *et al.*, "QuPath: Open source software for digital pathology image analysis," *Sci. Rep.*, vol. 7, no. 1, p. 16878, 04 2017, doi: 10.1038/s41598-017-17204-5.

[12] T. A. Wynn and L. Barron, “Macrophages: Master Regulators of Inflammation and Fibrosis,” *Semin. Liver Dis.*, vol. 30, no. 3, pp. 245–257, Aug. 2010, doi: 10.1055/s-0030-1255354.

[13] R. D. Stout, C. Jiang, B. Matta, I. Tietzel, S. K. Watkins, and J. Suttles, “Macrophages sequentially change their functional phenotype in response to changes in microenvironmental influences,” *J. Immunol. Baltim. Md 1950*, vol. 175, no. 1, pp. 342–349, Jul. 2005, doi: 10.4049/jimmunol.175.1.342.

[14] N. Kawanishi, H. Yano, Y. Yokogawa, and K. Suzuki, “Exercise training inhibits inflammation in adipose tissue via both suppression of macrophage infiltration and acceleration of phenotypic switching from M1 to M2 macrophages in high-fat-diet-induced obese mice,” *Exerc. Immunol. Rev.*, vol. 16, pp. 105–118, 2010.

[15] L. D. Mayer, G. Dougherty, T. O. Harasym, and M. B. Bally, “The Role of Tumor-Associated Macrophages in the Delivery of Liposomal Doxorubicin to Solid Murine Fibrosarcoma Tumors,” *J. Pharmacol. Exp. Ther.*, vol. 280, no. 3, pp. 1406–1414, Mar. 1997.

[16] G. A. Koning, J. A. A. M. Kamps, and G. L. Scherphof, “Interference of macrophages with immunotargeting of liposomes,” *J. Liposome Res.*, vol. 12, no. 1–2, pp. 107–119, May 2002, doi: 10.1081/lpr-120004782.

[17] M. L. Immordino, F. Dosio, and L. Cattel, “Stealth liposomes: review of the basic science, rationale, and clinical applications, existing and potential,” *Int. J. Nanomedicine*, vol. 1, no. 3, pp. 297–315, 2006.

[18] A. Vonarbourg, C. Passirani, P. Saulnier, P. Simard, J. C. Leroux, and J. P. Benoit, “Evaluation of pegylated lipid nanocapsules versus complement system activation and macrophage uptake,” *J. Biomed. Mater. Res. A*, vol. 78A, no. 3, pp. 620–628, 2006, doi: https://doi.org/10.1002/jbm.a.30711.

[19] J. Zhang, D. Liu, Y. Huang, Y. Gao, and S. Qian, “Biopharmaceutics classification and intestinal absorption study of apigenin,” *Int. J. Pharm.*, vol. 436, no. 1–2, pp. 311–317, Oct. 2012, doi: 10.1016/j.ijpharm.2012.07.002.

[20] J. K. Srivastava and S. Gupta, “Extraction, Characterization, Stability and Biological Activity of Flavonoids Isolated from Chamomile Flowers,” *Mol. Cell. Pharmacol.*, vol. 1, no. 3, p. 138, Jan. 2009.

[21] J. Gubernator, “Active methods of drug loading into liposomes: recent strategies for stable drug entrapment and increased in vivo activity,” *Expert Opin. Drug Deliv.*, vol. 8, no. 5, pp. 565–580, May 2011, doi: 10.1517/17425247.2011.566552.

[22] S. A. Sung, S. K. Jo, W. Y. Cho, N. H. Won, and H. K. Kim, “Reduction of renal fibrosis as a result of liposome encapsulated clodronate induced macrophage depletion after unilateral ureteral obstruction in rats,” *Nephron Exp. Nephrol.*, vol. 105, no. 1, pp. e1-9, 2007, doi: 10.1159/000096859.

[23] A. Jose, P. K. Mandapalli, and V. V. K. Venuganti, “Liposomal hydrogel formulation for transdermal delivery of pirfenidone,” *J. Liposome Res.*, vol. 26, no. 2, pp. 139–147, 2016, doi: 10.3109/08982104.2015.1060611.

[24] F. Khaja, D. Jayawardena, A. Kuzmis, and H. Önyüksel, “Targeted Sterically Stabilized Phospholipid siRNA Nanomedicine for Hepatic and Renal Fibrosis,” *Nanomaterials*, vol. 6, no. 1, Jan. 2016, doi: 10.3390/nano6010008.

[25] Y. Zhang, D. Yue, L. Cheng, A. Huang, N. Tong, and P. Cheng, “Vitamin A-coupled liposomes carrying TLR4-silencing shRNA induce apoptosis of pancreatic stellate cells and resolution of pancreatic fibrosis,” *J. Mol. Med. Berl. Ger.*, vol. 96, no. 5, pp. 445–458, 2018, doi: 10.1007/s00109-018-1629-6.

[26] D. C. Whitcomb *et al.*, “Chronic pancreatitis: An international draft consensus proposal for a new mechanistic definition,” *Pancreatol. Off. J. Int. Assoc. Pancreatol. IAP Al*, vol. 16, no. 2, pp. 218–224, Apr. 2016, doi: 10.1016/j.pan.2016.02.001.

[27] D. C. Whitcomb, “Peering Into the ‘Black Box’ of the Complex Chronic Pancreatitis Syndrome,” *Pancreas*, vol. 45, no. 10, pp. 1361–1364, Nov. 2016, doi: 10.1097/MPA.0000000000000715.

[28] D. C. Whitcomb *et al.*, “International consensus statements on early chronic Pancreatitis. Recommendations from the working group for the international consensus guidelines for chronic pancreatitis in collaboration with The International Association of Pancreatology, American Pancreatic Association, Japan Pancreas Society, PancreasFest Working Group and European Pancreatic Club,” *Pancreatol. Off. J. Int. Assoc. Pancreatol. IAP Al*, May 2018, doi: 10.1016/j.pan.2018.05.008.

[29] M. E. Lowe *et al.*, “Precision Medicine in Pancreatic Disease-Knowledge Gaps and Research Opportunities: Summary of a National Institute of Diabetes and Digestive and Kidney Diseases Workshop,” *Pancreas*, vol. 48, no. 10, pp. 1250–1258, Dec. 2019, doi: 10.1097/MPA.0000000000001412.

[30] J. G. D‘Haese(1), D. L. Cahen(2), and J. Werner(1), “Current Surgical Treatment Options in Chronic Pancreatitis,” *Pancreapedia Exocrine Pancreas Knowl. Base*, Aug. 2016, doi: 10.3998/panc.2016.26.

[31] H. Matthews, J. Hanison, and N. Nirmalan, “‘Omics’-Informed Drug and Biomarker Discovery: Opportunities, Challenges and Future Perspectives,” *Proteomes*, vol. 4, no. 3, Sep. 2016, doi: 10.3390/proteomes4030028.

[32] Y. Hasin, M. Seldin, and A. Lusis, “Multi-omics approaches to disease,” *Genome Biol.*, vol. 18, no. 1, p. 83, May 2017, doi: 10.1186/s13059-017-1215-1.

[33] S. Li, R. Li, H. Wang, L. Li, H. Li, and Y. Li, “The Key Genes of Chronic Pancreatitis which Bridge Chronic Pancreatitis and Pancreatic Cancer Can be Therapeutic Targets,” *Pathol. Oncol. Res. POR*, vol. 24, no. 2, pp. 215–222, Apr. 2018, doi: 10.1007/s12253-017-0217-3.

[34] N. Sanh *et al.*, “Proteomics Profiling of Pancreatic Cancer and Pancreatitis for Biomarkers Discovery,” *J. Cell Sci. Ther.*, vol. 9, no. 4, 2018, doi: 10.4172/2157-7013.1000287.

[35] X. Li, L. Zhu, B. Wang, M. Yuan, and R. Zhu, “Drugs and Targets in Fibrosis,” *Front. Pharmacol.*, vol. 8, Nov. 2017, doi: 10.3389/fphar.2017.00855.

[36] S. Herbertz *et al.*, “Clinical development of galunisertib (LY2157299 monohydrate), a small molecule inhibitor of transforming growth factor-beta signaling pathway,” *Drug Des. Devel. Ther.*, vol. 9, pp. 4479–4499, Aug. 2015, doi: 10.2147/DDDT.S86621.

[37] W. Xiao *et al.*, “Retinoic Acid Ameliorates Pancreatic Fibrosis and Inhibits the Activation of Pancreatic Stellate Cells in Mice with Experimental Chronic Pancreatitis via Suppressing the Wnt/β-Catenin Signaling Pathway,” *PloS One*, vol. 10, no. 11, p. e0141462, 2015, doi: 10.1371/journal.pone.0141462.

[38] L. CHEN and W. ZHAO, “Apigenin protects against bleomycin-induced lung fibrosis in rats,” *Exp. Ther. Med.*, vol. 11, no. 1, pp. 230–234, Jan. 2016, doi: 10.3892/etm.2015.2885.

[39] J. Zhang *et al.*, “The potential application of strategic released apigenin from polymeric carrier in pulmonary fibrosis,” *Exp. Lung Res.*, vol. 43, no. 9–10, pp. 359–369, Dec. 2017, doi: 10.1080/01902148.2017.1380086.

[40] W. Wu *et al.*, “The Targeted-liposome Delivery System of Antitumor Drugs,” *Curr. Drug Metab.*, vol. 16, no. 10, pp. 894–910, 2015, doi: 10.2174/1389200216101512101846 54.

3.11 Supplement

Figure S3.1. The size distribution of peptide modified liposomes detected by NanoSight. (A) NP liposomes. (B) MDLSLKP liposomes. (C) MNSIAIP liposomes.

A

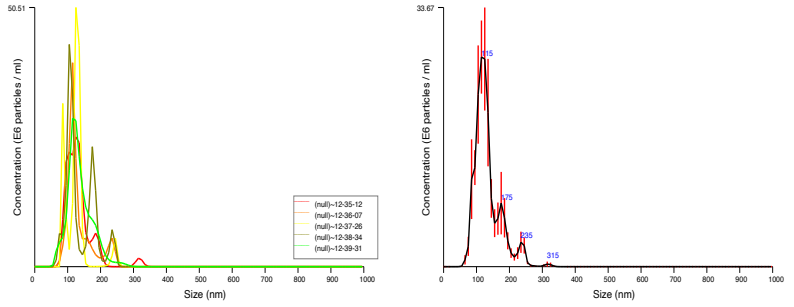

B

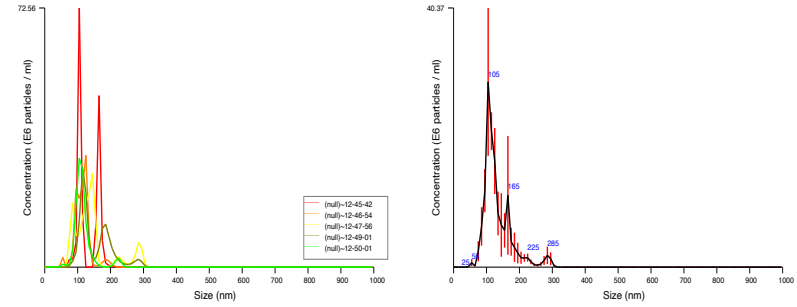

C

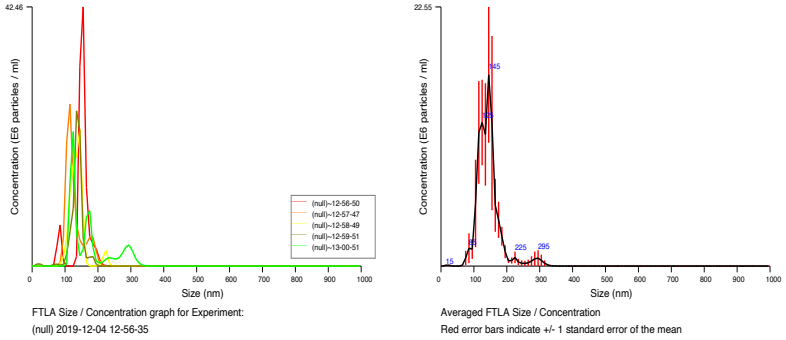

Figure S3.2. Targeted liposomal delivery of apigenin reduces hepatotoxicity. (A) Chemistry test results generated from serum samples collected from vehicle, free drug-, Api-Naked Lip- and Api-ECM Lip-treated CP mice revealing statically significant reduction of toxic effects of the apigenin-based treatment to the mice livers (p-value = 0.0196). No significant toxic effects induced to mice kidneys is observed in all treatments. Mean +/- SEM, N=3. (B) Representative H&E staining of livers. Scale bar: 100 µm. (C) Western blot images and the quantification of liver lysates from treated CP mice probing for SOD1. Mean +/- SEM, N = 5, *p-value = 0.0491.

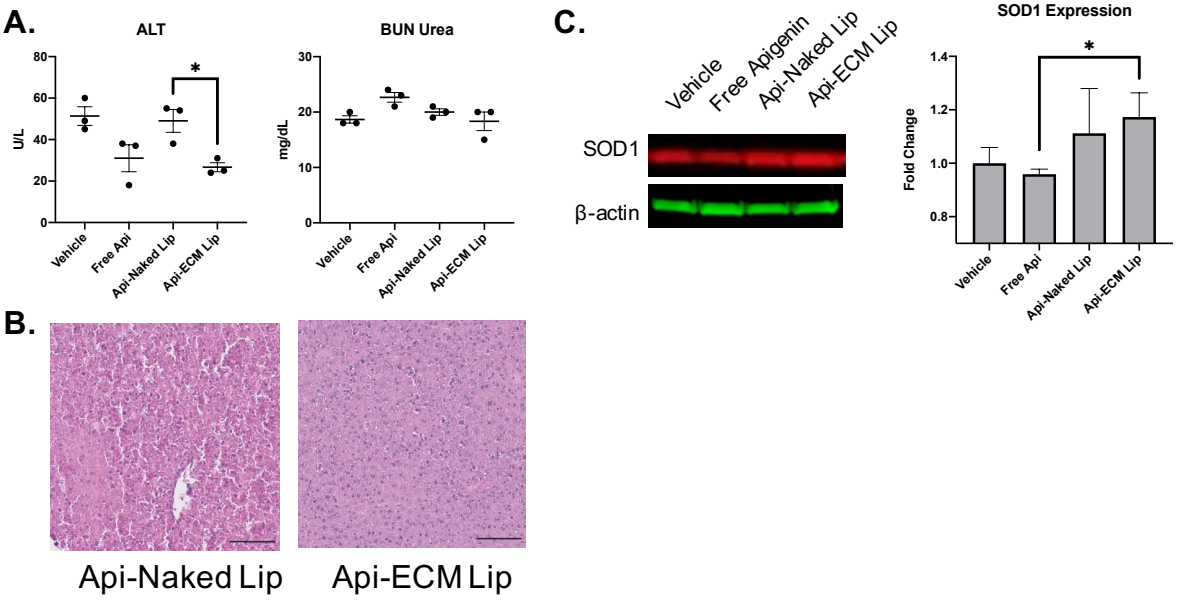

Table S3.1. P-values for statistical test performed on Manders' correlation coefficients of phage clones overlapping with cell markers. One-way ANOVA and Tukey-Kramer method were used for all tests. The result was considered significant if the p-value ≤ 0.05. ns: not statistically significant.

Figure	Phage clone	MCC Comparison	Adjusted P-value	Summary
Figure 3.1B	MDLSLKP	Col IIIa vs αSMA	<0.0001	****
Figure 3.1B		Col IIIa vs CD31	<0.0001	****
Figure 3.1B		Col IIIa vs CK7	<0.0001	****
Figure 3.1B		Col IIIa vs CPA-1	<0.0001	****
Figure 3.1B		Col IIIa vs F4/80	<0.0001	****
Figure 3.1B	SLPLGPM	F4/80 vs αSMA	0.0023	**
Figure 3.1B		F4/80 vs CD31	0.0448	*
Figure 3.1B		F4/80 vs CK7	<0.0001	****
Figure 3.1B		F4/80 vs Col IIIa	0.0284	*
Figure 3.1B		F4/80 vs CPA-1	0.4832	ns
Figure 3.1B	HPYSPLR	F4/80 vs αSMA	<0.0001	****
Figure 3.1B		F4/80 vs CD31	0.8189	ns
Figure 3.1B		F4/80 vs CK7	<0.0001	****
Figure 3.1B		F4/80 vs Col IIIa	0.082	ns
Figure 3.1B		F4/80 vs CPA-1	0.0342	*
Figure 3.1B	KTYVPTT	αSMA vs CD31	<0.0001	****
Figure 3.1B		αSMA vs CK7	<0.0001	****
Figure 3.1B		αSMA vs Col IIIa	0.0003	***
Figure 3.1B		αSMA vs CPA-1	0.0006	***
Figure 3.1B		αSMA vs F4/80	0.0095	**
Figure 3.1B	SLTNSSF	F4/80 vs αSMA	<0.0001	****
Figure 3.1B		F4/80 vs CD31	<0.0001	****
Figure 3.1B		F4/80 vs CK7	<0.0001	****
Figure 3.1B		F4/80 vs Col IIIa	<0.0001	****
Figure 3.1B		F4/80 vs CPA-1	<0.0001	****
Figure 3.1B	MNSIAIP	CPA-1 vs αSMA	<0.0001	****
Figure 3.1B		CPA-1 vs CD31	<0.0001	****
Figure 3.1B		CPA-1 vs CK7	<0.0001	****
Figure 3.1B		CPA-1 vs Col IIIa	<0.0001	****
Figure 3.1B		CPA-1 vs F4/80	0.0002	***
Figure 3.1B	SNSQDLH	F4/80 vs αSMA	<0.0001	****
Figure 3.1B		F4/80 vs CD31	<0.0001	****
Figure 3.1B		F4/80 vs CK7	<0.0001	****
Figure 3.1B		F4/80 vs Col IIIa	<0.0001	****
Figure 3.1B		F4/80 vs CPA-1	<0.0001	****

Table S3.2. P-values for statistical test performed on Manders' correlation coefficients of liposomes overlapping with cell markers. One-way ANOVA and Tukey-Kramer method were used for all tests. The result was considered significant if the p-value ≤ 0.05. ns: not statistically significant.

Figure	Liposome	MCC Comparison	Adjusted P-value	Summary
Figure 3.3B	MDLSLKP	Col IIIa vs αSMA	<0.0001	****
Figure 3.3B		Col IIIa vs CD31	<0.0001	****
Figure 3.3B		Col IIIa vs CK7	<0.0001	****
Figure 3.3B		Col IIIa vs CPA-1	<0.0001	****
Figure 3.3B		Col IIIa vs F4/80	0.0012	**
Figure 3.3B	MNSIAIP	CPA-1 vs αSMA	0.0005	***
Figure 3.3B		CPA-1 vs CD31	0.3179	ns
Figure 3.3B		CPA-1 vs CK7	0.0013	**
Figure 3.3B		CPA-1 vs Col IIIa	0.9882	ns
Figure 3.3B		CPA-1 vs F4/80	0.9746	ns
Figure 3.3B	NC Liposome	F4/80 vs αSMA	<0.0001	****
Figure 3.3B		F4/80 vs CD31	<0.0001	****
Figure 3.3B		F4/80 vs CK7	<0.0001	****
Figure 3.3B		F4/80 vs Col IIIa	<0.0001	****
Figure 3.3B		F4/80 vs CPA-1	<0.0001	****

Chapter 4. A bitter taste receptor as a novel molecular target for cancer-associated fibroblast in pancreatic ductal adenocarcinoma

Jessica Hung[1], Siva Sai Krishna Dasa[2], Julien Dimastromatteo[2], Howard C. Crawford[3,4], Lindsey T. Brinton*[5], and Kimberly A. Kelly*[2].

1. Department of Biomedical Engineering, School of Engineering, University of Virginia, Charlottesville, Virginia 22908, United States of America.
2. Department of Biomedical Engineering, School of Medicine, University of Virginia, Charlottesville, Virginia 22908, United States of America.
3. Department of Molecular and Integrative Physiology, University of Michigan, Ann Arbor, Michigan 48109, United States of America.
4. University of Michigan Ragel Cancer Center, University of Michigan, Ann Arbor, Michigan 48109, United States of America.
5. ZielBio Inc., Charlottesville, Virginia 22903, United States of America.

*These authors contributed equally.

Keywords: *cancer-associated fibroblast, CXCR2 inhibitor, Taste receptor, T2R9, targeted liposome*

At this point, the text in this chapter is from a manuscript in preparation.

4.1 Abstract

Cancer-associated fibroblasts (CAFs) interact with the tumor microenvironment to regulate tumor progression, immunosuppression, metastasis, and chemoresistance in pancreatic cancer. Targeting CAFs to reprogram the crosstalk between CAFs and cancer epithelial cells presents a promising therapeutic avenue, evading the adverse clinical effects of stromal depletion. Drugs to reprogram the CAF exist, however their suboptimal pharmacokinetics and off-target effects limit their use. The ability to specifically target these drugs via CAF-specific cell surface markers allows for increased efficacy while eliminating toxicity accessing the stroma as a viable therapeutic strategy. Here, we identified a G-protein coupled receptor, taste receptor type 2 member 9 (T2R9), as being overexpressed in CAFs. T2R9 mRNA is upregulated 57-fold in CAFs compared to normal fibroblasts. As proof of concept, we developed a T2R9-targeted liposome and demonstrated liposomal specific binding to T2R9 recombinant protein as well as stromal colocalization in a murine pancreatic cancer model. Encapsulation of the CXCR2 inhibitor SB225002 in the T2R9-targeted liposomes significantly reduced cell proliferation and constrained tumor growth through inhibiting the downstream pathways associated with the CXCL-CXCR2 axis. In summary, we have identified a novel protein present on CAFs that could provide valuable insights into CAF-tumor biology and paves the way for stromal therapy.

4.2 Introduction

Pancreatic ductal adenocarcinoma (PDAC) is the fourth leading cause of cancer-related deaths worldwide and is one of the few cancers with a 5-year survival rate that remains in the single digits (9%) [1, 2]. The poor clinical outcomes reflect the lack of effective treatments and singular approach of targeting the cancer epithelial cells while ignoring the rest of the tumor. Emerging evidence supporting the importance of stroma in PDAC development led to therapeutic approaches that act on the tumor microenvironment (TME) through stromal depletion. Clinically (NCT01130142, NCT01959139), depletion of cancer associated fibroblast (CAFs) resulted in a more aggressive tumor phenotype, helping tumor immune evasion and development of chemoresistance [3, 4]. These disappointing results emphasize the complex roles of stroma in balancing tumor-promoting and -restraining functions [5, 6].

PDAC is composed of extensive desmoplastic stroma that occupies >70% of total tumor volume [7, 8]. As the most abundant cellular components in PDAC TME, CAFs form complex networks with tumor epithelial cells, immune cells, and endothelial cells and play an integral role in regulating acellular stromal components (collagen, hyaluronan, chemokines, and cytokines), tumor progression, immunosuppression, metastasis, and drug resistance [9–12]. In contrast to depletion, reprogramming the crosstalk between CAFs, TME, and cancer cells offers the potentials to tune CAF's role away from tumor-promoting and illuminates a therapeutic potential. For example, Sano et al. showed that cancer cells and CAF promoted one another's invasion and migration through the CXC chemokines-receptor (CXCLs-CXCR2) axis, and they further showed that blocking the CXCLs-CXCR2 axis inhibited PDAC microinvasion and prolonged survival [13]. In addition, Biffi et al. revealed TGF-β and IL1/JAK/STAT signaling pathways are responsible for the heterogeneity of CAFs, and a JAK inhibitor shifted CAFs from inflammatory to a myofibroblastic phenotype and decreased tumor growth [14]. Taken together, these studies highlight the essential roles of CAFs in tumor progression, and that reprogramming the CAF-tumor or CAF-TME communications, in contrast to ablation, may help prolong patient survival.

In previous studies, we have identified a novel peptide sequence, HTTIPKV, specific for CAF originated from PDAC patients using phage display-based functional proteomics [15]. We bioinformatically confirmed the HTTIPLV peptide tissue selectivity against our peptide signature

database—spanning 56 cell lines and tissues, as well as demonstrated in vitro and in vivo CAF selectivity. As the peptide is selective for CAFs, in this work we identified the binding partner of the peptide as Taste Receptor type 2 Member 9 (T2R9). Taste receptors type 2 family (TAS2Rs) are G protein-coupled receptors (GPCRs) for bitter stimuli detection in the oral cavity, but are also expressed in the airway epithelium and the gastrointestinal tract [16, 17]. For the first time, we report and validate T2R9 expression in pancreatic CAFs and demonstrate that T2R9 is a viable molecular target for stroma-directed therapy.

For proof of concept, we encapsulated the CXCR2 inhibitor, SB225002, in a T2R9-targeted liposome (TTL). CXCR2 is a GPCR for CXC chemokines (CXCL1-3, CXCL5-8) and is involved in inflammation, angiogenesis, tumorigenesis, and metastasis through tumor-stroma interaction [13, 18–20]. Pharmacological inhibition of CXCR2 improved T cell infiltration in KPC mice and enhanced sensitivity to anti-PD1 immunotherapy [19]. Despite these promising features, the safety of systematic CXCR2 inhibitors remains questionable as these small molecule drugs disrupt neutrophil chemotaxis and activation, resulting in an increased risk of developing neutropenia in cancer patients who already suffer from a compromised immune system [21]. Thus, we sought to evaluate the pharmacokinetics and pharmacological responses of SB225002 encapsulated in TTL. Our results demonstrated targeted liposome's specificity to the recombinant T2R9 protein and stroma in vivo and showed an increase in tumor accumulation by 1.9-fold when compared to negative control (NC) liposome. In an admix PDAC mouse model bearing BXPC3 and CAF xenograft, we observed a significant reduction in tumor growth and cell proliferation in animals treated with drugs delivered by TTL compared to NC liposome or systematic delivery. We also showed a 3.3-fold reduction in CTGF expression, a downstream molecule of the CXCLs-CXCR2 axis, in TTL than the systematic drug. The discovery of T2R9 in pancreatic CAFs represents an important target for improved therapeutic interventions in PDAC and signifies a tractable method of re-engineering PDAC stroma for improved patient outcomes.

4.3 Materials and Methods

4.3.1 Animals

All experiments were performed on male 6-8-week-old athymic nude mice purchased from Harlan Sprague Dawley Inc. (Indianapolis, IN). All animal experiments were approved by the Animal Care and Use Committee at the University of Virginia and conformed to the NIH "Guide for the Care and Use of Laboratory Animals in Research."

4.3.2 Cell lines

CAFs, obtained from Dr. Diane Simeone (NYU Langone Medical Center, New York City, NY), and BXPC3s (American Type Culture Collection (ATCC), Manassas, VA) were grown in RPMI medium 1640 (Life Technologies, Carlsbad, CA). Human dermal fibroblasts (HDFs) were obtained from Dr. Jennifer Munson (Virginia Polytechnic Institute and State University, Blacksburg, VA) and grown in DMEM (Life Technologies). The RPMI and DMEM media were supplemented with 10% fetal bovine serum, 1% penicillin/streptomycin, and 1% L-glutamine. All cells were maintained in a humidified atmosphere containing 5% CO_2 at 37℃.

4.3.3 Lipids and peptides for liposome preparation

1,2-Dioleoyl-sn-glycerol-3-phosphocholine (DOPC), and 1,2-distearoyl-sn-glycero-3-phosphoethanolamine-N-[methoxy(polyethylene glycol)-2000] (DSPE-PEG_{2000}) were purchased from Avanti polar lipids, Miami, FL; DSPE-PEG_{3400}-maleimide was purchased from Laysan Bio Inc., Arab, AL; 1,1'-Dioctadecyl-3,3,3',3'-tetramethylindotricarbocyanine iodide (DiR) was purchased from Biotium Inc., Hayward, CA; cholesterol was purchased from Millipore Sigma, Burlington, MA. Peptides were synthesized by the Tufts University Peptide Synthesis Core Facility using standard FMOC chemistry and Rink-Amide resin (Tufts University, Boston, MA).

4.3.4 Phage-based pulldown assay

The binding partner of phHTTIPKV was identified using a phage display-based pulldown assay [22]. In brief, CAFs were cultured in 10 cm dishes overnight prior to allow binding to phage. $1x10^{12}$ plaque-forming unit (pfu) phHTTIPKV or control phage M13KE (200uL) were biotinylated

in 5µL of 0.2 µg/µL NHS-biotin in DMSO, 5µL of 50 µg/µL Sulfosuccinimidyl 2-[7-amino-4-methylcoumarin-3-acetamido]ethyl-1,3´dithiopropionate (sulfo-SAND) in DMSO, and 100µL 50 mM carbonate buffer (pH 9.0) for 15min, RT. A negative control using M13KE phage (New England BioLabs, Ipswitch, MA), which does not contain the insert coding region for the displayed peptides, was utilized. The biotinylated phage were isolated by by PEG/NaCl (2.5mM NaCl + 80% v/v PEG-8000) precipitation [23] and covalently cross-linked to CAFs by exposing to 10 mW UV light for 15 min, on ice. Cells were lysed in 1mL of PBS lysis buffer containing 1x protease inhibitor cocktail (Fisher Scientific, Hampton, NH), 10 µL EDTA, and 10uL Triton X-100. Cell lysates were then mixed with 200 µL Pierce Streptavidin Agarose (Thermo Scientific, Waltham, MA) following the manufacturer's instructions. The extracts were eluted in 50 µL of 50 mM NaCl/130 mM DTT for 15 min, and neutralized in 50 µL of 0.1M Glycine (pH 2.2) for 5 min. The eluted complexes were mixed with 4x Laemmle buffer (Bio-Rad, Hercules, CA) and loaded into precast 4-15% tris-glycine eXtended (TGX) polyacrylamide gels (Bio-Rad, Hercules, CA), followed by silver staining (SilverQuest Silver Staining Kit, Life Technologies, Carlsbad, CA). By comparing to the pulldowns of the M13KE phage, the gel pieces of the unique bands present in the pulldowns of HTTIPKV phage was cut for mass spectrometry (MS/MS) analysis. The LC-MS system consisted of a Thermo Electron Orbitrap Velos ETD mass spectrometer system with a Protana nanospray ion source interfaced to a self-packed 8 cm x 75 um id Phenomenex Jupiter 10 um C18 reversed-phase capillary column. The peptides and proteins identified for the sample were displayed using Scaffold (v4.8.9) with the following settings (parent = 10 ppm, fragment = 1.00 Da, Trypsin, 80% peptide threshold, 80% protein threshold).

4.3.5 T2R9 siRNA/shRNA lentivirus transduction

50,000 CAFs were seeded in a 24-well plate and cultured for 24 h, at which time the cells were treated with medium containing T2R9 (human) siRNA/shRNA Lentivirus (piLenti-siRNA-GFP, Applied Biological Materials, Richmond, BC, Canada) at MOI = 10 and 8 µg/mL of polybrene. Fresh culture medium was replenished 24 h post-induction of lentivirus. The transduced cells were sorted based on GFP expression using FACS Aria Fusion Cell Sorter (BD Bioscience, San Jose, CA)

and cultured in medium containing 1 µg/mL puromycin (Millipore Sigma, Burlington, MA) to maintain stable cell lines.

4.3.6 Quantitative PCR

Cells were cultured in 10-cm dishes and cultured for 24 h, at which time RNA was isolated according to the manufacturer's instructions (RNAeasy Mini kit, Qiagen), followed by DNase I reaction (DNase Max Kit, Qiagen, Hilden, Germany). The concentration and purity were determined using a NanoDrop spectrophotometer (Thermo Fisher, Waltham, MA). Complementary DNA (cDNA) was generated (Qiagen QuantiTect Reverse Transcription Kit) and subjected to pre-amplification (Qiantitect SYBR Green PCR Kit). In this reaction, 60 nM of each primer, T2R9 (Forward: 5'-GATGGTTCCCTTTATCCTTTGC-3'; Reverse: 5'-CCCTCATGTGGGCCTCTGTA-3') and 18s (Forward: 5'-GTAACCCGTTGAACCCCATT-3'; Reverse: 5'-CCATCCAATCGGTAGTAGCG-3') were mixed with cDNA template and SYBR green master mix and subjected to the following thermal cycling protocol: 15 min at 95℃, followed by 55 cycles of 15 sec at 94℃, 30 sec at 52℃, and 45 sec at 72℃ and 4 min. The normalized gene expression was determined by the delta delta Ct method.

4.3.7 Competitive ELISA

HTTIPKV peptide was iodinated using chloramine-T oxidation method [24]. Briefly, we added 40µg of HTTIPKV peptide (2mg/ml) to 18MBq Iodine-125 (Cardinal Health, Dublin, OH). We added 20µl Chloramine-T (20mg/ml) to trigger the oxidative reaction. We added 20µl Sodium-Metabisulfate (20mg/ml) to stop the reaction after 1 minute. We separated radiolabeled from unlabeled peptides using SepPack C-18 cartridge. Radiochemical Purities (RCP) were assessed using thin layer chromatography (methanol/water - 75/25). The RCPs were >93%. I-125-labeled HTTIPKV peptide (10,000 cpm, 1nM) was incubated with an excess amount of recombinant human T2R9 protein (Novus Biologicals, 100nM) in 1% BSA/PBS for 30 min at room temperature. 5000 CAF cells per well were seeded in 96-well plates and cultured for 24 h. 100 µL of I-125-labeled HTTIPKV alone or 100 µL of the I-125-HTTIPKV/rhT2R9 complex were added to CAFs, respectively, for 1 h on ice. Cells were washed with ice-cold PBS, 5 times, and then fixed

with 4% PFA for 10 min on ice. Wash the cells again with ice-cold PBS and elute the bound complexes with 50 µL of 100mM glycine (pH 2.0) for 10 min at room temperature and neutralized with 50 µL of 100mM Tris (pH 9.0). Radioactivity was measure on a gamma counter (Wallac Wizard Model 1470) using the detection energy window 15-75KeV.

4.3.8 Western blot

CAFs and T2R9 (-) CAFs were cultured in 10 cm dishes until 95% confluency. Cells were washed with HBSS and lysed with radioimmunoprecipitation assay (RIPA) buffer (Thermo Scientific). The lysate was deglycolysated with PNGase F (New England BioLabs, Ipswich, MA) following manufacture's protocol. Lysate protein concentration was measured by the bicinchoninic acid assay (BCA, Peirce BCA Protein Assay Kit, Thermo Fisher Scientific, Waltham, MA), and an equal amount of proteins was loaded into precast 4-15% TGX polyacrylamide gels (Invitrogen). The proteins were resolved by electrophoresis and transferred to nitrocellulose membranes. The membrane was incubated in denature buffer (62.5 mM Tris-HCl, pH6.8, 2% SDS, and 100 mM βME) at 55℃ for 15 min. The membranes were then washed twice in PBS, blocked for 1h in 50/50 PBS/Odyssey blocking buffer (LI-COR Bioscience, Lincoln, NE), and incubated overnight at 4 ℃ with primary antibodies anti-T2R9 (Abcam; 1:100) and anti-β-actin (Cell Signaling Technology, Danvers, MA; 1:1000) in the blocking buffer. The following day the membranes were washed and subsequently incubated with the secondary antibodies IRdye donkey anti-rabbit 680RD (LI-COR Bioscience; 1:5000). Anti-β actin antibody and the secondary antibodies IRdye donkey anti-mouse 800CW (LI-COR Bioscience; 1:5000) were used as a loading control. Fluorescent signals were detected on the Li-COR Odyssey Fluorescent Imager (LI-COR Bioscience) and analyzed with Image Studio Lite (LI-COR Bioscience, v5.2.5).

Tumors were homogenized (N = 3 per group) and the total protein concentration was measured by Perice660 protein assay (Thermal Fisher Scientific Inc, Waltham, MA) for each tumor lysates. An equal amount of proteins was loaded into precast 4-15% TGX gel, resolved by electrophoresis, and transferred to nitrocellulose membranes using the iBlot system (Bio-Rad, source). The membranes were washed in Tris-buffered saline + 1% Tween-20 (TBST), blocked for 1 h in the blocking buffer, and incubated overnight at 4℃ in anti-CTGF antibody (Abcam),

followed by secondary antibody anti-rabbit HRP (1:1000). Anti-β actin antibody and the secondary antibody, anti-mouse HRP (1:1000) was used as a loading control. After washing, the membranes were incubated in lumino/peroxide substrate reagents (Millipore, Burlington, MA), exposed to HyBlot autoradiography film (Denville Scientific, South Plainfield, NJ). The developed film was scanned for densitometry.

4.3.9 Immunofluorescent staining

40,000 cells were seeded in each well of a Millicell EZ SLIDE 4-well glass (Millipore, Burlington, MA) and cultured for 24 h. Cells were washed with HBSS, fixed for 10 min with 4% PFA on ice, blocked for 1 h in blocking buffer, incubated for 1 h with anti-T2R9 antibody (Bioss Antibodies, Woburn, MA) at 1:100, followed by washes and incubation for 1 h in goat anti-rabbit secondary antibody (IgG conjugated Alexa fluor-647, 1:500, Abcam, Cambridge, MA). Cells were then incubated with Wheat Germ Agglutinin (WGA), Alexa Fluor 488 Conjugate (Invitrogen, Carlsbad, CA) for 10 min prior to mounting with ProLong Gold Antifade Mountant (Thermo Fisher Scientific Inc, Waltham, MA).

Tumor sections were blocked for 1 h in blocking buffer and incubated with FITC-conjugated anti- α-SMA (Sigma, 1:200 1 h), anti-CTGF (Abcam, 1:200, 20 min) then anti-rabbit secondary (1:250, 20 min), anti-CD31 (BD biosciences, 1:100, 20 min) then anti-rat secondary (1:250, 20 min), or anti-Ki67 (Abcam, 1:250, 20 min) then anti-rabbit secondary (1:250, 20 min). Images were collected using ZEISS LSM-880 Confocal Laser Scanning Microscope (Carl Zeiss Meditec, Inc., Jena, Germany). Mander's correlation coefficients were determined using the JACoP plugin in ImageJ (National Institute of Health, Bethesda, MD) for the co-localization analysis. To characterize CD31 and Ki67 expression, the area fraction of the positive pixels was measured for each image using the Measurement Tool in ImageJ. Section averages were entered into Prism to find overall means for each treatment group and tested for statistical significance between groups using the Student's t-test.

4.3.10 Immunohistochemistry

Immunohistochemistry staining of T2R9 was performed on human intraductal papillary mucosal neoplasms (IPMNs) and pancreatic ductal adenocarcinoma (PDAC) tissues using anti-Tas2r9 antibody (ThermoFisher OSR00157W) at 1:2000 and anti-rabbit HRP as 2'-antibody.

4.3.11 Preparation and characterization of liposomes

[H]-HTTIPKVGGSK(fitc)C-[NH2] peptide was synthesized and purified at Tufts University Peptide Synthesis Core Facility. Drug encapsulated Liposomes is prepared using the ethanol injection method [25]. In brief, 4 mg of FITC-labeled peptide was dissolved in 900 µL of degassed PBS/1 mM EDTA and 9 mg of DSPE-PEG3400-maleimide dissolved in 100 µL methanol. The two solutions were combined while bubbling with argon gas and then freeze-dried. 20.5 mg DOPC, 9.5 mg DSPC-cholesterol, 9.5 mg DSPE-PEG2000, 1 mg freeze-dried DSPE-PEG3400- maleimide-conjugated peptide, and 0.5 mg DiR (Invitrogen) in methanol (25 mg/mL) were dissolved in 2 mL chloroform (Sigma-Aldrich). After evaporation, the lipid layer was hydrated by adding 2 mL saline and subjected to three freeze-thaw cycles. For the drug loaded liposomes, liposomes were prepared in the same procedure as described, but instead of hydrating the lipid membrane in saline, hydration was done in solution containing SB225002 (Tocris Bioscience, Bristol, UK), 0.5 mg/mL. The liposomes were sized by passing the solution 41 times through a manual extruder with a 0.2 µm Nuclepore filter (Thermo Fisher Scientific, Inc., Waltham, MA). The size-extruded liposomes were characterized by Nanosight NS300 (Malvern Instruments Ltd., Worcestershire, UK) to determine particle size and concentration. Zeta potential was measured using a ZetaSizer 3000HSA (Malvern Panalytical, Westborough, MA), in 10mM HEPES buffer (pH 7.4) at 25℃.

4.3.12 Liposome binding assay

Biolayer interferometry (BLI) was performed using ForteBio octect Red 96 system (ForteBio, Menlo Park, CA) in black 96-well plates (Nunc F96 Micro Well plates, Thermo Fisher, Waltham, MA). The total working volume for samples or buffer was 0.2 mL per well, and the rpm setting for each equilibration and loading step was set at 1000 rpm. The association and dissociation step with T2R9 and peptide-liposomes was carried out at 600 rpm. Prior to each

assay, anti-his biosensor tips were pre-wetted in 0.2 mL PBS for at least 10 min followed by equilibrium with PBS for 100 s. Anti-his biosensors were then non-covalently loaded with his-tagged T2R9 (50-200 g/mL, 100 s). Subsequently, association with NC and HTTIPKV liposomes (40 mM, 300 s) was carried out. Finally, the dissociation was monitored in PBS for 600 sec.

4.3.13 Tumor studies

For tumor implantation, BXPC3 and CAF cells were grown under standard culture conditions for 48 h prior to being trypsinized and enumerated. BXPC3s were suspended in 500,000 cells/25 µL DPBS, CAFs in 1,500,000 cells/25 µL DPBS, and 50 µL of Matrigel (BD Biosciences, San Jose, CA) was added to each aliquot of admix cells prior to implantation. The cell-Matrigel slurry containing 2 million cells was injected subcutaneously into nude mice on the flanks, 2 tumors per animal. The tumor volume was calculated from caliper measurements using the formula $(\text{width}^2 \times \text{length})/2$. For liposome PK study, after tumors reached the size of 100 mm^3, dye-labeled liposomes (50,000 pmol DiR) were injected intravenously via tail vein. Fluorescent intensity was measured by the Fluorescent Molecular Tomography (FMT, PerkinElmer, Waltham, MA) daily from day 0 to day 14 post liposome injection. Post 14 days of imaging, tumors were harvested and submerged in Neg-50 Frozen Section Medium (Thermo Scientific, Waltham, MA) and snap-freezing by placing on top of liquid nitrogen vapor. The embedded tissues were cut into 5 µm sections using a cryostat (Leica Microsystems Inc., Buffalo Grove, IL) for subsequent immunofluorescent staining.

For SB225002 treatment study, after tumors reached the size of 100 mm^3, mice bearing subcutaneous admix BXPC3/CAF xenografts on both flanks were grouped into 4 treatment regimens (n = 5-6/group): 1) untreated, 2) free SB225002 (0.5 mg/kg per intraperitoneal injection, 5x/week)[21], 3) SB225002-loaded NC liposomes (0.83 mg/kg per intravenous injection, 3x/week), and 4) SB225002-loaded HTTIPKV liposomes (0.83 mg/kg per intravenous injection, 3x/week). The drug dosage was calculated for each treatment to achieve the same weekly amount of SB225002 given per animal. Tumor volume were calipered twice weekly until day 19, at which time the tumors were harvested for cell proliferation (Ki67) and angiogenesis (CD31) analysis and homogenized for detection CTGF expression on Western blot.

4.3.14 Pharmacokinetics

The accumulation and clearance coefficient for liposomes in tumors were determined using linear regression on the log transformations of the two-week tumor accumulation time course. The fit line was evaluated and compared to the experimental data in MATLAB. Total liposome accumulation was estimated from the area under the curve (AUC) from the projected fit line in MATLAB (The MathWorks Inc., Natick, MA).

4.3.15 Statistical analysis

Statistical analysis of the data was performed by student t-test. All data presented are expressed as mean $\pm$ standard error of at least three independent measurements. For all comparisons, p-value < 0.05 was considered significant.

4.4 Results

4.4.1 T2R9 is upregulated in CAFs of PDAC

Using PHASTpep, we previously identified a 7-amino acid peptide, HTTIPKV, and demonstrated its specificity to CAFs isolated from stroma of patients with PDAC [15]. As HTTIPKV bound specifically and selectively to CAFs, we hypothesized that the binding partner of HTTIPKV could serve as a potential cellular marker and therapeutic target for CAFs. To identify the binding partner, we used phage display-based functional proteomics, which utilizes chemically modified phage displaying HTTIPKV (phHTTIPKV) as "bait" to capture the protein on the cell that is binding to the peptide [22]. Samples were analyzed via SDS-PAGE and revealed the presence of a unique band in the HTTIPKV sample when compared with the wildtype (WT) M13KE phage (Figure 4.1A). The unique band was excised, digested with trypsin and analyzed via mass spectrometry, revealing the identity of the candidate protein as T2R9. Two unique tryptic digest fragments were identified, matching 12% coverage of the human T2R9 amino acid sequences (Figure S4.1). To demonstrate phHTTIPKV binding to T2R9, we performed a binding assay using recombinant T2R9 protein. HTTIPKV was radiolabeled with I-125 and incubated with absorbed T2R9 recombinant protein. As a control, I-125-HTTIPKV was pre-incubated with T2R9 for 1h then the mixture added to a well containing absorbed T2R9. I-125-HTTIPKV bound to T2R9 and was competed when pre-bound to T2R9 indicating specific binding of HTTIPKV to T2R9 (Figure 4.1B).

Expression of T2R9 in CAF was determined using two methods, qPCR and western blot. We assessed the expression level of T2R9 mRNA in CAFs using T2R9 specific primers and qPCR. As a specificity control, we generated T2R9 knockdown cells using lentivirus. qPCR demonstrated the presence of T2R9 mRNA in CAF cells and an 80.25% reduction in T2R9 mRNA expression in T2R9 siRNA (siT2R9) transduced cells (Figure 4.1C, $p = 0.0053$; Figure S4.2). The end-point products of the qPCR reactions revealed a unique band at the predicted amplicon size (161 base pairs, b.p.), indicating specificity of the T2R9 primers (Figure 4.1D). Primers against 18s ribosomal RNA was used as a housekeeping control, and reactions without reverse transcriptase (RT) added were used as internal negative controls for the qPCR reaction. To assess T2R9 expression on the

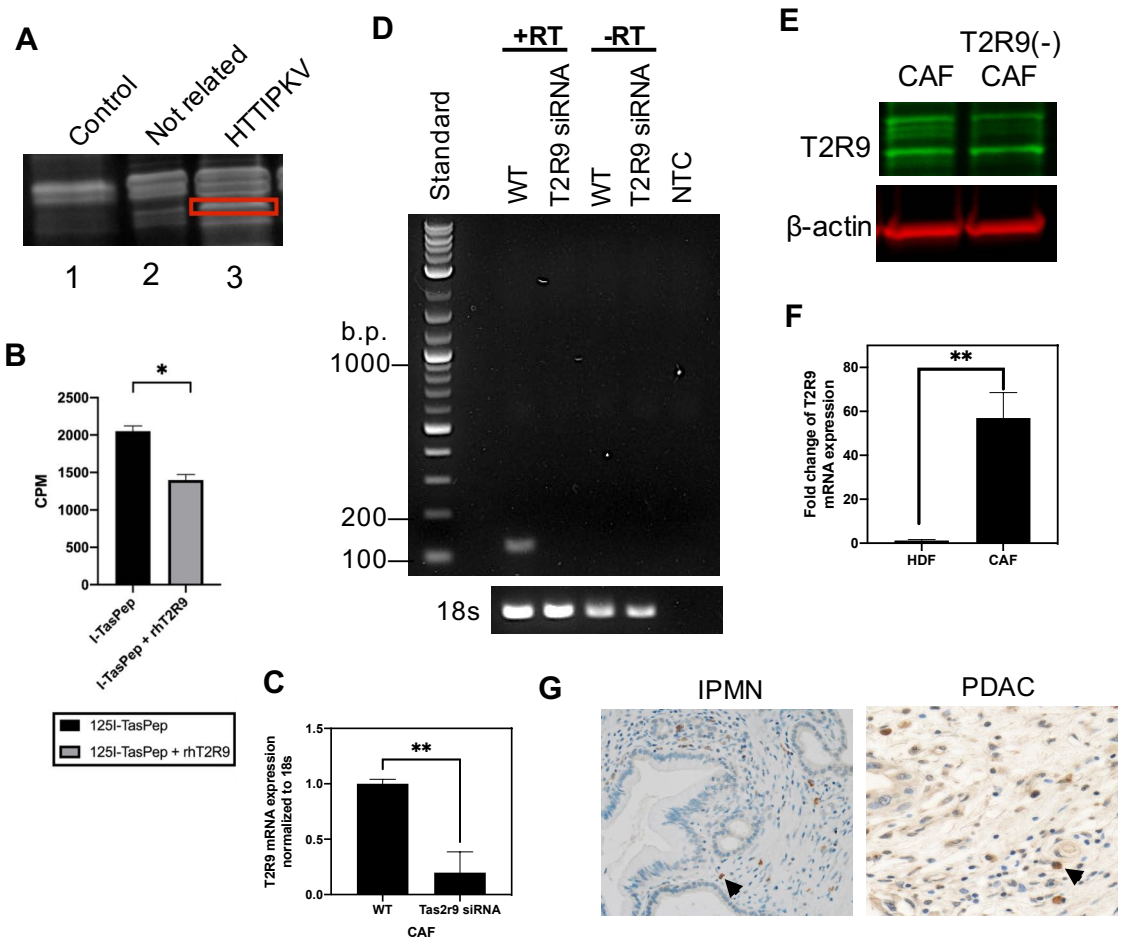

Figure 4.1. T2R9 expression in CAFs isolated from human PDAC. (A) Phage pulldown of CAF-specific clone, HTTIPKV (lane 3), from CAF revealed a unique band (boxed) that was not pulled-down by the M13Ke phage (control; lane 1). The boxed band was sent for MS/MS analysis. (B) A competitive assay of I-125-labeled HTTIPKV (I-TasPep) binding to CAF cells with and without the competition of recombinant hT2R9 protein. *p<0.05. (C) qPCR analysis of T2R9 transcriptional levels in wildtype (WT) and T2R9 siRNA lentivirus transduced CAFs. **p=0.0053, N = 4. (D) End-point qPCR samples from the above reactions were resolved on a 1.5% agarose gel and imaged for SYBR safe intensity. Gel represents reaction samples following T2R9 and 18s primer set amplification, respectively. NTC = no template control. (E) Western blot of CAF and T2R9(-) CAF whole cell lysates probed against T2R9 (Thermo). (F) qPCR analysis of T2R9 transcriptional levels in HDF and CAFs. ***p=0.009, N = 3. (G) IHC staining of T2R9 expression in human IPMN and PDAC pancreas. Arrows indicate stroma cells with strong T2R9 expression.

protein level, we performed anti-T2R9 immunoblotting on the WT CAFs and siT2R9 transduced CAFs. We evaluated 4 different sources of anti-T2R9 antibodies, and all highlighted a band at approximately 36 kDa corresponding to the correct molecular weight of T2R9. In lanes with samples from cells transduced with siT2R9, the T2R9 band had an average of 44.8% reduction in intensity (Figure 4.1E, Figure S4.3).

Finally, we compared T2R9 expression in normal and malignant fibroblasts and in patient samples from pancreatic cancer, intraductal papillary mucinous neoplasms (IPMN), and normal pancreas. Compared to human dermal fibroblasts (HDFs), T2R9 had a 57-fold higher mRNA expression in CAFs via qPCR (Figure 4.1F). Likewise, T2R9 expression is detected in the stroma of human IPMN and PDAC tissues (Figure 4.1G). Taken together, these data demonstrate that 1) T2R9 is the binding partner of a CAF-targeted phage, 2) T2R9 is upregulated in pancreatic CAFs compared to normal fibroblasts, and 3) strong T2R9 expression is present in the stroma of malignant pancreas, suggesting that T2R9 is a potential molecular target for therapeutic delivery in PDAC.

4.4.2 Liposomes functionalized with the HTTIPKV peptide demonstrate specificity to T2R9

Peptide-functionalized liposomes to allow targeted delivery of small molecular drugs have produced cancer therapies with superior pharmacodynamics and efficacy [26]–[28]. Based on the expression profile of T2R9 in PDAC stroma, we engineered a CAF targeted liposome through conjugation of HTTIPKV to PEG-lipid moieties present in the liposome (TTL, Schema Figure 4.2A). The peptide sequence HTTIPKVGGSK(fitc)C was conjugated to DSPE-PEG_{3400}-maleimide to form peptide-PEG_{3400}-DSPE (Figure 4.2A). Liposomes without surface modifications were prepared in parallel as a negative control (NC liposome). A non-exchangeable lipid dye, DiR, was incorporated into the lipid formula to allow particle tracking via imaging. All batches of TTL and NC liposomal formulations were of similar particle size (100-120 nm, Figure S4.4) and concentration ($2.4 \times 10^{12} - 3.2 \times 10^{12}$ particles/mL) as determined via NanoSight analysis (Figure 4.2B). The zeta potential of NC liposomes and TTL was -37.2 mV and -34.2 mV, respectively, indicating that the peptide did not alter the charge of the liposomes (Figure S4.5).

A

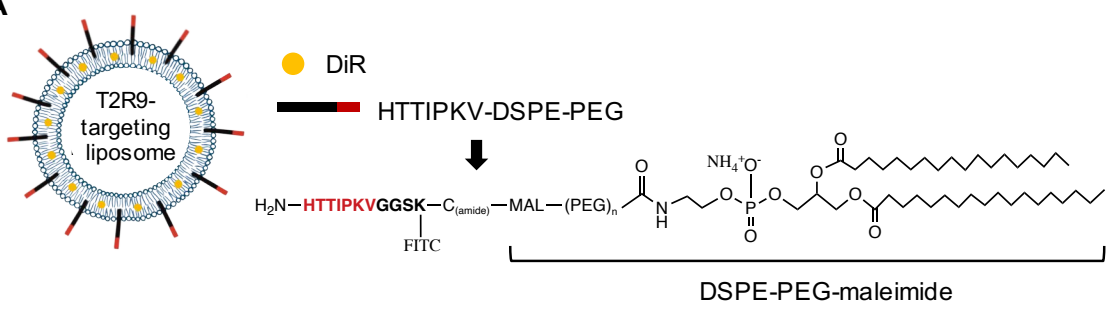

B

	Batch	1	2	3	4
TTL	Size (nm)	120.0 ± 0.9	102.9 ± 2.3	107.6 ± 1.4	106.2 ± 0.7
	Concentration (particles/mL)	2.6e12 ± 2.1e8	3.2e12 ± 7.5e8	2.7e12 ± 4.9e8	2.4e12 ± 1.0e8
NC	Size (nm)	119.5 ± 1.0	112.3 ± 0.8	102.5 ± 1.3	
	Concentration (particles/mL)	2.4e12 ± 4.5e8	2.5e12 ± 4.0e8	2.9e12 ± 5.12e8	

C

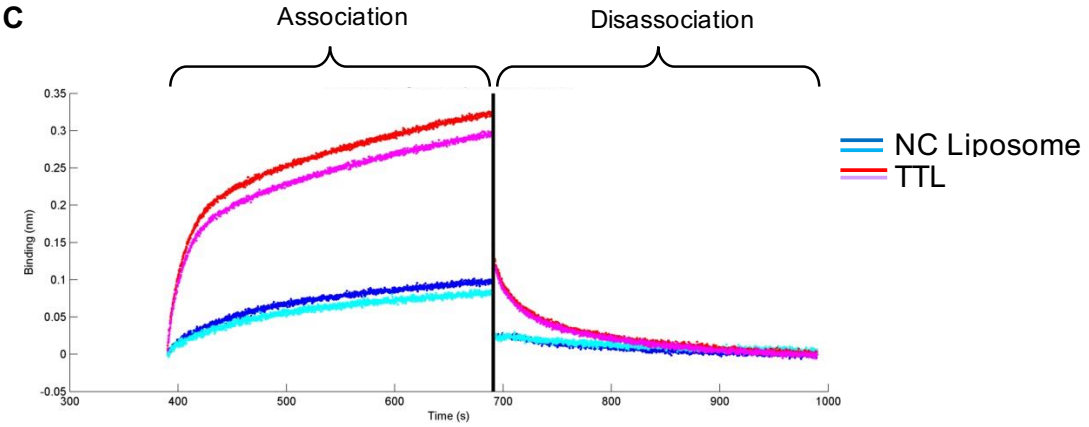

Figure 4.2. HTTIPKV-conjugated liposomes bind specific to T2R9. (A) Schematics of TTL. T2R9-targeting peptide (HTTIPKV) was conjugated to DSPE-PEG on DOPC liposomes. (B) Batch concentration and liposome size of TTL and NC liposomes. (C) A binding assay using ForteBio showed the association and dissociation curves of liposomes with (red and pink) or without (dark and light blue) the HTTIPKV peptide to recombinant T2R9 protein.

Peptide remained specific to T2R9 after incorporation into liposomes as assessed by binding assays using the ForteBio octet system. His-T2R9 was non-covalently bound to the biosensor and the biosensor exposed to 40mM of either NC liposomes or TTL. An association with T2R9 was observed at first 300 sec when exposed to TTL, followed by a complete disassociation between the protein and the liposome (Figure 4.2C). Such association curve was not seen when T2R9 exposed to the NC liposomes, suggesting the binding between TTL and T2R9 is not a result of lipid's non-specific binding. These data have confirmed the HTTIPKV peptide was displayed on liposomes in a correct orientation that the specificity to T2R9 has been preserved in TTL.

4.4.3 TTL enhances tumor uptakes in an admix PDAC model

To determine the targeting ability of TTL to PDAC stroma, we intravenously injected TTL and NC liposomes via tail vein in a subcutaneous xenograft admix PDAC mouse model containing both BXPC3 and CAF cells (BXPC3-to-CAF-ratio = 1:3) as previously described [15]. The ratio of CAF to cancer cells were chosen to reflect the dense stromal content in PDAC tumors in patients. Since the liposomes contained a non-exchangeable lipophilic dye (DiR), we could detect the location and the amount of particle accumulation non-invasively using fluorescent molecular tomography (FMT) imaging (Figure 4.3A). The amount of DiR in the tumor xenograft was quantified from the reconstructed images using the FMT system software (Figure 4.3B). We used a compartment model to fit our liposome time course data to calculate the accumulations in tumors based on the area under the curve (AUC). The total drug exposure to the tumor increased significantly as a 1.9-fold higher liposome accumulation was observed in animals injected with TTL compared to NC liposomes (Figure 4.3C; AUC 7.19 in NC liposomes vs. 13.89 in TTL). The peptides present on the liposomes did not alter particle accumulation (K_a) and elimination (K_e) rates in the admix tumor, indicating the increased accumulation of TTL is not a result of altered clearance due to surface modification (Figure 4.3C).

To test whether the increased tumor uptake of targeted liposomes was a result of CAF binding, we performed a colocalization analysis on admix tumor sections stained with α-SMA for CAFs and DiR for liposomes. Admix PDAC tumor-bearing mice were harvested 24 h post liposomal injection and stained for CAF expression. TTL showed a ~20-fold higher overlap with α-SMA-

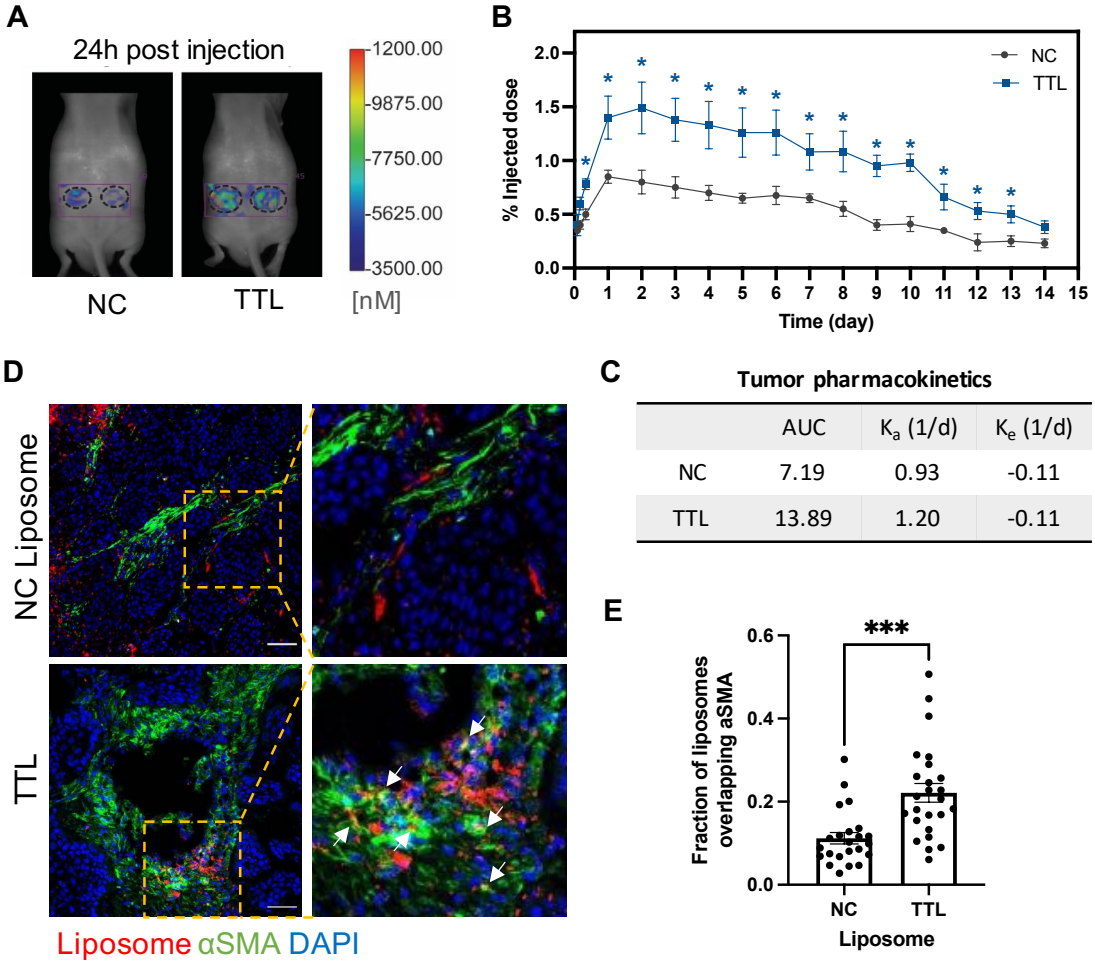

Figure. 4.3. In Vivo imaging of TTL. (A) FMT images of mice one-day post-injection. (B) Mice bearing subcutaneous admix CAF/BXPC3 tumors (n=10 tumors/group) were injected with dye-labeled liposomes and the tumor accumulation was measured on an FMT using a region-of-interest around the tumor area. Statistical significance was measured with a Student's t-test between TTL and NC liposomes. *p<0.05. (C) Tumor pharmacokinetics were determined by fitting the liposome time course data with compartment models by regression analysis in MATLAB. (D) Immunofluorescence images of tumor sections from mice injected with liposomes with and without HTTIPKV. Lipophilic dye shows the location of liposomes (red); cells stained to show nuclei (DAPI, blue) and α-SMA-positive cells (green). Arrows indicate co-localization. Scale bars, 50 µm. (E) Mander's colocalization analysis of injected liposomes overlapping with aSMA-positive cells in the admix tumor section at 24h post liposome inejction. N = 7~9 images/mouse, 3 mice/group. ***p = 0.0002.

positive cells than NC liposomes (Mander's correlation coefficient = 0.22 for TTL vs 0.045 for NC liposomes; p-value = 0.0002), indicating that liposomes accumulated primarily in CAFs (Figure 4.3D & E) and that the peptide was able to shift the cellular distribution of the liposomes. Compared to NC liposomes that are found ditributed throughout the tumor sections, incorporation of T2R9-targeting peptide presented a shift in the liposomal distribution favoring PDAC stroma (Figure 4.3D). Combining the tumor pharmacokinetics and the immunofluorescent results, we excluded the possibility of particle clearance in tumors being altered by liposome surface modifications and concluded that the addition of a T2R9-targeting peptide contributed to the enhanced liposome uptakes in the admix PDAC tumor models.

4.4.4 TTL liposomal delivery of CXCR2 inhibitors constrains tumor growth

Inhibiting the CXCL-CXCR2 axis with CXCR2 antagonists has been shown to inhibit tumor growth, extend survival, and induce anti-angiogenesis effects in tumor xenograft models [18, 19]. However, systemic CXCR2 inhibition increases the risk of developing neutropenia [21] and could present undesirable adverse effect in cancer patients with a compromised immune system. To evaluate whether our targeted liposomes may mitigate the off-target effects and improve therapeutic outcomes, we developed a liposomal encapsulated formulation of a CXCR2 inhibitor, SB225002, using the ethanol injection method. We compared tumor outgrowth in mice bearing subcutaneous admix BXPC3/CAF xenografts during 4 treatment regimens over a 19-days course: 1) untreated, 2) systemic SB225002 (0.5 mg/kg per intraperitoneal injection, 5x/week), 3) SB225002-loaded NC liposomes (0.83 mg/kg per intravenous injection, 3x/week), and 4) SB225002-loaded TTL (0.83 mg/kg per intravenous injection, 3x/week). The free SB225002 were administrated based on previously described optimal dosage and route [18]. The liposomal drug dosage was calculated for each injection to achieve the same total weekly drug administration for all groups.

Mice from all groups treated with SB225002 displayed significant growth inhibition compared to the untreated mice, with the greatest inhibition rate seen in the TTL-treated cohort (Figure 4.4A). We observed tumor ulceration in mice treated with NC liposomes on day 16 and had to euthanize the animal; no ulceration was observed in any of the other groups. Compared

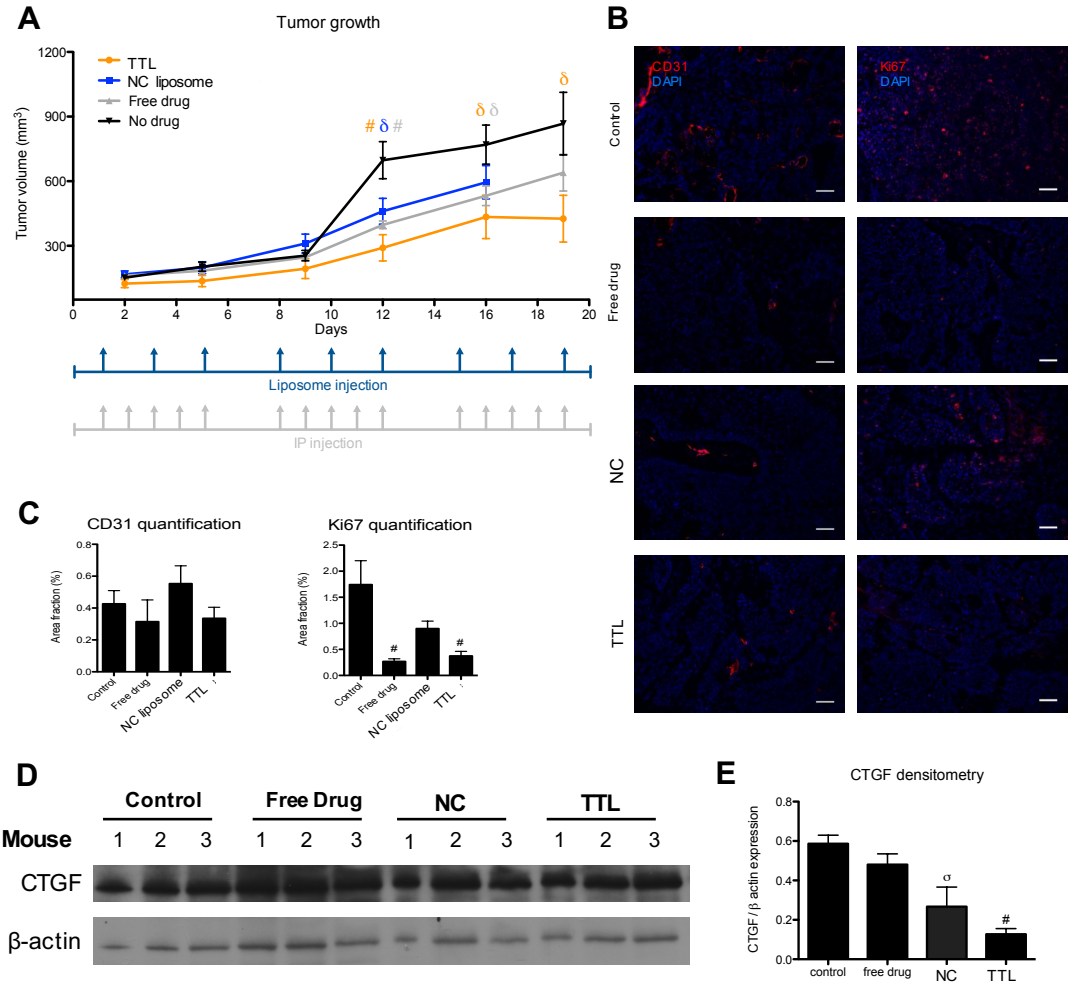

Figure 4.4. CXCR2 inhibition in admix BXPC3/CAF tumors following SB225002 delivery. (A) Mice bearing subcutaneous admix BXPC3/CAF tumors were injected with SB225002, NC liposomes loaded with SB225002, TTL loaded with SB225002, or no treatment. Tumor growth was measured via calipers for 19 days (n=10-12 tumors/group). Dosage schedules for liposomes and free drug (IP injections) are as indicated. Statistical significance was measured with a Student's t-test between liposomes with and without a peptide where #p<0.01, and δp<0.05. The NC liposome group was terminated early due to tumor ulceration. (B) Representative images of CD31 and Ki67 staining show the vessels and cell proliferation in different treatment groups. Scale bar, 50 µm. (C) Quantification of images using thresholding in ImageJ was averaged across five images of three sections of three tumors (45 images total per treatment group). #p<0.01 statistical significance with Student's t-test. (D) Western blot of homogenized tumor lysates from three mice per treatment group using anti-CTGF and anti-β-actin. (E) Densitometry of CTGF western blot. Adapted from [29].

to systemic delivery, SB225002 delivered by TTL resulted in a respective 1.6- and 1.25-fold smaller tumors on day 12 and 16 ($p < 0.05$), indicating an improved anti-tumor efficacy with CAF-targeted therapies. In contrast, there was no statistically significant difference between liposome and free drug treatments on day 19. At the end of treatment (day 19), the average tumor volume of mice receiving SB225002-loaded TTL was significantly smaller compared to the untreated mice (1.9-fold smaller, $p < 0.05$). The H&E staining of tumor sections revealed a similar tumor-to-stromal ratio from all groups, indicating the decrease in tumor volume was not merely a reflection of stromal depletion (Figure S4.6). These data demonstrated targeted delivery of SB225002 to PDAC stroma improved anti-tumor efficacy.

To further evaluate pharmacodynamics, we characterized downstream molecular effects of CXCR2 inhibition. CXC chemokines (CXCL) interact with CXCR2 and induce CTGF expression in CAFs, which consequently induce tumor growth [18]. Thus, a decrease in CTGF expression can be utilized as an indicator for the interruption of the CXCL-CXCR2 axis by SB225002. Tumors from all groups were homogenized for Western blot analysis using anti-CTGF and anti-β-actin (a loading control). Quantification via densitometry revealed a 4-fold lower CTGF expression in TTL treated animals compared to the untreated mice ($p<0.05$, Figure 4.4D & E). In contrast, NC treated animals showed only a 1-fold decrease in CTGF expression. These data suggested an effective delivery of SB225002 by TTL. Ijichi et al. showed inhibition of angiogenesis contributed to the overall anti-tumor effect of SB225002 [18]. We, however, did not observe significant difference in CD31+ areas between 4 treatment groups (Figure 4.4B &C). Next, we examined SB225002's effects on cell proliferation through Ki67 staining on the tumor sections. Quantification of Ki67 positive areas by ImageJ revealed a significant reduction in Ki67+ area fraction in mice treated with free drug and targeted liposomes but no significance was observed when given the NC liposomes ($p<0.01$, Figure 4.4B & C). Taken together, these results demonstrate that TTL-mediated delivery of SB225002 to PDAC stroma results in more effective anti-tumor outcomes than free drug and NC liposome delivery.

4.5 Discussion

We have identified a novel target of CAF cells, T2R9. T2R9 is a member of the bitter taste receptor family that is expressed in healthy tissues of the palate and oral cavity [29]. Here, we reveal for the first time, the presence of T2R9 in CAFs from PDAC patients and demonstrate the ability to therapeutically target stroma through T2R9. CAF cells represent a compelling target as they are the most abundant cellular components in the PDAC TME with an estimated 10-100 times more adjacent CAFs for every tumor epithelial cell. Additionally, the relative genetic stability of CAF compared to cancer cells, which possess various genetic profiles at distinct stages, makes CAF more amenable to treatment than cancer epithelial cells. Common cell markers used to detect CAFs are alpha-SMA, S100A4, FAP, PDGFR-alpha/beta, tenascin-C, NGS, desman, CD90/THY1, and PDPN [31]. However, none of these markers are exclusively expressed by CAFs and can also be found in other cell types, such as in vascular muscle cells and pericytes (alpha-SMA), fibroblasts (S100A4), and CD45+ cells (FAP) [31–33]. The lack of selectivity to distinguish CAFs from normal cells limits their clinical use as molecular targets in targeted therapy. Our discoveries addressed this deficiency through identifying a CAF-specific ligand (HTTIPKV) and its binding partner, T2R9, from the stroma of patients with PDAC. From cell binding assays, we demonstrated a 1.9- and 1.5-fold higher binding of HTTIPKV-phage to CAF than to a normal fibroblast (MRC5) and a PDAC-derived cell line (BXPC3), respectively [15]. Liposomes decorated with CAF-specific ligands demonstrated 1.9-fold higher tumor accumulations than NC liposomes. Importantly, the targeted liposomes were found either co-localized or adjacent to aSMA+ cells, whereas NC liposomes present non-specifically. Taken together, these results suggest T2R9 is a potential molecular target of pancreatic stroma. Further experimentation will be needed to investigate the stromal cell subtypes that express T2R9 and their associated biological functions.

Several papers have reported the expressions of bitter taste receptors in pancreatic cancer. Gaida et al. found T2R38 localized with lipid droplets in pancreas-derived cancer cells and activation of T2R38 upregulated MAP kinases and a multidrug-resistance protein ABCB1 [35]. Stern et al. identified T2R10 expression in epithelial cells of human PDAC tissue (79% cancer samples) and PDAC derived cell lines, and demonstrated a T2R10-dependent signaling pathway that regulates ABCG2, a transmembrane drug-effluent pump that help cells develop

chemoresistance [36]. Furthermore, a recent study indicated the significance of the gustatory signaling in metaplastic tuft cells to suppress PDAC progression in the CXCL1/2-CXCR2 axis dependent manner [37]. These data suggest the functional role of bitter receptors in chemoresistance and immunosuppression in pancreatic cancer. Consistent with previous findings of upregulated bitter receptor members in PDAC, our results revealed overexpression of T2R9 in the pancreatic CAF by 57-fold. Anti-T2R9 immunostaining showed T2R9 expression in the stroma of IPMN and PDAC. Future studies will be needed to evaluate the functional role of T2R9 in PDAC.

To evaluate the anti-tumor effects of targeted delivered CXCR2 antagonist to CAF, we measured tumor growth over a 19 days treatment course and characterized the downstream molecular response of the CXCLs-CXCR2 axis in an admix xenograft mouse model. SB225002 is a small molecule CXCR2 inhibitor that has been shown to profoundly prolonged survival in the KPC mice [19]. Using this small molecule drug to test our targeting platform, we significantly inhibited tumor growth in mice treated with drugs in targeted liposomes compared to systemic delivery. Successful delivery of SB225002 to interfere with CXCLs-CXCR2 response was confirmed with the reduced expression of its downstream product, CTGF, amongst all treatment groups. Treating with CAF-targeted liposome, in particular, induced optimal CXCR2 suppression, which resulted in tumor growth inhibition and reduced cell proliferation. We, however, did not observe differences in tumor angiogenesis between treated and untreated mice that was previously reported in a rat corneal micropocket model of PDAC [20]. One potential explanation is that there exist multiple tumor angiogenesis signaling pathways regulated by CAFs, and down-regulating the CXCLs-CXCR2 axis alone may cause changes in alternate, compensatory pathways [38]. Taken together, the CAF-targeted liposome improved the pharmacodynamic response in inducing anti-tumor effects.

In conclusion, we have identified a bitter receptor overexpressed in pancreatic CAFs and demonstrated the feasibility of using T2R9 as a molecular target to achieve stromal-targeting therapy. The anti-tumoral outcomes induced by targeted delivery of CXCR2 inhibitors offer the potential to reprogram CAF-cancer cell communications in PDAC.

4.6 Acknowledgements

The work was supported by NIH (R21 CA231196-01, R01 CA233716-01 A1) and NCI (P30 CA044579-26).

4.7 Author contributions

Conceptualization (JH, LTB, KAK), data curation (JH, SSKD, JD, HCC, LTB), formal analysis (JH, SSKD, JD, HCC, LTB), investigation (JH, SSKD, JD, HCC, LTB, KAK), methodology (JH, SSKD, JD, HCC, LTB, KAK), project administration (LTB, KAK), supervision (LTB, KAK), visualization (JH, LTB), writing – original draft (JH, LTB), and writing – review & editing (JH, LTB, KAK).

4.8 Declaration of Interests

The authors declare that Dr. Kelly is the CEO and Founder of ZielBio, Inc. JD and LTB are employees of ZielBio. ZielBio played no role in funding this work. JH, and SSKD declare no conflicts of interest in this work.

4.9 Reference

[1] W. Street, “Cancer Facts & Figures 2020,” p. 76, 2020.

[2] A. A. Mohammad, “Advanced pancreatic cancer: The standard of care and new opportunities,” *Oncol. Rev.*, vol. 12, no. 2, Sep. 2018, doi: 10.4081/oncol.2018.370.

[3] R. K. Ramanathan *et al.*, “A phase IB/II randomized study of mFOLFIRINOX (mFFOX) + pegylated recombinant human hyaluronidase (PEGPH20) versus mFFOX alone in patients with good performance status metastatic pancreatic adenocarcinoma (mPC): SWOG S1313 (NCT #01959139).,” *J. Clin. Oncol.*, vol. 36, no. 4_suppl, pp. 208–208, Feb. 2018, doi: 10.1200/JCO.2018.36.4_suppl.208.

[4] “Infinity Reports Update from Phase 2 Study of Saridegib Plus Gemcitabine in Patients with Metastatic Pancreatic Cancer,” Jan. 27, 2012. https://www.businesswire.com/news/home/20120127005146/en/Infinity-Reports-Update-from-Phase-2-Study-of-Saridegib-Plus-Gemcitabine-in-Patients-with-Metastatic-Pancreatic-Cancer (accessed Feb. 21, 2021).

[5] R. Kalluri, “The biology and function of fibroblasts in cancer,” *Nat. Rev. Cancer*, vol. 16, no. 9, Art. no. 9, Sep. 2016, doi: 10.1038/nrc.2016.73.

[6] L. Bolm *et al.*, “The Role of Fibroblasts in Pancreatic Cancer: Extracellular Matrix Versus Paracrine Factors,” *Transl. Oncol.*, vol. 10, no. 4, pp. 578–588, Aug. 2017, doi: 10.1016/j.tranon.2017.04.009.

[7] S. Su *et al.*, “CD10+GPR77+ Cancer-Associated Fibroblasts Promote Cancer Formation and Chemoresistance by Sustaining Cancer Stemness,” *Cell*, vol. 172, no. 4, pp. 841-856.e16, Feb. 2018, doi: 10.1016/j.cell.2018.01.009.

[8] J. Leca *et al.*, “Cancer-associated fibroblast-derived annexin A6+ extracellular vesicles support pancreatic cancer aggressiveness,” *J. Clin. Invest.*, vol. 126, no. 11, pp. 4140–4156, Nov. 2016, doi: 10.1172/JCI87734.

[9] L. Monteran and N. Erez, “The Dark Side of Fibroblasts: Cancer-Associated Fibroblasts as Mediators of Immunosuppression in the Tumor Microenvironment,” *Front. Immunol.*, vol. 10, Aug. 2019, doi: 10.3389/fimmu.2019.01835.

[10] Q. Sun *et al.*, “The impact of cancer-associated fibroblasts on major hallmarks of pancreatic cancer,” *Theranostics*, vol. 8, no. 18, pp. 5072–5087, Oct. 2018, doi: 10.7150/thno.26546.

[11] B. C. Özdemir *et al.*, “Depletion of carcinoma-associated fibroblasts and fibrosis induces immunosuppression and accelerates pancreas cancer with reduced survival,” *Cancer Cell*, vol. 25, no. 6, pp. 719–734, Jun. 2014, doi: 10.1016/j.ccr.2014.04.005.

[12] A. D. Rhim *et al.*, “Stromal elements act to restrain, rather than support, pancreatic ductal adenocarcinoma,” *Cancer Cell*, vol. 25, no. 6, pp. 735–747, Jun. 2014, doi: 10.1016/j.ccr.2014.04.021.

[13] M. Sano *et al.*, “Blocking CXCLs-CXCR2 axis in tumor-stromal interactions contributes to survival in a mouse model of pancreatic ductal adenocarcinoma through reduced cell invasion/migration and a shift of immune-inflammatory microenvironment,” *Oncogenesis*, vol. 8, no. 2, p. 8, Jan. 2019, doi: 10.1038/s41389-018-0117-8.

[14] G. Biffi *et al.*, “IL1-Induced JAK/STAT Signaling Is Antagonized by TGFβ to Shape CAF Heterogeneity in Pancreatic Ductal Adenocarcinoma,” *Cancer Discov.*, vol. 9, no. 2, pp. 282–301, Feb. 2019, doi: 10.1158/2159-8290.CD-18-0710.

[15] L. T. Brinton, D. K. Bauknight, S. S. K. Dasa, and K. A. Kelly, “PHASTpep: Analysis Software for Discovery of Cell-Selective Peptides via Phage Display and Next-Generation Sequencing,” *PLOS ONE*, vol. 11, no. 5, p. e0155244, May 2016, doi: 10.1371/journal.pone.0155244.

[16] M. R. Howitt *et al.*, “Tuft cells, taste-chemosensory cells, orchestrate parasite type 2 immunity in the gut,” *Science*, vol. 351, no. 6279, pp. 1329–1333, Mar. 2016, doi: 10.1126/science.aaf1648.

[17] D. A. Deshpande *et al.*, “Bitter taste receptors on airway smooth muscle bronchodilate by localized calcium signaling and reverse obstruction,” *Nat. Med.*, vol. 16, no. 11, Art. no. 11, Nov. 2010, doi: 10.1038/nm.2237.

[18] H. Ijichi *et al.*, “Inhibiting Cxcr2 disrupts tumor-stromal interactions and improves survival in a mouse model of pancreatic ductal adenocarcinoma,” *J. Clin. Invest.*, vol. 121, no. 10, pp. 4106–4117, Oct. 2011, doi: 10.1172/JCI42754.

[19] C. W. Steele *et al.*, “CXCR2 Inhibition Profoundly Suppresses Metastases and Augments Immunotherapy in Pancreatic Ductal Adenocarcinoma,” *Cancer Cell*, vol. 29, no. 6, pp. 832–845, Jun. 2016, doi: 10.1016/j.ccell.2016.04.014.

[20] M. N. Wente *et al.*, “Blockade of the chemokine receptor CXCR2 inhibits pancreatic cancer cell-induced angiogenesis,” *Cancer Lett.*, vol. 241, no. 2, pp. 221–227, Sep. 2006, doi: 10.1016/j.canlet.2005.10.041.

[21] L. M. Campbell, P. J. Maxwell, and D. J. J. Waugh, “Rationale and Means to Target Pro-Inflammatory Interleukin-8 (CXCL8) Signaling in Cancer,” *Pharmaceuticals*, vol. 6, no. 8, Art. no. 8, Aug. 2013, doi: 10.3390/ph6080929.

[22] F. Reynolds *et al.*, “A Functional Proteomic Method for Biomarker Discovery,” *PLOS ONE*, vol. 6, no. 7, p. e22471, Jul. 2011, doi: 10.1371/journal.pone.0022471.

[23] M. Zollo and E. Y. Chen, “A manual high-throughput M13 DNA preparation,” *BioTechniques*, vol. 16, no. 3, pp. 370–372, Mar. 1994.

[24] R. Hunter, “Standardization of the chloramine-T method of protein iodination,” *Proc. Soc. Exp. Biol. Med. Soc. Exp. Biol. Med. N. Y. N*, vol. 133, no. 3, pp. 989–992, Mar. 1970, doi: 10.3181/00379727-133-34611.

[25] A. Wagner, K. Vorauer-Uhl, and H. Katinger, “Liposomes produced in a pilot scale: production, purification and efficiency aspects,” *Eur. J. Pharm. Biopharm. Off. J. Arbeitsgemeinschaft Pharm. Verfahrenstechnik EV*, vol. 54, no. 2, pp. 213–219, Sep. 2002, doi: 10.1016/s0939-6411(02)00062-0.

[26] K. He and M. Tang, “Safety of novel liposomal drugs for cancer treatment: Advances and prospects,” *Chem. Biol. Interact.*, vol. 295, pp. 13–19, Nov. 2018, doi: 10.1016/j.cbi.2017.09.006.

[27] M. R. Aronson, S. H. Medina, and M. J. Mitchell, “Peptide functionalized liposomes for receptor targeted cancer therapy,” *APL Bioeng.*, vol. 5, no. 1, p. 011501, Jan. 2021, doi: 10.1063/5.0029860.

[28] L. Belfiore, D. N. Saunders, M. Ranson, K. J. Thurecht, G. Storm, and K. L. Vine, “Towards clinical translation of ligand-functionalized liposomes in targeted cancer therapy: Challenges and opportunities,” *J. Controlled Release*, vol. 277, pp. 1–13, May 2018, doi: 10.1016/j.jconrel.2018.02.040.

[29] L. Brinton and K. (advisor) Kelly, “Stromal Disruption of Pancreatic Adenocarcinoma Using Liposomes Targeted to Cancer-Associated Fibroblasts,” University of Virginia, Biomedical Engineering - School of Engineering and Applied Science, PHD (Doctor of Philosophy), 2016, Charlottesville, VA, 2016. Accessed: Jun. 09, 2021. [Online]. Available: https://doi.org/10.18130/V3N299

[30] “TAS2R9 protein expression summary - The Human Protein Atlas.” https://www.proteinatlas.org/ENSG00000121381-TAS2R9 (accessed May 20, 2021).

[31] T. Liu *et al.*, “Cancer-associated fibroblasts: an emerging target of anti-cancer immunotherapy,” *J. Hematol. Oncol.J Hematol Oncol*, vol. 12, no. 1, p. 86, Aug. 2019, doi: 10.1186/s13045-019-0770-1.

[32] J. Zhang, L. Chen, X. Liu, T. Kammertoens, T. Blankenstein, and Z. Qin, “Fibroblast-Specific Protein 1/S100A4–Positive Cells Prevent Carcinoma through Collagen Production and Encapsulation of Carcinogens,” *Cancer Res.*, vol. 73, no. 9, pp. 2770–2781, May 2013, doi: 10.1158/0008-5472.CAN-12-3022.

[33] D. Öhlund *et al.*, “Distinct populations of inflammatory fibroblasts and myofibroblasts in pancreatic cancer,” *J. Exp. Med.*, vol. 214, no. 3, pp. 579–596, Mar. 2017, doi: 10.1084/jem.20162024.

[34] J. N. Arnold, L. Magiera, M. Kraman, and D. T. Fearon, “Tumoral Immune Suppression by Macrophages Expressing Fibroblast Activation Protein-Alpha and Heme Oxygenase-1,”

Cancer Immunol. Res., vol. 2, no. 2, pp. 121–126, Feb. 2014, doi: 10.1158/2326-6066.CIR-13-0150.

[35] M. M. Gaida *et al.*, "Expression of the bitter receptor T2R38 in pancreatic cancer: localization in lipid droplets and activation by a bacteria-derived quorum-sensing molecule," *Oncotarget*, vol. 7, no. 11, pp. 12623–12632, Mar. 2016, doi: 10.18632/oncotarget.7206.

[36] L. Stern *et al.*, "Overcoming chemoresistance in pancreatic cancer cells: role of the bitter taste receptor T2R10," *J. Cancer*, vol. 9, no. 4, pp. 711–725, 2018, doi: 10.7150/jca.21803.

[37] M. T. Hoffman *et al.*, "The Gustatory Sensory G-Protein GNAT3 Suppresses Pancreatic Cancer Progression in Mice," *Cell. Mol. Gastroenterol. Hepatol.*, vol. 11, no. 2, pp. 349–369, 2021, doi: 10.1016/j.jcmgh.2020.08.011.

[38] F.-T. Wang, W. Sun, J.-T. Zhang, and Y.-Z. Fan, "Cancer-associated fibroblast regulation of tumor neo-angiogenesis as a therapeutic target in cancer," *Oncol. Lett.*, vol. 17, no. 3, pp. 3055–3065, Mar. 2019, doi: 10.3892/ol.2019.9973.

4.10 Supplements

Figure S4.1. HTTIPKV phage pulldown. (A) Sequences of the 2 identified peptides following MS/MS analysis of the gel band derived from the HTTIPKV phage pulldown assay. Sequences (highlighted) were overlaid on the amino acid sequence of human taste 2 receptor member 9. The percent coverage (MS/MS peptides/T2R9 amino acid sequence is 12%. (B) The spectra for each of the 2 identified peptides.

A

Valid	Weight	Sequence	Prob	SEQUEST XCorr	SEQUEST deltaCn	NTT
☑	1.0	(R)DISLIDIILISLAISR(I)	97%	0.95	0.73	2
☑	1.0	(K)VMLAILLGSFLISLIISVPK(N)	83%	0.46	0.90	2

Q9NYW1 (100%), 35,614.1 Da
Taste receptor type 2 member 9 OS=Homo sapiens GN=TAS2R9 PE=1 SV=1
2 exclusive unique peptides, 2 exclusive unique spectra, 2 total spectra, 36/312 amino acids (12% coverage)

```
MPSAIEAIYI  ILIAGELTIG  IWGNGFIVLV  NCIDWLKRRD  ISLIDIILIS  LAISRICLLC  VISLDGFFML  LFPGTYGNSV
LVSIVNVVWT  FANNSSLWFT  SCLSIFYLLK  IANISHPFFF  WLKLKINKVM  LAILLGSFLI  SLIISVPKND  DMWYHLFKVS
HEENITWKFK  VSKIPGTFKQ  LTLNLGVMVP  FILCLISFFL  LLFSLVRHTK  QIRLHATGFR  DPSTEAHMRA  IKAVIIFLLL
LIVYYPVFLV  MTSSALIPQG  KLVLMIGDIV  TVIFPSSHSF  ILIMGNSKLR  EAFLKMLRFV  KCFLRRRKPF  VP
```

B

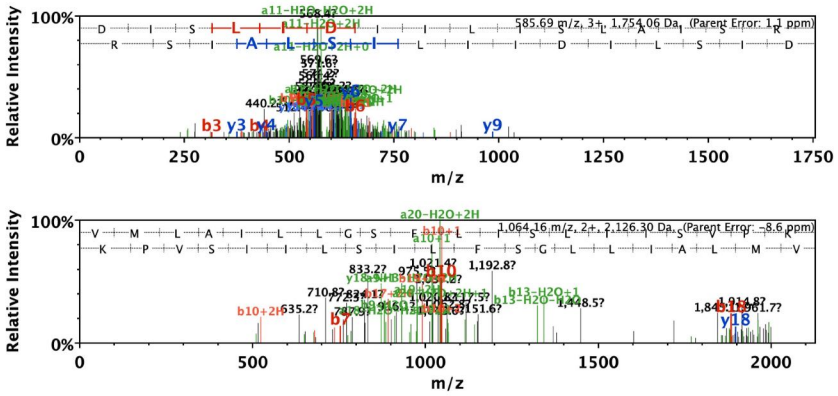

Figure S4.2. Generation of T2R9 knockdown CAF cell lines. CAF cells were transduced with T2R9 shRNA lentivirus at MOI of 10 (A), 2 (B), and vehicle control (C). (D) T2R9 shRNA lentivirus transduced CAF was selected based on the GFP expression using Aria Cell Sorter. (E) The GFP expression in Tasr9 (-) CAF remains intact in the sorted KO CAFs and after brought-up from frozen vials. 10x. (F) Immunoblot detection of T2R9 expression in the WT and KO CAFs. β-actin serves as a loading control. (G) Densitometry of the T2R9 WB image, N = 2.

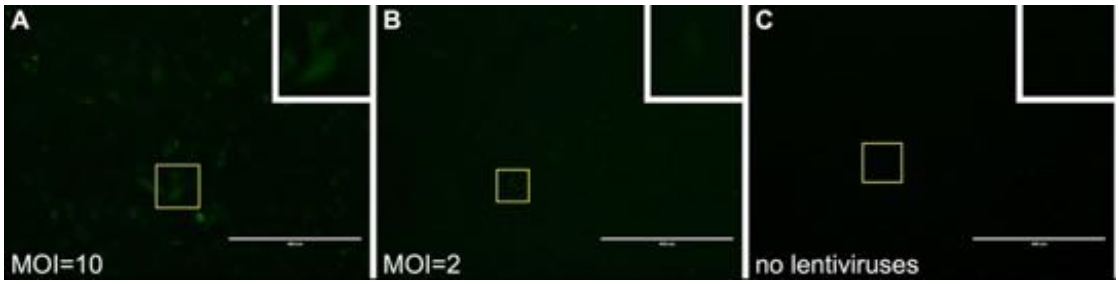

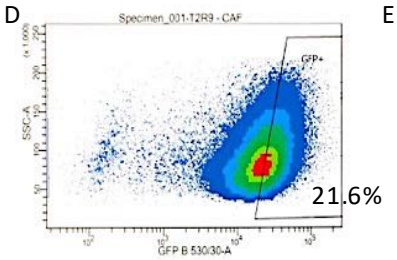

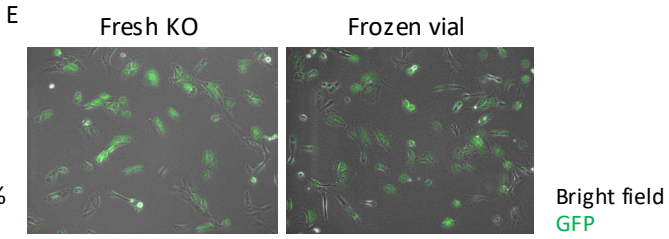

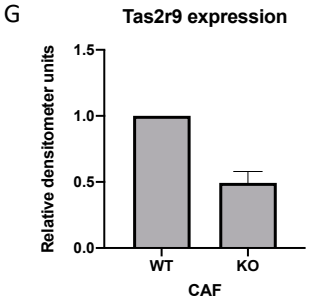

Figure S4.3. Antibody evaluation for T2R9 detected by WB. (A) Immunoblot of T2R9 antibodies from Thermo Fisher (Thermo), Bioss, Abcam, and Novus Biologicals (NovBio) for detection of crude and deglycosylated CAF lysates. CAF lysates were deglycosylated with PNGase F to remove N-linked oligosaccharides from the glycoproteins. β-actin serves as a loading control. (B) Densitometry of the T2R9 WB image in the boxed region (36kDa). (C) Degree of T2R9 knockdown detected by WB using 4 antibodies. (D) Summary table of T2R9 antibody used in all conducted experiments.

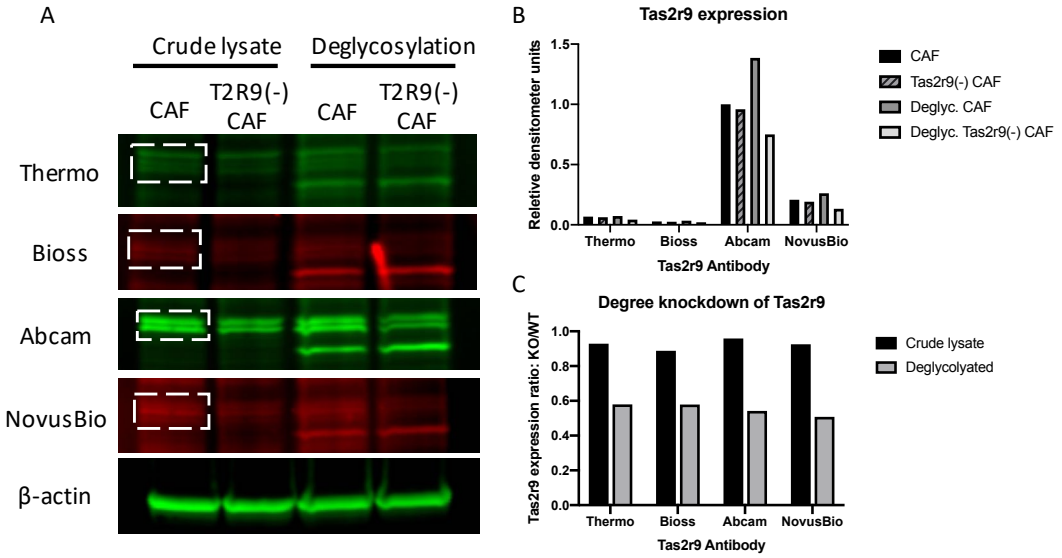

D

Source	Host/ clonality	Reactivity	Epitope	Experiments (dilutions)
Thermo Fisher OSR00157W	Rabbit/ polyclonal	Human	region 200-250 (intracellular)	IHC (1:1000)
Thermo Fisher PA5-67753	Rabbit/ polyclonal	Rat Human Mouse	region 141-160 (extracellular)	WB (1:1000)
NovusBio NB110-74894	Rabbit/ polyclonal	Human	region 200-250 (intracellular)	WB (1:1000)
Abcam Ab172932	Rabbit/ polyclonal	Human	region 153-180 (extracellular)	WB (1:1000)
Bioss Antibodies bs-11613R	Rabbit/ polyclonal	Human	region 166-179 (extracellular)	IF (1:100), WB (1:1000) Competitive ELISA

Figure S4.4. Liposome size distribution determined by NanoSight. (A) TTL batch #1-4. (B) NC liposomes batch #1-3. Adapted from [29].

A. TTL

Batch #1

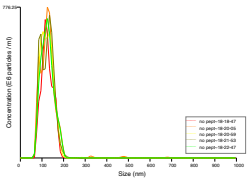

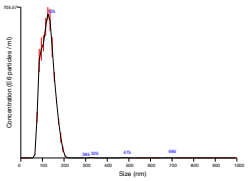

Batch #2

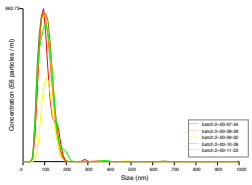

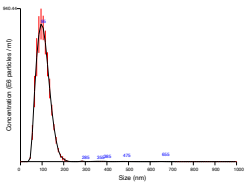

Batch #3

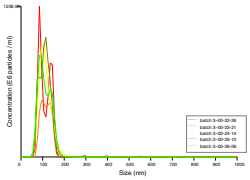

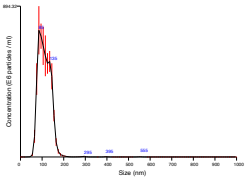

Batch #4

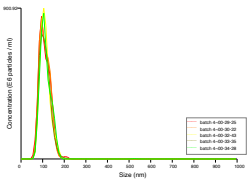

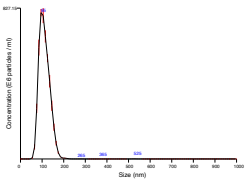

B. NC liposomes

Batch #1

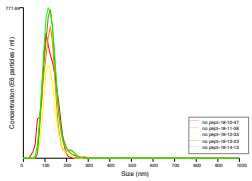

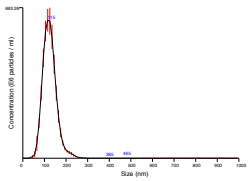

Batch #2

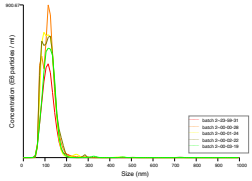

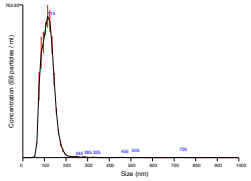

Batch #3

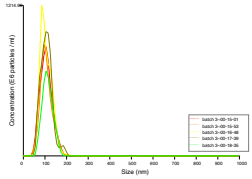

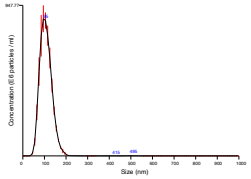

Figure S4.5. Liposome zeta-potential determined by Zetasizer. (A) NC (no peptide) liposome. (B) TTL (HTTIPKV liposome).

A

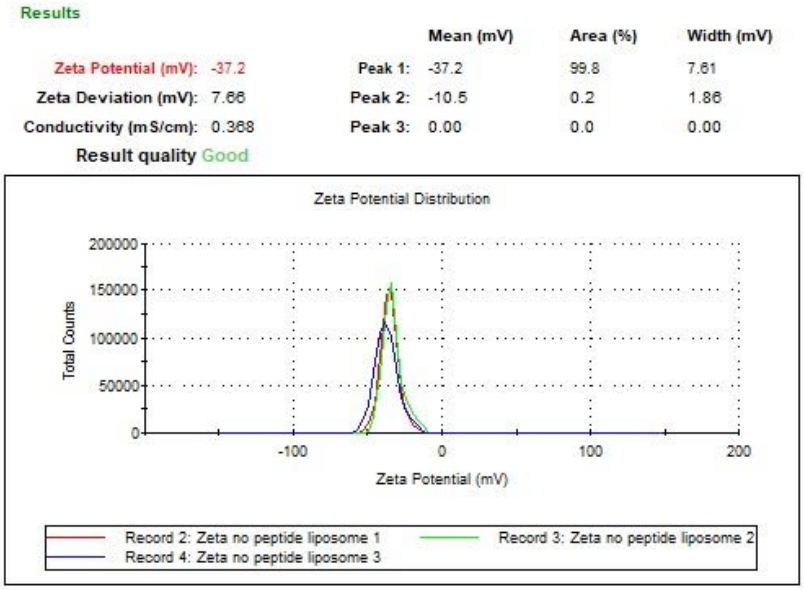

B

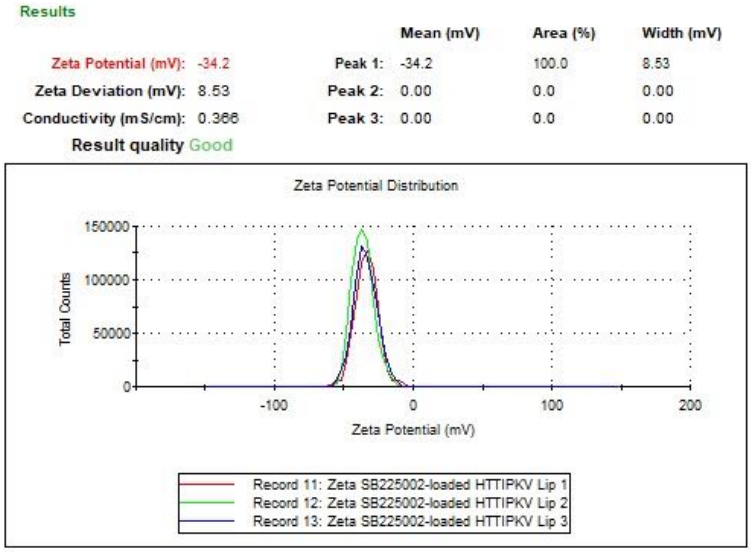

Figure S4.6. H&E staining of admix BXPC3/CAF tumors given (A) no treatment, (B) systemic SB225002, (C) SB225002-loaded NC liposomes, and (D) SB225002-loaded TTL. Scale bars, 50 µm. S, stroma; T, tumor. Adapted from [29].

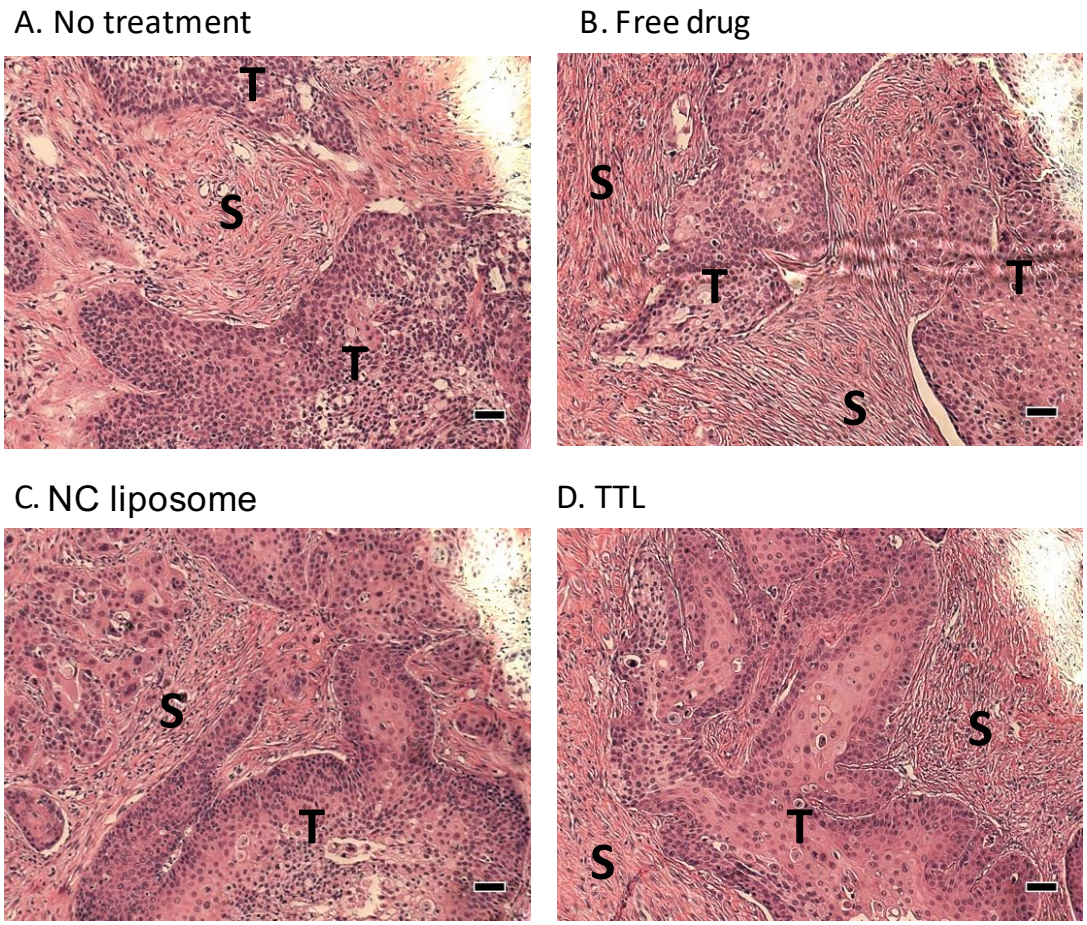

Chapter 5. Contributions and Future Directions

5.1 Recap of prior chapters

In this dissertation, we utilized computational-guided phage display to advance the identification of targeting moieties and their molecular targets in pancreatic diseases. In chapter 1, we reviewed the history of ligand identification technologies and how targeting ligands fit into advancing precision medicine for complex diseases. Despite the rapid development of proteomics approaches, there is yet a high-throughput method to allow an unbiased comparison of targeting moieties between different pancreatic disorders and to query proteins in their native context. To address this limitation, in chapter 2 of this dissertation, we developed a pipeline, Quantitative Selection of Available Targets (QSAT), to guide ligand selection in databases generated from in vivo phage display screening in the mouse model of chronic pancreatitis (CP). In chapter 3, the cellular selectivity of the CP-targeted peptides was confirmed, and the selected ligands were further developed into targeted liposomes for antifibrotic therapy in CP. In chapter 4, we leveraged phage display beyond ligand screening and identified a G-protein coupled receptor, taste receptor 2 member 9 (T2R9), as a novel molecular target for cancer-associated fibroblasts (CAFs) of pancreatic cancer and demonstrated the therapeutic potential of targeting T2R9 to improve small molecular drug delivery efficiency and efficacy. Collectively, Chapter 2-4 of this dissertation emphasize the scientific findings of ligand discovery in pancreatic disorders; here, we focus on the broader impacts of those findings and how they can be built upon to shape future research endeavors.

5.2 Contributions

5.2.1 A fulsome in silico prediction of disease-specific ligands for the inflamed and malignant pancreas

In chapter 2, we have developed a methodology to facilitate selection of ideal targeting ligands for deep-sequenced, in vivo phage display screens. Our in silico analysis addresses phage amplification bias and library-induced variabilities through normalization algorithm, isolates consistently enriched sequences based on the growth rate of the frequency counts, and identifies homologous motifs using a clustering algorithm. This quantitative approach increases predictive power and rigorousness in selecting candidate peptides and allows comparisons across different

species, cell lines, and diseased models. In fact, utilizing our developed method, we have analyzed and compiled pancreas-related screens from the lab's historical database to form a fulsome prediction of peptide signature for pancreas disease (Figure 5.1). In this analysis, we included three normal (HUVEC, N = 2; human-derived pancreatic stellate cell, PSC, N = 1; murine pancreas, N = 9), one inflamed (murine CP pancreas, N = 9), and three malignant (BXPC3, N = 2; patient-derived CAF, N = 6; tumor-conditioned media cultured HUVEC, N = 2) conditions. To our knowledge, this is the first to profile targeting moieties for multiple diseased conditions of the pancreas. The capability to exclude non-disease-specific ligands in silico will reduce the amount of time for validating false-positive ligands and overcome the common limitation of low specificity seen in current biomarkers (e.g., CA19-9 [1]), thus increasing clinical translatability.

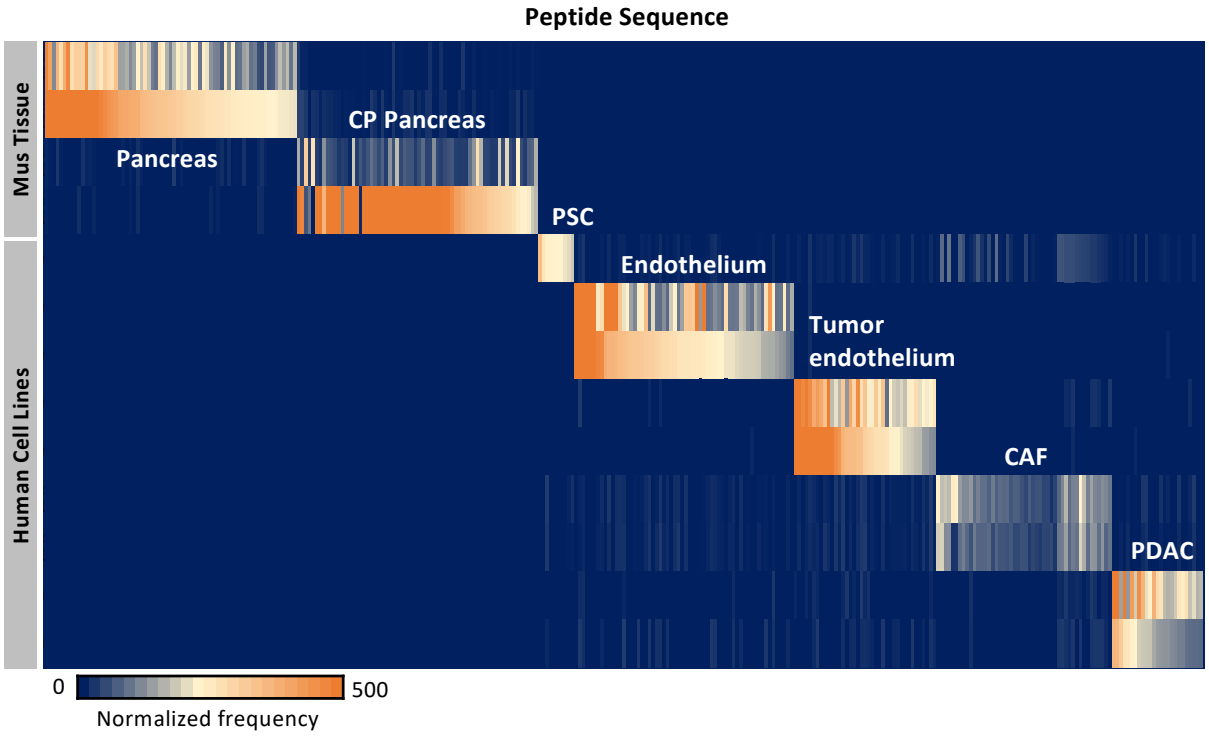

Figure 5.1 Summary matrix of peptide signatures of various diseased conditions in the pancreas. 319 peptides identified from screens performed on cell lines and *in vivo* screens were processed and analyzed using QSAT. CAF, cancer-associated fibroblast. PDAC, pancreatic ductal adenocarcinoma.

Additionally, the breakdown of targets in the database provides insight into the target of each peptide and could benefit broader areas of pancreatic research from engineering targeted drug delivery to molecular imaging agents and allow a deeper understanding of disease through exploration of the importance of the target itself to the disease.

5.2.2 Targeting moieties identification and targeted therapy development for chronic pancreatitis

Current treatments for CP are limited to palliative care and pain alleviation, and unlike in other diseases, no molecular targeting ligands or non-serum-based biomarkers are available, hindering the development of target-specific interventions [2]. In chapter 2 and 3, we have identified 5 peptide ligands (MDLSLKP, MNSIAIP, KTYVPTT, SNSQDLH, SLTNSSF) specific to CP and showed cellular selectivity to extracellular matrix, acinar cells, activated pancreatic stellate cells, and macrophages, respectively. From in silico comparison, we demonstrated that these ligands enriched only in phage screens performed in the inflamed pancreas but not in the healthy pancreas or PDAC-related cell lines. Validated using imaging modalities, the identified ligands showed a 2.5-to-3.1-fold higher accumulation in CP over healthy mice and 52~83% colocalization with the target cells in the inflamed pancreas. An automated ImageJ-based procedure was developed to allow rapid colocalization analysis. The ImageJ macro and R code are made available in the Appendix.

Liposome-based drug delivery systems are obtaining FDA approval and showing promising features, including enhanced drug bioavailability, prolonged circulation half-life, and improved patient outcomes through increasing the efficacy to toxicity ratio of the small molecule drugs encapsulated [3]. In chapter 3, we demonstrated an effective CP-targeted liposome via surface modification with one of the identified targeting ligands (MDLSLKP). The incorporation of targeted peptides was shown to increase the accumulation of liposomes in the CP pancreas 1.3-fold over non-targeted nanoparticles. The biodistribution study revealed a reduced particle accumulation in liver and kidneys, suggesting the CP-targeted liposomes have potential in overcoming drug toxicity issues in liver. Indeed, mice treated with the targeted formulation showed reduced ALT and oxidative stress in liver compared to the non-targeted liposomes. The

capability of using targeted liposomes to effectively delivery apigenin to the inflamed pancreas was demonstrated by a 37.2% and 33.1% respective reduction in collagen and fibronectin expression compared to systemic administration. These results have paved the way for new therapeutic strategies for CP.

5.2.3 Reveal a new molecular target, T2R9, for pancreatic ductal adenocarcinoma (PDAC)

In chapter 4, we used phage display-based functional proteomics to discover a novel CAF target, T2R9 [4]. The expression of T2R9 was confirmed by qPCR, WB, and IF to be upregulated in CAF isolated from PDAC patients when compared with healthy human dermal fibroblasts. Elevated T2R9 expression is also detected in the stroma of patient tumor samples derived from PDAC and IPMN. T2R9 belongs to a 25-member bitter taste family (T2R) with homology to 7 transmembrane GPCR. While other members of T2Rs have been detected in the airway epithelium or the gastrointestinal tract [5, 6], T2R9 expression in normal cells, to our knowledge, is restricted only to the oral cavity [7]. This makes T2R9 a potential molecular target in developing targeted therapeutics or imaging agents for PDAC for its low background in other non-diseased regions. Additionally, the 100-1000 times more abundancy of CAFs present in the pancreatic tumor compared to cancer epithelial cells makes them a more tractable and accessible target. To test the targetability, in chapter 4 we developed a T2R9 specific liposome and showed a 1.9-fold increased accumulation in the PDAC admix tumor when compared to non-targeted liposomes. CXCR2 inhibitor delivered by targeted liposome was shown to significantly reduce tumor growth and cancer cell proliferation compared to non-targeted or systematic delivery. Taken together, our in vivo study shows the incorporation of a T2R9 targeting peptide improved pharmacokinetics and pharmacodynamics of drug-loaded nanoparticles in PDAC therapy and suggests T2R9 represents an intriguing molecular target in PDAC. Future studies to unfold the biological functions of T2R9 in PDAC progression may provide further investigation in revealing therapeutic values of T2R9 in pancreatic cancer.

5.3 Future directions

5.3.1 Evaluating other homology clustering algorithms for in vivo NGS-phage display

In chapter 2, we implemented the Hobohm clustering algorithm [8] to select consensus sequences for phage pool isolated from biopanning in the pancreas. However, the in vivo validation of candidate clones showed that Hobohm clustering analysis failed to select CP-specific ligands. This could be the result of highly diverse targets present in the in vivo screens significantly increases the diversity of phage pools and surpasses the sequence alignment capacity of the algorithm to provide a meaningful prediction. To address this limitation, future studies should explore more complex algorithms that able to facilitate multiple protein-protein interactions in large-scale datasets. One example model is Hammock [9], in which progressive clustering was operated parallelly to first identify multiple, small-sized cluster cores from the raw dataset, then followed by iterative procedures to enrich and merge similar clusters. In contrast to top-down methods where a small number of consensus motifs are attempted to fit across all available sequences, the bottom-up hierarchical clustering process is an ideal option for in vivo screens as it weights toward selecting more small-sized clusters (i.e., more diverse targets) but each cluster contains high sequence similarities (i.e., more representative motifs). In addition to sequence similarity, motif clustering based on the peptide's physiochemical properties should also be evaluated. Amino acids with similar physiochemical properties may serve an interchangeable role in target binding. This feature, however, has yet to be captured in any clustering analysis. Future studies to develop an algorithm that links hydrophobicity, charge, or pKa of amino acids to clustering analysis could benefit the discovery of functional motifs.

5.3.2 Completing peptide signature analysis for other pancreas diseases

We have performed 31 NGS-phage display screenings on pancreas-related targets and identified a total of 319 peptides related to normal, inflamed, or malignant pancreas tissues and cell lines (Figure 5.1). Diabetes is another major pancreatic disorder that, while affecting over 460 million people worldwide, still lacks effective biomarker-guided therapy and diagnosis [10]. Future studies should utilize QSAT to profile peptide ligands specific to diabetic cell lines or animal models and complete the full picture of peptide signature for major pancreas diseases.

We have performed a pilot study to screen murine pancreatic α- and β-cells, αTC-6 and NIT, using the conventional clone picking method. In this study, we showed the feasibility of discovering β-cell selective ligands through phage ELISA and identified 8 clones that have 1.5-fold higher binding to NIT over αTC-6 (Figure 5.2). A follow-up study should perform NGS-phage display in those murine cell lines and human β-cells (EndoC-βH1 [11]), and compare the results with the existing database to build a more fulsome characterization of the pancreas disease proteome. Moreover, exploring ligand profiles of β-cells that possess various degrees of insulin-secretory response to glucose would provide valuable insight into delineating essential proteins that regulate glucose-stimulated insulin secretion.

A

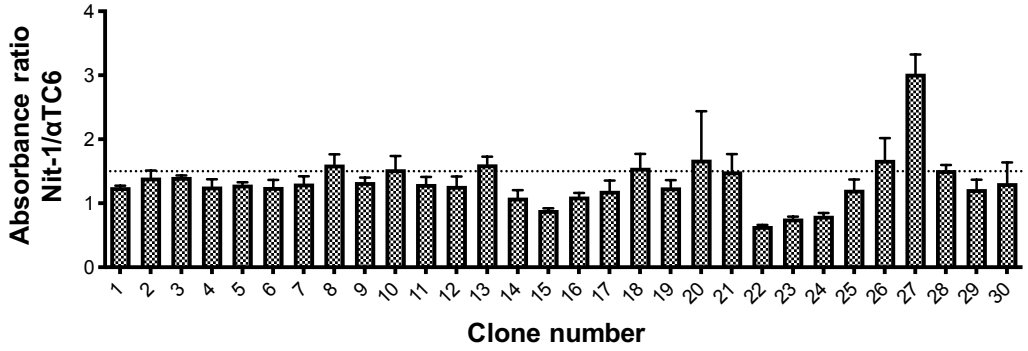

B

Clone #	Peptide sequence
8	AFDWNYR
10	KIPIALS
13	YSIPKSS
18	TMFALPQ
20	TQVTSPD
21	SILPYPY
26	VRPEVML
27	VQTPARM

Figure 5.2 ELISA of candidate clones binding to pancreatic β-cells. (A) 30 phage clones were isolated from the 2nd round of biopanning in Nit-1 while negatively select for αTC-6 cell. Phage binding to each cell line is measured in absorbance. (B) The identity of phage clones that shows Nit-1 selectivity over αTC-6 cells (absorbance ratio > 1.5).

5.3.3 Identifying binding partners of CP-targeting peptides

In chapter 3, we have identified five CP-specific ligands that show cellular selectivity to 3 common cell types and the extracellular matrix of CP. Future studies should use phage display-based functional proteomics and mass spectrometry to identify the binding partners of those ligands [12]. As there are no immortalized cell lines available for CP, target cells used for functional pulldown assay will need to be isolated from the pancreas of the caerulien-induced mice. Primary cell isolation procedures from the pancreas have been developed for PSC [13], macrophage [14], and acinar cells [15]. One challenge that we may encounter is a large number of proteins being captured due to the phage's non-specific binding. This will result in a complex validation process in the subsequence analysis. To address this, incorporating stable isotope labeling by amino acids in cell culture (SILAC) could distinguish pulldown lysates between targeting phage and wildtype phage and allow quantitative comparison on each protein level in mass spectrometry [16, 17]. Identifying the binding partners will enable us to use antibody-staining of panels to determine the location and the number of proteins expressed per target cell and elsewhere. The identified proteins may lead to crucial biological insight into the roles of target cells in CP progression.

5.3.4 Understanding the functional roles of T2R9 in PDAC

In chapter 4, we have shown upregulation of T2R9 in CAFs of PDAC compared to normal human dermal fibroblasts. Extraoral bitter taste receptors have been detected in ovarian cancer, breast cancer, and neuroblastoma, presenting a promising oncological marker. In pancreatic cancer, T2R10 and T2R38 are not only upregulated, they are also involved in regulating chemoresistance and immunosuppression [5, 6, 18]. Thus, it is reasonable to suspect that T2R9 may also serve functional roles in CAF-cancer cells or CAF-immune cells interactions in PDAC. Using our established T2R9 knockdown CAFs, future studies should first evaluate proliferation, migration, and invasion of cancer cells when co-cultured with the wildtype and T2R9 (-) CAF in vitro. The xenograft model of admix tumor composed of iRFP expressed PDAC cells and CAFs with and without T2R9 knockdown would provide insight into whether T2R9 affects tumor growth and metastasis in vivo. Moreover, Dotson et al. found that a T2R9 haplotype is associated with altered

glucose and insulin homeostasis [19]. Whether T2R9 in CAF is also involved in glucose regulation and how T2R9 fits into metabolic reprogramming in pancreatic cancer are both intriguing questions for further investigation to understand the functional roles of T2R9 in PDAC, and potentially lead to new therapeutic strategies.

5.3.5 Evaluating neutropenia and metastasis suppression in targeted CXCR2 treatment

Significant neutropenia has been observed in patients treated with systemic CXCR2 inhibitors [20, 21]. In chapter 4, we have shown CXCR2 inhibitors delivered by targeted liposomes can improve pharmacokinetic and pharmacodynamic in the PDAC mouse model than systemic delivery, but we have yet explored whether targeted delivery could also have a positive effect in reducing neutropenia. To answer this question, the number of neutrophils in plasma needs to be measured throughout the drug treatment course. Our current model is human cell xenograft in the athymic nude mouse, which, however, is immunodeficient for proper neutrophil study. Thus, we sought to identify the mouse homolog of human T2R9 using the protein BLAST tool (NCBI) and found the top two mouse taste receptors, tas2r130 and tas2r105, that share respective 45.02% and 39.94% sequence similarity with T2R9 (Figure 5.3A). Owing to the lack of commercially available murine bitter taste receptor antibodies and recombinant protein, we performed a pilot study to evaluate whether T2R9-targeted liposome still preserve stromal targeting feature in the admix mouse PDAC xenograft (KPC915/NIH3T3) in c57BL/6j mice (Figure 5.3C). Using a cardiomyocyte targeting peptide, I1 [22], to conjugate on liposomes as a non-specific control for PDAC tumor, T2R9-targeted liposomes showed 1.69-fold higher accumulation in tumor region than non-specific nanoparticles at 24 h post-injection (Figure 5.3D-F). These results match with what we observed in human PDAC xenograft, suggesting the T2R9 targeting peptide could still maintain stromal binding despite low sequence similarities shared between human and mouse homologous.

Using the KPC915/NIH3T3 admix model, future studies should determine neutropenia counts in plasma using FACS at various timepoints in immunocompetent mice receiving systemic or targeted CXCR2 treatments. A dose escalation study would be beneficial to determine optimal dosage with minimal toxicity while still maintain antitumoral effects. In addition, CXCR2 inhibition

A

Mus homologous	% a.a. overlap
tas2r130	45.02%
tas2r105	39.94%

B

Liposome	Size (nm) Mean ± SD	Conc. (#/mL)	# peptide per liposome	# DiD per liposome
I1	125.2 ± 38.4	2.82E+13	210.92	3565.98
S3	123.7 ± 52.8	3.21E+13	212.23	3918.88

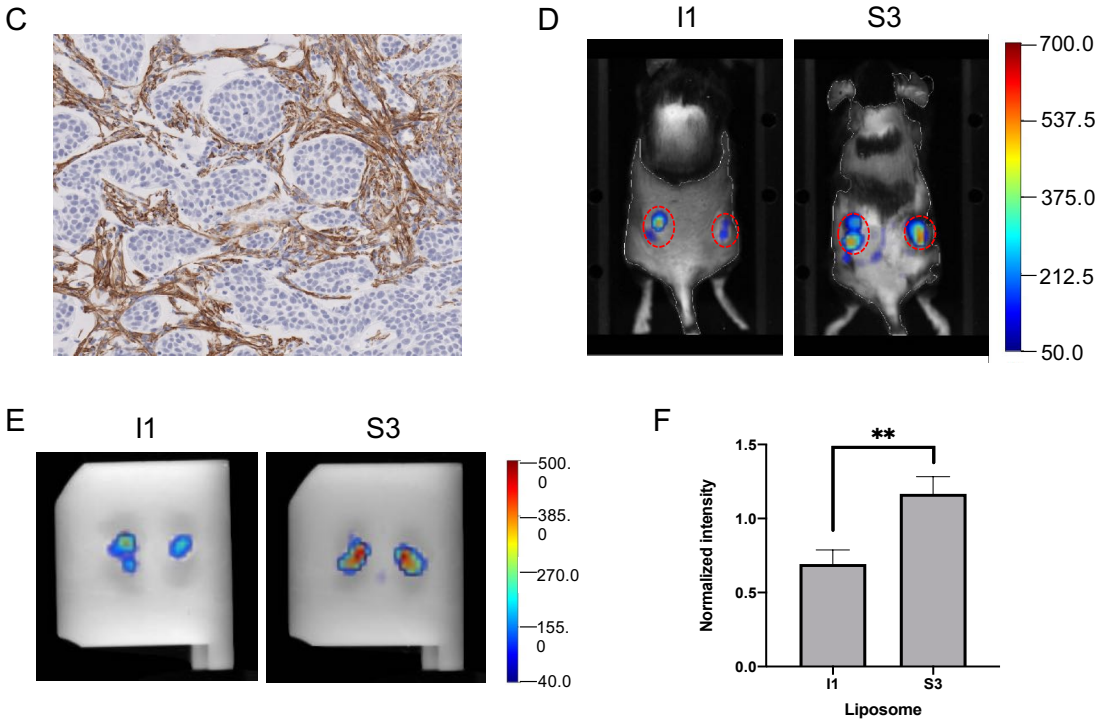

Figure 5.3 T2R9 targeting peptide improves liposome accumulation in the admix KPC915/NIH3T3 tumor model. (A) Comparison of amino acid sequences of human Tas2r9 with its mouse homologous. (B) Characterization of peptide-conjugated liposomes: I1, TALPRLN, a cardiomyocyte-targeting peptide. I1 is used as a negative control for mouse stroma. S3, HTTIPKV. Liposome size, concentration, and # of peptide per liposome is determined by NanoSight. The number of dye (DiD) per liposome is determined by Nanodrop. (C) αSMA immunostaining of admix tumor sections showed αSMA-positive stroma occupied 30.67 ± 7.80% of area at 7 days post KPC915/NIH3T3 inoculation. N = 3 mice, 6 images/tumor. (D) Mice bearing subcutaneous admix KPC915/NIH3T3 tumors (D7 post-inoculation) were injected with I1- and S3-liposomes. Images show FMT in vivo imaging at 24h post-injection. (E) FMT ex vivo imaging of admix tumors at 24h post-injection. (F) Quantification of fluorescent intensity in ex vivo imaging. Statistical signification was measured with a Student's t-test. **$p < 0.01$, N = 6.

has been shown to profoundly suppress PDAC metastases [23]. From the xenograft model, we observed targeted CXCR2 therapy enhanced tumor burden reduction in the primary tumor. Future studies using an orthotopic admix tumor model could allow the evaluation of targeted CXCR2 inhibition in pancreatic cancer metastasis.

5.4 Summary

Computational methods have leveraged NGS-phage display in high-throughput ligand selection for complex biological systems. In this dissertation, we have developed an analytical approach to rapidly identify disease-specific ligands for pancreas disease. In both chronic pancreatitis and pancreatic cancer, our work demonstrated the promise of utilizing disease-specific ligands to develop targeted therapies and to treat diseases and identify novel molecular targets.

5.5 Reference

[1] G. Y. Locker *et al.*, “ASCO 2006 Update of Recommendations for the Use of Tumor Markers in Gastrointestinal Cancer,” *J. Clin. Oncol.*, vol. 24, no. 33, pp. 5313–5327, Nov. 2006, doi: 10.1200/JCO.2006.08.2644.

[2] M. E. Lowe *et al.*, “Precision Medicine in Pancreatic Disease-Knowledge Gaps and Research Opportunities: Summary of a National Institute of Diabetes and Digestive and Kidney Diseases Workshop,” *Pancreas*, vol. 48, no. 10, pp. 1250–1258, Dec. 2019, doi: 10.1097/MPA.0000000000001412.

[3] C. Bornmann *et al.*, “A new liposomal formulation of Gemcitabine is active in an orthotopic mouse model of pancreatic cancer accessible to bioluminescence imaging,” *Cancer Chemother. Pharmacol.*, vol. 61, no. 3, pp. 395–405, Mar. 2008, doi: 10.1007/s00280-007-0482-z.

[4] L. T. Brinton, D. K. Bauknight, S. S. K. Dasa, and K. A. Kelly, “PHASTpep: Analysis Software for Discovery of Cell-Selective Peptides via Phage Display and Next-Generation Sequencing,” *PLOS ONE*, vol. 11, no. 5, p. e0155244, May 2016, doi: 10.1371/journal.pone.0155244.

[5] M. R. Howitt *et al.*, “Tuft cells, taste-chemosensory cells, orchestrate parasite type 2 immunity in the gut,” *Science*, vol. 351, no. 6279, pp. 1329–1333, Mar. 2016, doi: 10.1126/science.aaf1648.

[6] D. A. Deshpande *et al.*, “Bitter taste receptors on airway smooth muscle bronchodilate by localized calcium signaling and reverse obstruction,” *Nat. Med.*, vol. 16, no. 11, Art. no. 11, Nov. 2010, doi: 10.1038/nm.2237.

[7] “TAS2R9 protein expression summary - The Human Protein Atlas.” https://www.proteinatlas.org/ENSG00000121381-TAS2R9 (accessed May 20, 2021).

[8] U. Hobohm, M. Scharf, R. Schneider, and C. Sander, “Selection of representative protein data sets,” *Protein Sci.*, vol. 1, no. 3, pp. 409–417, 1992, doi: https://doi.org/10.1002/pro.5560010313.

[9] A. Krejci, T. R. Hupp, M. Lexa, B. Vojtesek, and P. Muller, “Hammock: a hidden Markov model-based peptide clustering algorithm to identify protein-interaction consensus motifs in large datasets,” *Bioinformatics*, vol. 32, no. 1, pp. 9–16, Jan. 2016, doi: 10.1093/bioinformatics/btv522.

[10] P. Saeedi *et al.*, “Global and regional diabetes prevalence estimates for 2019 and projections for 2030 and 2045: Results from the International Diabetes Federation Diabetes Atlas, 9th edition,” *Diabetes Res. Clin. Pract.*, vol. 157, p. 107843, Nov. 2019, doi: 10.1016/j.diabres.2019.107843.

[11] V. G. Tsonkova *et al.*, “The EndoC-βH1 cell line is a valid model of human beta cells and applicable for screenings to identify novel drug target candidates,” *Mol. Metab.*, vol. 8, pp. 144–157, Feb. 2018, doi: 10.1016/j.molmet.2017.12.007.

[12] F. Reynolds *et al.*, “A Functional Proteomic Method for Biomarker Discovery,” *PLOS ONE*, vol. 6, no. 7, p. e22471, Jul. 2011, doi: 10.1371/journal.pone.0022471.

[13] L. Zhao *et al.*, “Modified methods for isolation of pancreatic stellate cells from human and rodent pancreas,” *J. Biomed. Res.*, vol. 30, no. 6, pp. 510–516, Nov. 2016, doi: 10.7555/JBR.30.20160033.

[14] J. Xue *et al.*, “Alternatively activated macrophages promote pancreatic fibrosis in chronic pancreatitis,” *Nat. Commun.*, vol. 6, p. 7158, May 2015, doi: 10.1038/ncomms8158.

[15] J. Gout *et al.*, “Isolation and Culture of Mouse Primary Pancreatic Acinar Cells,” *J. Vis. Exp. JoVE*, no. 78, Aug. 2013, doi: 10.3791/50514.

[16] S.-E. Ong *et al.*, “Stable Isotope Labeling by Amino Acids in Cell Culture, SILAC, as a Simple and Accurate Approach to Expression Proteomics,” *Mol. Cell. Proteomics MCP*, vol. 1, pp. 376–86, Jun. 2002, doi: 10.1074/mcp.M200025-MCP200.

[17] S. B. Pollock *et al.*, “Highly multiplexed and quantitative cell-surface protein profiling using genetically barcoded antibodies,” *Proc. Natl. Acad. Sci.*, vol. 115, no. 11, pp. 2836–2841, Mar. 2018, doi: 10.1073/pnas.1721899115.

[18] M. M. Gaida *et al.*, “Expression of the bitter receptor T2R38 in pancreatic cancer: localization in lipid droplets and activation by a bacteria-derived quorum-sensing molecule,” *Oncotarget*, vol. 7, no. 11, pp. 12623–12632, Mar. 2016, doi: 10.18632/oncotarget.7206.

[19] C. D. Dotson *et al.*, “Bitter Taste Receptors Influence Glucose Homeostasis,” *PLoS ONE*, vol. 3, no. 12, Dec. 2008, doi: 10.1371/journal.pone.0003974.

[20] L. M. Campbell, P. J. Maxwell, and D. J. J. Waugh, “Rationale and Means to Target Pro-Inflammatory Interleukin-8 (CXCL8) Signaling in Cancer,” *Pharmaceuticals*, vol. 6, no. 8, Art. no. 8, Aug. 2013, doi: 10.3390/ph6080929.

[21] S. I. Rennard *et al.*, “CXCR2 Antagonist MK-7123. A Phase 2 Proof-of-Concept Trial for Chronic Obstructive Pulmonary Disease,” *Am. J. Respir. Crit. Care Med.*, vol. 191, no. 9, pp. 1001–1011, May 2015, doi: 10.1164/rccm.201405-0992OC.

[22] S. S. K. Dasa *et al.*, “Development of target-specific liposomes for delivering small molecule drugs after reperfused myocardial infarction,” *J. Control. Release Off. J. Control. Release Soc.*, vol. 220, no. Pt A, pp. 556–567, Dec. 2015, doi: 10.1016/j.jconrel.2015.06.017.

[23] C. W. Steele *et al.*, “CXCR2 Inhibition Profoundly Suppresses Metastases and Augments Immunotherapy in Pancreatic Ductal Adenocarcinoma,” *Cancer Cell*, vol. 29, no. 6, pp. 832–845, Jun. 2016, doi: 10.1016/j.ccell.2016.04.014.

Appendix. An automated procedure to batch-analyze colocalization in immunofluorescence images

A.1 Abstract

Colocalization analysis of immunofluorescence images has been widely used in biomedical research to study cellular and molecular functions through evaluating spatial proximities of molecules of interest with cellular compartments or molecule complexes. Manders' correlation coefficient describes the spatial overlap between two signals and offers quantitative evaluation on co-occurrence from multi-color fluorescence images. The computational approach to calculate this coefficient is common in various image processing software, including ImageJ. However, all software applications are user dependent and require multi-step image pre-processing making it difficult to transfer seamlessly between different users, therefore reproducibility is difficult. Additionally, methods that allow the application of systematic procedures to the image pool is not an option, resulting in a lack of efficiency and repeatability. Thus, we developed a robust procedure that includes masking and thresholding background subtraction algorithms as built-in functions that manual image pre-processing is not required. We implemented batch-processing features in both ImageJ and R code to allow automatic evaluation throughout image lists, and summarized overall results in a simple table format such that statistical analysis can be easily carried out.

- Automatic and robust approach for fluorescence image processing.
- High-throughput quantitative colocalization analysis to allow batch processing and simply data extraction for statistical purposes.

A.2 Method overview

Colocalization analysis using immunofluorescence is a common laboratory technique to determine the close proximity of two molecules present in cells and tissues. Computational methods that determine Manders' correlation coefficient (MCC) have been developed in imaging processing software to provide quantitative analyses[1,2]. However, reproducibility is hindered by user variability and batch processing remains unavailable, resulting in lack of efficiency and repeatability. Here, we provide an automated procedure to quantitatively determine the degree of colocalization for statistical purposes from immunofluorescence images using confocal microscopy, ImageJ, and R.

A.3 Required equipment and software

- Immunofluorescence-stained cell or tissue sections.
- Confocal microscopy. In this study, all images were taken using ZEISS LSM-880 Confocal Laser Scanning Microscope (Carl Zeiss Meditec, Inc., Jena, Germany) at the Advanced Microscopy Facility at the University of Virginia. Any confocal microscopy will fit in this procedure.
- Image J/FIJI. The Bio-Formats and JACoP plugins will need to be installed.
- RStudio or similar platform for running the R code.

A.4 Procedure

Throughout this procedure, any fluorescently stained tissues can be used but here we used pancreas tissues, which had been intravenously injected via tail vein with cell targeting peptides, as examples to show colocalization analysis of these peptides with activated pancreatic stellate cells (aPSCs). Phage were covalently conjugated to VivoTag 680 XL (Ex/Em 680/700, red channel) and aPSCs were stained with antibody against its cell marker, αSMA conjugated to FITC (Ex/Em 490/525, green channel). Nucleus stained with DAPI (Ex/Em 358/461, blue channel) is a standard procedure in immunofluorescence staining, which we also included in this procedure to show how to exclude an unneeded signal during image processing.

A.4.1 Image acquisition

1. Immunofluorescence images should be collected using a confocal microscopy to ensure fluorescent signals obtained from all channels are in the same z-section. Carefully choose several fields of view that represent the staining of the entire cell populations or tissues. Avoid area with artifacts due to tissue folding or incorrect staining.
2. Select optimal laser intensity for each channel. Do not over-saturate the pixels.
3. Acquire z-stack images and export as proprietary Ziess *.czi files. Image resolution is recommended to reach a minimum of 1024x1024 to ensure good results. As MCC determines the fractional percentage of pixels overlapping between two channels, poor resolution may lead to miscounts and false results.
4. Proceed to another field of view using the same procedure to acquire enough representative images that covers most of tissue sections.

5. Name the file. Image filename will be inherited in following steps in both ImageJ and R. It is critical to avoid spaces in naming the files as the ImageJ macro code cannot process the image with space in the filename. The recommended format for the filename is “stain1_stain2_magnification.czi”, which will allow R to easily extract the correct information about the image.

A.4.2 Image pre-processing

1. Import *.czi files to ImageJ. Make sure Bio-Formats plugin is installed in ImageJ. Bio-format plugin[3] can be downloaded at https://www.openmicroscopy.org/bio-formats/.
2. In the Bio-Formats Import Options, choose the following settings and click “OK” to import (Figure A.1A).
3. View stack with: “Hyperstack”.
4. Dataset organization: check “Open files individually” and “Open all series”
5. Color mode: “Colorized”
6. Metadata viewing: “Display metadata”
7. Memory management: “Use virtual stack”
8. The imported Zeiss file is composed of z-stack images with signals from 3 channels in parallel images. To merge 3 channels, first split channels at “Image” > “Color” > “Split channel”, then assign proper color for each channel at “Image” > “Color” > “Merge channels”. Make sure the color matches with the image: C1 = red. C2 = green, C3 = blue. Check “Create composite”, then “OK”.
9. On the merged image, scroll the Z-bar at the bottom to choose the best representative image. Adjust brightness and contrast if needed (Figure A.1B).
10. Save the best representative merged image as *.jpg file. Keep all *.jpg files from the same experiment in the same folder for batch processing in colocalization analysis (Figure A.1C).

A.4.3 Background subtraction and batch colocalization analysis in ImageJ

The main colocalization analysis will be performed using the JACoP plugin in ImageJ. To account for background signals, we added a background subtraction step before feeding the images to JACoP. A complex masking method was used on an individual channel to remove background noise that resulted from each stain. Using an aPSC-targeting phage as an example, we showed that including a mask subtraction algorithm could reduce background by 50% (Figure

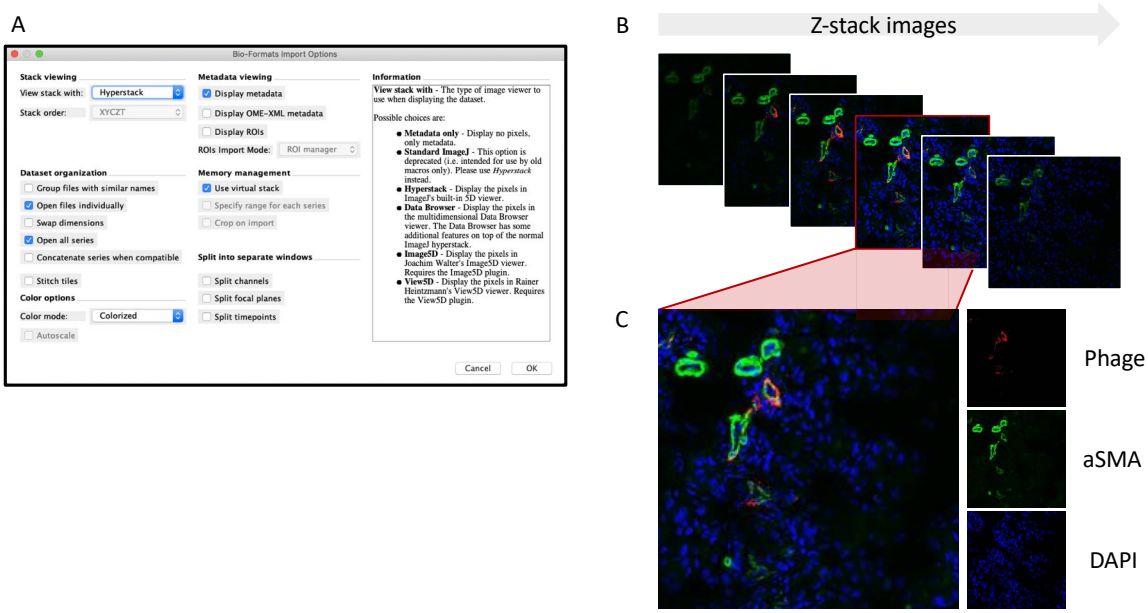

Figure A.1. Image pre-processing procedures. (A) *.czi files were imported to Image J using Bio-Format plugin. (B) The optimal image from the z-stacks were selected and saved as *.jpg as the input file for the colocalization analysis. (C) A multi-channel image can be analyzed in this approach.

A.2A). This is significant as background noise can account for false-positive colocalization between 2 channels (Figure A.2B). Applying background removal to various phage systems, we demonstrated a reduction of 48.17% and 45.24% in MCC of two non-aPSC-targeting phage, respectively. In comparison, only a 17.72% reduction occurred in MCC of the aPSC-targeting phage (Figure A.2C). This suggested that the inclusion of the mask subtraction method amplified the differentiation between true colocalization from non-specific signals.

The background subtraction function is a feature of our batch processing macro code so that users do not need to perform manual background subtraction. JACoP also includes a thresholding background removal function in the colocalization analysis. We used Ostu's thresholding option in this procedure to ensure reproducibility. Threshold values of each channel are reported on the final output file for users' reference. Procedures to initiate the code are as follows.

ImageJ macro code: *"IF colocalization analysis.ijm".*

1. In Image J, make sure JACoP plugin is installed. The JACoP[1] plugin can be downloaded at https://imagejdocu.tudor.lu/doku.php?id=plugin:analysis:jacop_2.0:just_another_colocalization_plugin:start.
2. Drag "IF colocalization analysis.ijm" file to ImageJ to open the macro code. And click "Run" to initiate the code.
3. Choose the folder containing *.jpg files of the best representative merged images from image pre-processing as input files.
4. Three output folders will be generated under the input folder, including:
5. Channel_splitted_images: *.jpg files of each channel, both raw and background subtracted.
6. JACoP: final red and green channel images that feed into JACoP for colocalization analysis.
7. JACoP log files: the output text files (*.txt) containing the colocalization results generated from JACoP. This folder will be used as an input folder in the R code for data extraction.

A.4.4 Colocalization parameters extraction in R

The colocalization parameters generated from ImageJ are saved as a text file for each image, which is rather difficult for users to quickly extract needed values for statistical analysis when a great number of images are analyzed. Thus, we developed an R code to rapidly extract relevant parameters into a summary table. Parameters regarding image information, threshold values, and colocalization coefficients, including Pearson coefficient, Manders' overlap coefficient, and Manders' correlation coefficients will be generated (Figure A.3). Procedures to process the code are as follows.

R code: *"Log_batch_processing.R".*

1. Open "Log_batch_processing.R" in RStudio.
2. Run the R code. Choose the folder containing *.txt files generated from ImageJ. R will generate a "Colocalization_Analysis_Output.csv" file summarizing all parameters from every log file in the folder.

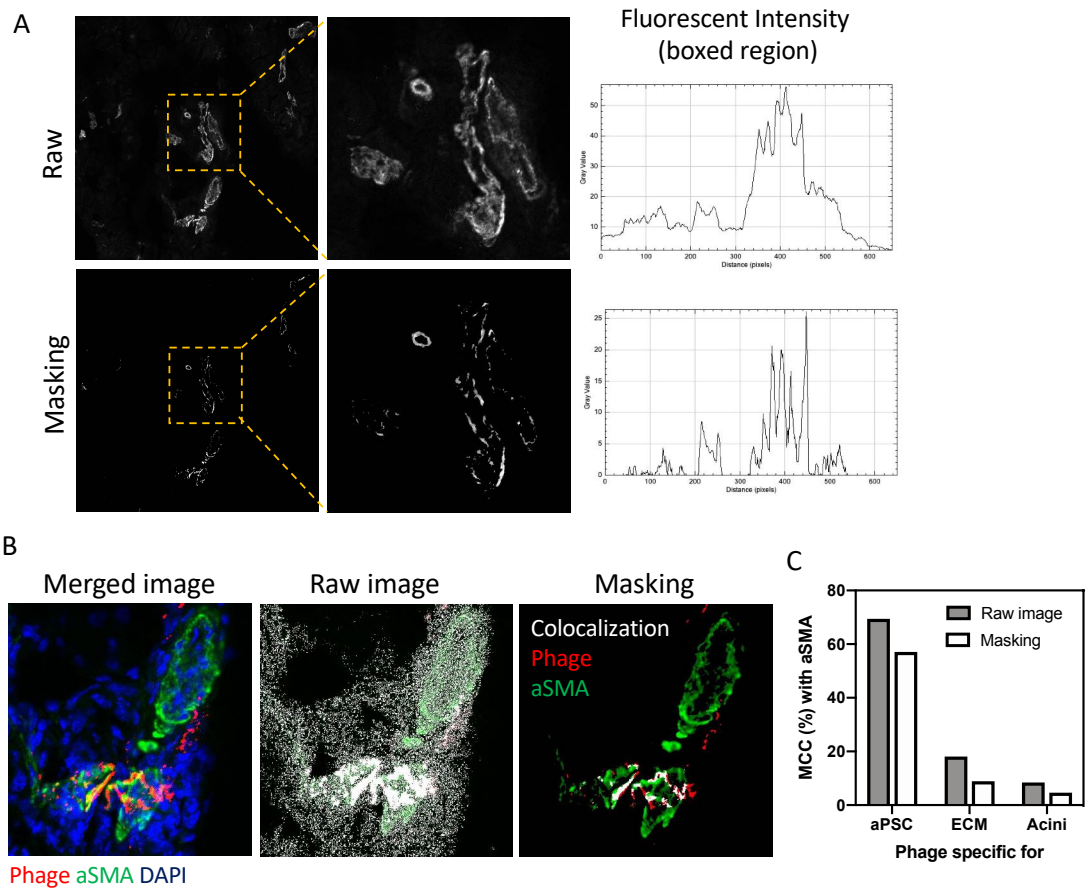

Figure A.2. Background subtraction through masking algorithm. (A) Overall fluorescent signal reduced after application of masking on the aPSC-targeting phage image. (B) Masking contributed to clearer signals of multi-channel images and removed false colocalization resulted from background noise. (C) MCC analysis before and after background subtraction to remove non-specific signal. Extent of colocalization was relatively unchanged for the targeted agent in contrast to non-targeted agents whose signals are mainly non-specific.

A.5 Additional information

The effectiveness of the proposed procedure has been compared with the standard procedure of colocalization analysis performed manually on the JACoP plugin in ImageJ[1]. In the standard procedure, the optimal multi-color images chosen from confocal z-stacks are first split into single-channel images before importing to JACoP. Costes' automatic thresholding is built into JACoP and offers background correction of the input images. However, if a different thresholding algorithm is needed to provide better noise removal, users would have to pre-process the images before the colocalization analysis. The results generated from JACoP are then recorded, and a

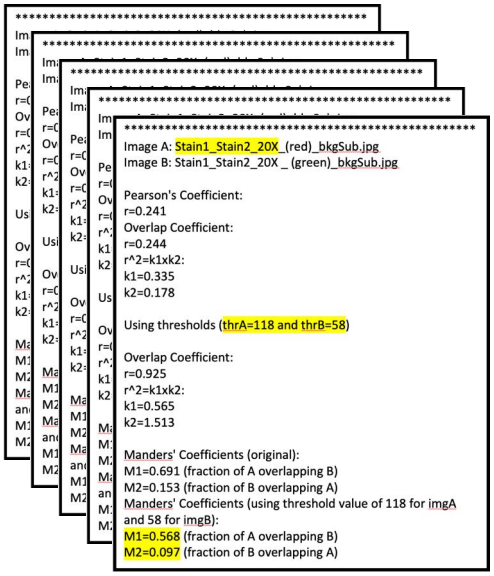

Image info | JACoP Threshold values | Raw values | Threshold applied

Filename	Stain 1	Stain 2	Mag.	Threshold value of		Pearson Coeff.	Overlap Coeff.	Manders' Correlation Coeff.			
				Stain 1	Stain 2			M1	M2	tM1	tM2
Image 1	Phage 1	αSMA	20	118	58	0.241	0.925	0.691	0.153	0.568	0.097
Image 2	Phage 2	αSMA	20	102	102	0.044	0.965	0.178	0.089	0.086	0.021
⋮	⋮	⋮	⋮	⋮	⋮	⋮	⋮	⋮	⋮	⋮	⋮
Image X	Phage X	αSMA	20	91	104	0.031	0.951	0.086	0.081	0.044	0.025

Figure A.3. Example output from the R code. Colocalization analysis in Image J generates results as *.txt files for each image. Highlighted rows are the only needed information from the text file for MCC analysis. In our R code, we extracted relevant parameters from text format to excel table for the ease of statistical analysis.

new analysis applied to a new set of images until all images have been processed. With the standard procedure using built-in Costes' thresholding method, an average of 30 seconds is required to complete the analysis of one image. The process may take beyond several minutes to complete for each image if a multi-step pre-processing is required, which is common in fluorescent image analysis. Our automated process incorporated a background subtraction algorithm prior to JACoP and offered a significantly reduced execution time demonstrated by batch processing of 100 images in less than 10 minutes (Figure A.4A). In addition, data extraction on R can be completed within a second, significantly reducing the amount of working time and potential errors caused by data retrieval or typos. In comparison with the standard procedure, the proposed method generated identical colocalization parameters using the same set of input images and settings but completed the process within a noticeably shorter amount of time (Figure A.4B). All images generated throughout the procedure were automatically saved to allow users to revisit if needed. With the output colocalization parameters along with the image information summarized in a single *.csv file, users can directly import the results to Excel or similar platforms to perform downstream data analysis.

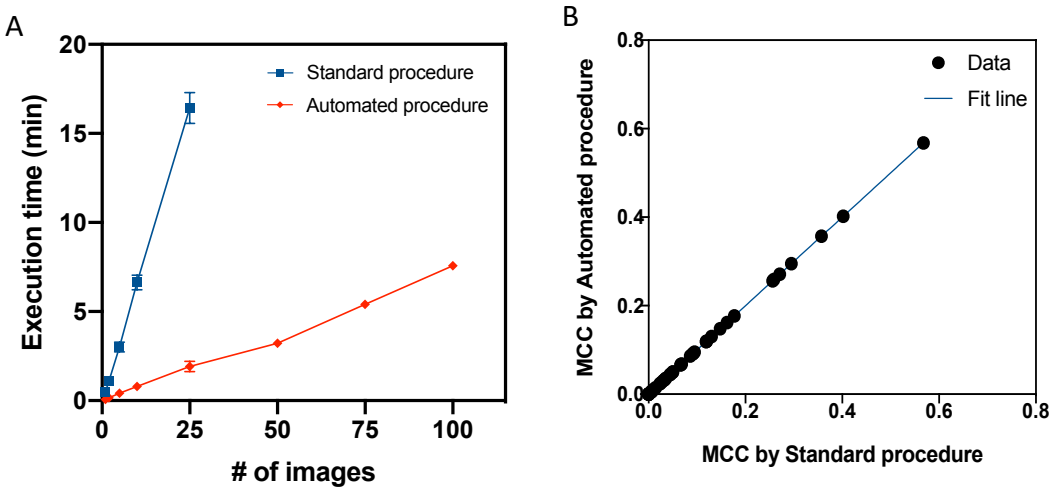

Figure A.4. Procedure execution time. (A) The execution time required to perform JACoP colocalization analysis using standard procedure and the proposed automated procedure. The measured time did not include image pre-processing from z-stacks. Mean ± SD, n = 5 for standard procedure, n =10 for proposed procedure. (B) The correlation curve of MCC generated by the standard and proposed procedure. A perfect fit was observed in 50 images analyzed with both methods using the same JACoP settings. $R^2 = 1$.

A.6 Reference

1. Bolte, S. & Cordelières, F. P. A guided tour into subcellular colocalization analysis in light microscopy. *J. Microsc.* **224**, 213–232 (2006).

2. Dunn, K. W., Kamocka, M. M. & McDonald, J. H. A practical guide to evaluating colocalization in biological microscopy. *Am. J. Physiol. - Cell Physiol.* **300**, C723–C742 (2011).

3. The Open Microscopy Environment. https://www.openmicroscopy.org/bio-formats/.

A.7 Code

A.7.1. ImageJ macro code: IF colocalization analysis.ijm

```
// This code takes in 3-channel (RGB) .jpg images and generates Mander's correlation
// coefficients (MCC) for markers in the red and green channel. The output folders include:
//   1. Channel_splitted_images: .jpg for each color, raw and background subtracted.
//   2. JACoP: final red and green images used in JACoP analysis.
//   3. JACoP Log files: .txt files containing MCC from JACoP.
//      *** THIS IS THE FOLDER THAT WILL BE USED IN "Log_processing_batch.R" ***

// ps: 1. ImageJ macro can't handle file names with space. Avoid spaces when naming the input images.
//     2. Depending on RAM of the computer, this code may not run >50 input images at once.
//     3. code may need to be changed if the input images contain channels other than 3.


// ask user to select a folder for analysis
MainDir = getDirectory("Select A folder");
MainFileList = getFileList(MainDir);

// Split channels
splitted_dir = MainDir + File.separator + "Channel_splitted_images" + File.separator ;
File.makeDirectory(splitted_dir);

setBatchMode(true); //activate batch mode
for (i = 0; i < lengthOf(MainFileList); i++) {
    // define path
    current_imagePath = MainDir+MainFileList[i];

    // check that the currentFile is not a directory
    if (!File.isDirectory(current_imagePath)){
        open(current_imagePath);
        getDimensions(width, height, channels, slices, frames);
        run("Split Channels"); // split channels

        // Save the generated images as jpeg in the "Channel_splitted_images" folder
        ch_nbr = nImages ;
        for ( c = 1 ; c <= ch_nbr ; c++){
            selectImage(c);
            currentImage_name = replace(toUpperCase(getTitle()), ".JPG ","_");
            saveAs("jpg", splitted_dir + currentImage_name);
        }
        run("Close All"); // Clear opened images
    }
}
setBatchMode(false);

//// Masking///
// background mask generation
dir2 = splitted_dir;
fileList2 = getFileList(dir2);
Mask_dir = dir2 + File.separator + "Mask" + File.separator ;
File.makeDirectory(Mask_dir);

setBatchMode(true);
for (i = 0; i < lengthOf(fileList2); i++) {
    current_imagePath2 = dir2+fileList2[i];
    if (!File.isDirectory(current_imagePath2)){
        open(current_imagePath2);
        getDimensions(width, height, channels, slices, frames);

        // Use default threshold as background mask
        setAutoThreshold("Default");
        call("ij.plugin.frame.ThresholdAdjuster.setMode", "B&W");
        setOption("BlackBackground", true);
        run("Convert to Mask");
        run("Dilate");

        // Save the generated images as jpeg in the "Mask" folder
        ch_nbr = nImages ;
        for ( c = 1 ; c <= ch_nbr ; c++){
            selectImage(c);
            currentImage_name2 = getTitle() + "_mask";
            currentImage_name2 = replace(currentImage_name2, ".jpg","");
            saveAs("jpg", Mask_dir+currentImage_name2);
        }
        run("Close All");
    }
}
setBatchMode(false);

```

```
// Apply mask subtraction
dir3 = Mask_dir;
fileList3 = getFileList(dir3);
BkgSubB_dir = dir3 + File.separator + "bkg_subtracted_Blue" + File.separator ;
BkgSubR_dir = dir3 + File.separator + "bkg_subtracted_Red" + File.separator ;
BkgSubG_dir = dir3 + File.separator + "bkg_subtracted_Green" + File.separator ;

setBatchMode(true);
for (i = 0; i < lengthOf(fileList2); i++) {
    current_imagePath2 = dir2+fileList2[i];
    current_imagePath3 = dir3+fileList3[i];
    open(current_imagePath2);
    img = getTitle();
    open(current_imagePath3);
    mask = getTitle();
    imageCalculator("Subtract create", img, mask);

    // Save background subtracted images as jpeg in the bkg_subtracted_Blue/Red/Green folder
    currentImage_name3 = getTitle() + "_bkgSub";
    currentImage_name3 = replace(currentImage_name3, "Result of ","");
    currentImage_name3 = replace(currentImage_name3, ".jpg","");
    // Assign RGB images in 3 folders, respectively
        if(indexOf(currentImage_name3,"BLUE") >= 0) {
        File.makeDirectory(BkgSubB_dir);
        saveAs("jpg", BkgSubB_dir+currentImage_name3);
    }
        if(indexOf(currentImage_name3,"RED") >= 0) {
        File.makeDirectory(BkgSubR_dir);
        saveAs("jpg", BkgSubR_dir+currentImage_name3);
    }
        if(indexOf(currentImage_name3,"GREEN") >= 0) {
        File.makeDirectory(BkgSubG_dir);
        saveAs("jpg", BkgSubG_dir+currentImage_name3);
    }

    run("Close All");
}
setBatchMode(false);

// JACOP
dir4 = BkgSubR_dir; //Red
fileList4 = getFileList(dir4);
dir5 = BkgSubG_dir; //Green
fileList5 = getFileList(dir5);
JACoP_dir = MainDir + File.separator + "JACoP" + File.separator;
dir6 = JACoP_dir;
JACoP_log = MainDir + File.separator + "JACoP Log files" + File.separator;
//#define LOWERTOUPPER(x) ((x - 'a') + 'A')

setBatchMode(true);
for (i = 0; i < lengthOf(fileList4); i++) {
    // Save red & green images into a joint "JACoP" folder
    // Red image
    File.makeDirectory(BkgSubR_dir);
    current_imagePath4 = dir4+fileList4[i];
    open(current_imagePath4);
    Image_red = getTitle();
    //Image_red = toUpperCase(getTitle());
    File.makeDirectory(JACoP_dir);
    saveAs("jpg", JACoP_dir+Image_red);
    close(Image_red);

    // Green image
    File.makeDirectory(BkgSubG_dir);
    current_imagePath5 = dir5+fileList5[i];
    open(current_imagePath5);
    Image_green = getTitle();
    //Image_green = toUpperCase(getTitle());
    File.makeDirectory(JACoP_dir);
    saveAs("jpg", JACoP_dir+Image_green);
    close(Image_red);

```

```
    // Mander's coefficient analysis
    File.makeDirectory(JACoP_dir);
    fileList6 = getFileList(dir6);
    Array.sort(fileList6);

    // Obtain thresholds on green images
    current_imagePath6 = dir6+fileList6[2*i];
    open(current_imagePath6);
    img_Gn = getTitle(); // Green
    setAutoThreshold("Otsu dark");
    getThreshold(lower_gn, upper_gn);
    thr_gn = (lower_gn);

    // Obtain thresholds on red images
    current_imagePath7 = dir6+fileList6[2*i+1];
    open(current_imagePath7);
    img_Rd = getTitle();
    setAutoThreshold("Otsu dark");
    getThreshold(lower_rd, upper_rd);
    thr_rd = (lower_rd);

    // Initiate JACoP Plugin
    run("JACoP ", "imga="+img_Rd+" imgb="+img_Gn+" thra="+d2s(thr_rd,0)+" thrb="+d2s(thr_gn,0)+" pearson overlap mm");

    // Save Mander's coefficients as a text file in the "JACoP Log files" folder
    selectWindow("Log");
    result = replace(img_Rd, "\\_\\(RED\\)\\_bkgSub","");
    File.makeDirectory(JACoP_log);
    saveAs("Text", JACoP_log+result);

    // Clear logs and all images
    print("\\Clear");
    run("Close All");
}
setBatchMode(false);
```

A.7.2. R code: Log_batch_processing.R

```
###### This code batch processes and extracts colocaliztion coefficients from log files generated from JACoP, ImageJ. ######
###### All coefficients in the log files from the same input folder will be compiled into a single .csv file.          ######
###### Package "svDialogs" will need to be installed before running this code.                                         ######

# install.packages('svDialogs')
library("svDialogs")

# Function that extracts colocalization coefficients from log files (.txt) generated from JACoP, ImageJ
summarize_data <- function(data){
 # Read files
 dat <- read.table(data, header = FALSE, sep = "", fill = TRUE, stringsAsFactors = FALSE)
 v1 <- dat[ ,1]
 v2 <- dat[ ,2]
 v3 <- dat[ ,3]

 # Images info
 Img_ID <- v3[2]
 ind_red <- as.numeric(gregexpr('RED',Img_ID[1])) -3 # Index of "red"
 Img_ID <- substr(Img_ID, 1, ind_red)
 Stain1 <- substr(Img_ID, 1, 7)
 ind__ <- unlist(gregexpr('_',Img_ID)) # Index of "_"
 Stain2 <- substr(Img_ID, ind__[1]+1, ind__[2]-1)
 Mag <- as.numeric(substr(Img_ID, ind__[2]+1, ind__[3]-2))

 # Ostu threshold
 ThrA <- v3[11]
 ThrA <- as.numeric(substr(ThrA, unlist(gregexpr('=',ThrA))+1, nchar(ThrA)))
 ThrB <- v2[12]
 ThrB <- as.numeric(substr(ThrB, unlist(gregexpr('=',ThrB))+1, nchar(ThrB)-1))

 # Mander's coefficients
 Pearson_r <- v1[5]
 Pearson_r <- as.numeric(substr(Pearson_r, unlist(gregexpr('=',Pearson_r))+1, nchar(Pearson_r)))
 Overlap_r <- v1[14]
 Overlap_r <- as.numeric(substr(Overlap_r, unlist(gregexpr('=',Overlap_r))+1, nchar(Overlap_r)))
 M1 <- v1[19]
 M1 <- as.numeric(substr(M1, unlist(gregexpr('=',M1))+1, nchar(M1)))
 M2 <- v1[21]
 M2 <- as.numeric(substr(M2, unlist(gregexpr('=',M2))+1, nchar(M2)))
 tM1 <- v1[28]
 tM1 <- as.numeric(substr(tM1, unlist(gregexpr('=',tM1))+1, nchar(tM1)))
 tM2 <- v1[30]
 tM2 <- as.numeric(substr(tM2, unlist(gregexpr('=',tM2))+1, nchar(tM2)))

 # Generate table
 JACoP <- as.data.frame(rbind(Value = c(Img_ID, Stain1, Stain2, Mag, ThrA, ThrB, Pearson_r, Overlap_r, M1, M2,
tM1, tM2)))
 names(JACoP) <- c("ImageID", "Stain1", "Stain2", "Magnification", "Threshold_A", "Threshold_B",
                   "PearsonCoeff.", "MandersOverlapCoeff.", "M1", "M2", "tM1", "tM2")
 return(JACoP)
}
```

```
# Choose directory for folder of ImageJ output log files
myDir <- setwd(dlg_dir(default = getwd())$res)
files <- list.files(path=myDir, pattern="*.txt", full.names=TRUE, recursive=FALSE)

# Apply functions
coeff <- lapply(files, FUN = summarize_data)
coeff_sorted <- data.frame(Reduce(rbind, coeff))

# Save Output as a .csv file
outputfile <- paste(myDir,"/Colocalization_Analysis_Output.csv", sep = "")
write.csv(coeff_sorted, outputfile, row.names = FALSE)
```